DISS. ETH NO. 28307

The role of ammonia and nitric acid on new particle formation and growth in urban environments

A thesis submitted to attain the degree of

DOCTOR OF SCIENCES of ETH ZURICH

(Dr. sc. ETH Zurich)

presented by

Ruby Marten

Master in Science in Chemistry with Industrial Experience with First Class Honours
University of Bristol, UK

born on 25.04.1993

Citizen of the United Kingdom and Canada

accepted on the recommendation of

Prof. Dr. Urs Baltensperger (examiner)
Dr. Imad El Haddad (co-examiner)
Prof. Dr. Ruth Signorell (co-examiner)
Prof. Dr. Gordon McFiggans (co-examiner)

2022

Contents

Summary

Aerosols are an important part of the atmosphere, they are defined as liquid or solid particles suspended in air, ranging from one nanometer to tens of micrometers in diameter. Aerosols affect the climate directly, via aerosol-radiation interactions, and indirectly, via aerosol-cloud interactions. While pollution in cities does not have the largest impact on global climate, it does affect local climate and weather. Aerosols can also be deadly; in 2019 lower respiratory infections were reported as the third leading cause of death globally, which are largely caused by aerosols. Since around 55% of the world's population live in cities, it is important to understand the key drivers of urban aerosol formation and growth. Ammonium nitrate is an important component of aerosols, but not much is known about its contribution to aerosol formation and early growth. In this thesis, we aim to understand how nitric acid (HNO_3) and ammonia (NH_3) can impact aerosol formation in urban environments.

Previous understanding of urban air conditions led to a puzzle of competing growth rates and loss rates, where it appeared that measured growth rates in cities were not high enough to explain the persistence of particle number concentrations in the face of high loss rates from coagulation with pre-existing large particles. Results from the CLOUD chamber at CERN presented in this thesis show a newly discovered mechanism of rapid growth by formation of ammonium nitrate onto pre-existing particles. We find that in situations of excess NH_3 and HNO_3, with respect to ammonium nitrate saturation ratios, particles can grow orders of magnitude faster than previously measured in ambient environments. Since this mechanism is consistent with the nano-Köhler theory, there is an activation diameter above which ammonium nitrate can form on the particles, and particles as small as a few nanometers can be affected. Furthermore, this mechanism was found to have a strong temperature dependence where at lower temperatures the same gas phase concentrations result in higher growth rates. At temperatures as low as −25°C, ammonia and nitric acid were found to be able to nucleate even in the absence of sulfuric acid or other known nucleating species.

In order to determine whether these rapid growth rates are in fact high enough to overcome high coagulation loss rates, further experiments were undertaken at the CLOUD chamber at

CERN at 5°C in the presence of a high condensation sink, analogous to haze. Experimental results showed that in experiments with higher NH_3 and HNO_3 concentrations, particle number concentrations were sustained with a steady formation of 2.5 nm particles. Newly formed particles are found to be effectively lost to the condensation sink, thus confirming that loss rates have not been over-estimated, and high growth rates are more likely to be the explanation for particle survival in haze conditions. Alongside experimental results, a kinetic model was developed which is capable of quantitatively reproducing growth from ammonium nitrate formation. We used this model to predict particle survival over a wide range of NH_3 and HNO_3 concentrations and condensation sinks. Results showed that survival of newly formed particles was drastically increased in the presence of supersaturated conditions of NH_3 and HNO_3.

Since supersaturation of NH_3 and HNO_3 is needed in order to achieve these high growth rates, and since ambient environments typically tend towards equilibrium, the third and final chapter of this thesis investigates whether expected inhomogeneities in concentrations and temperatures in a city are sufficient to cause substantial changes in the particle size distribution. The kinetic model was adapted to be able to quantitatively reproduce experiments at −10°C as well as 5°C. Using the model, a simulation was performed of an air parcel moving up in altitude, and thus down in temperature. Results show that the resulting perturbation from equilibrium is sufficient to grow small particles through the most vulnerable size range. Even after returning to equilibrium conditions at the surface, the newly grown particles continue to survive and grow via condensation of other gases. The effect was even more considerable when multiple temperature changes were simulated, as an air parcel rises and falls. Testing inhomogeneities in the gas phase NH_3 concentration, e.g. from car emissions, yielded similar results where small particles grew rapidly during the short bursts of supersaturation. In conclusion, short and rapid changes in temperature and gas-phase concentrations are sufficient to cause drastic changes in the particle size distribution, and can lead to an increase in CCN, thus sustaining haze and pollution. Since the inhomogeneities used in the model were based on ambient measurements, it is plausible that ammonium nitrate formation has an important impact on aerosol number and size distribution in polluted environments.

Zusammenfassung

Aerosole sind ein wichtiger Bestandteil der Atmosphäre. Dabei handelt es sich um flüssige oder feste Partikel in der Luft. Der Durchmesser von Aerosolpartikeln liegt zwischen 1 nm bis zu knapp 100 µm. Aerosole beeinflussen das Klima direkt über Aerosol-Strahlung-Wechselwirkungen und indirekt über Aerosol-Wolken-Wechselwirkungen. Die Luftverschmutzung in Städten hat nicht den grössten Einfluss auf das globale Klima, jedoch beeinflusst sie das lokale Klima und das Wetter. Aerosole können auch tödlich sein; 2019 wurden Infektionen der unteren Atemwege weltweit als dritthäufigste Todesursache gemeldet, diese wurden grösstenteils durch Aerosole verursacht. Da rund 55 % der Weltbevölkerung in Städten leben, ist es wichtig, die Quellen der städtischen Aerosolbildung und des Wachstums zu verstehen. Ammoniumnitrat ist ein wichtiger Bestandteil von Aerosolen, aber über seinen Beitrag zur Aerosolbildung und zum frühen Wachstum ist nicht viel bekannt. In dieser Arbeit wollen wir verstehen, wie Salpetersäure (HNO_3) und Ammoniak (NH_3) die Aerosolbildung in städtischen Umgebungen beeinflussen können.

Vorherige Studien der städtischen Luftbedingungen führten zu einem Rätsel konkurrierender Wachstumsraten und Verlustraten, bei denen es den Anschein hatte, dass die gemessenen Wachstumsraten in Städten nicht hoch genug waren, um die anhaltende Partikelanzahlkonzentrationen angesichts der hohen Verlustraten durch Koagulation mit bereits existierenden grossen Partikeln zu erklären. Ergebnisse aus der CLOUD-Kammer am CERN, die in dieser Dissertation vorgestellt werden, zeigen einen neu entdeckten Mechanismus des schnellen Wachstums durch Bildung von Ammoniumnitrat auf bereits existierenden Partikeln. Wir stellen fest, dass in Situationen mit überschüssigem NH_3 und HNO_3 in Bezug auf die Ammoniumnitrat-Sättigungsverhältnisse Partikel erheblich schneller wachsen können als zuvor in Feldstudien gemessen wurde. Da dieser Mechanismus mit der Nano-Köhler-Theorie übereinstimmt, gibt es einen Aktivierungsdurchmesser, oberhalb dessen sich Ammoniumnitrat auf den Partikeln bilden kann, wobei Partikel, die nur wenige Nanometer gross sind, betroffen sein können. Darüber hinaus wurde festgestellt, dass dieser Mechanismus eine starke Temperaturabhängigkeit aufweist, indem bei niedrigeren Temperaturen die gleichen Gasphasenkonzentrationen zu höheren Wachstumsraten führen. Es wurde festgestellt, dass

Ammoniak und Salpetersäure bei so niedrigen Temperaturen wie −25 °C selbst in Abwesenheit von Schwefelsäure, oder anderen bekannten nukleierenden Spezies, Keime bilden können.

Um festzustellen, ob diese schnellen Wachstumsraten tatsächlich hoch genug sind, um hohe Koagulationsverlustraten zu überwinden, wurden weitere Experimente an der CLOUD-Kammer am CERN bei 5 °C in Gegenwart einer hohen Kondensationssenke, analog zu einer Smog-Situation, durchgeführt. Die Ergebnisse zeigten, dass in Experimenten mit höheren NH_3 und HNO_3 Konzentrationen Partikelanzahlkonzentrationen mit einer stetigen Bildung von 2.5 nm Partikeln aufrechterhalten wurden. Es wurde festgestellt, dass neu gebildete Partikel effektiv an die Kondensationssenke verloren gehen, was bestätigt, dass die Verlustraten nicht überschätzt wurden und dass hohe Wachstumsraten eher die Erklärung für das Überleben der Partikel auch in Smog-Situationen sind. Neben experimentellen Ergebnissen wurde ein kinetisches Modell entwickelt, das in der Lage ist, das Wachstum aus der Ammoniumnitratbildung quantitativ abzubilden. Wir haben dieses Modell verwendet, um das Überleben von Partikeln über einen breiten Bereich von NH_3 und HNO_3 Konzentrationen und Kondensationssenken vorherzusagen. Die Ergebnisse zeigten, dass das Überleben neu gebildeter Partikel in Gegenwart von übersättigten Bedingungen von NH_3 und HNO_3 drastisch erhöht wurde.

Da eine Übersättigung von NH_3 und HNO_3 erforderlich ist, um diese hohen Wachstumsraten zu erreichen, und da atmosphärische Bedingungen typischerweise zum Gleichgewicht tendieren, untersucht das dritte und letzte Kapitel dieser Arbeit, ob erwartete Inhomogenitäten in Konzentrationen und Temperaturen in einer Stadt ausreichen, um erhebliche Veränderungen in der Partikelgrössenverteilung zu verursachen. Das kinetische Modell wurde angepasst, um Experimente sowohl bei −10 °C als auch bei 5 °C quantitativ reproduzieren zu können. Unter Verwendung des Modells wurde eine Simulation eines Luftpakets durchgeführt, das sich in der Höhe und damit in der Temperatur nach oben bewegt. Die Ergebnisse zeigen, dass die resultierende Störung des Gleichgewichts ausreicht, um kleine Partikel durch den anfälligsten Grössenbereich wachsen zu lassen. Selbst nach der Rückkehr zu Gleichgewichtsbedingungen an der Oberfläche überleben die neu gewachsenen Partikel weiter und wachsen durch Kondensation anderer Gase. Noch deutlicher war der Effekt, wenn mehrere Temperaturwechsel

simuliert wurden, also ein Luftpaket auf- und absteigt. Prüfung von Inhomogenitäten in der NH_3 Konzentration in der Gasphase, z.B. aus Autoabgasen, ergaben ähnliche Ergebnisse, bei denen kleine Partikel während der kurzen Übersättigungsschübe schnell wuchsen. Zusammenfassend lässt sich sagen, dass kurze und schnelle Änderungen der Temperatur und der Gasphasenkonzentrationen ausreichen, um drastische Änderungen der Partikelgrössenverteilung zu verursachen, und zu einer Erhöhung des CCN führen können, wodurch Dunst und Verschmutzung aufrechterhalten werden. Da die im Modell verwendeten Inhomogenitäten auf Umgebungsmessungen basierten, ist es plausibel, dass die Bildung von Ammoniumnitrat einen wichtigen Einfluss auf die Aerosolanzahl und -grössenverteilung in verschmutzten Umgebungen hat.

Acknowledgements

My first thanks go to my incredible supervisors whom I have had the pleasure of working with for over four years. Thank you Prof. Urs Baltensperger for being my doctoral father, and for being such a brilliant scientist. It has been a delight to be able to work with you, your advice and patience have been sincerely appreciated. Thanks to Dr. Imad El Haddad for your extraordinary commitment, there have certainly been highs and lows in the past four years and you have always been a constant source of encouragement and a joy to have as a supervisor. To Dr. Houssni Lamkaddam, I have greatly valued all of your help and guidance, but also your sense of humour and patience. I think we all made a pretty great team.

I also had the pleasure of supervision from Dr. Josef Dommen and Prof. Julia Schmale. Thanks to Josef for introducing me to the world of atmospheric chemistry, it's a shame that it was only for a year but I hope that you are enjoying retirement! Thank you Julia for supporting me through a very difficult CLOUD campaign, and for your supervision and care.

Thank you to my co-examiners Prof. Ruth Signorell and Prof. Gordon McFiggans for agreeing to act as my co-examiners, and for the time you have taken to review my thesis.

To my lovely office mate Mihnea Surdu, I hope that whoever fills my desk is less distracting than me, but just as fun! We've had some fun times and not-so-fun times at various campaigns and schools, but you've always kept me smiling, and somehow you always manage to stay positive. I wish you the best of luck with the rest of your Doctorate, and whatever else the future brings.

I want to thank all of the CLOUD collaboration, especially Mingyi Wang, Neil Donahue, and Jasper Kirkby, who have been fantastic collaborators. I have truly loved being a part of CLOUD, I have had amazing support from colleagues, great collaborations, intense discussions, and I have made friends to keep for a lifetime. So thanks to Birte Rörup, Guillaume Marie, Joschka Pfeifer, Steffen Bräkling, and Stefan Weber, not only for all of your hard work, but for also keeping me sane throughout some tough times.

Many many thanks go to all those at the LAC who have become my work family, especially those who have served time in the group with many names: Andrea Baccarini, David Bell, Lubna Dada, Chuan Ping Lee, Simon Wang, and Mao Xiao.

My final thanks go to all of my friends and family who have continuously supported me. To my Mom and Dad for everything up until this moment, including constantly offering to fly to Switzerland to cook and clean for me as I attempted to finish my Doctorate, even though you

1   Introduction

1.1   Aerosols in the atmosphere

1.1.1   What are aerosols?

Aerosols are small solid or liquid particles (1 nm - 10s µm) which are suspended in air. Aerosols are ubiquitous in our atmosphere and can be divided into many different classifications. The first is primary and secondary aerosols, where primary aerosols are directly emitted into the atmosphere, such as dust, pollen, and salt, and secondary aerosols are formed in the atmosphere by gas-to-particle conversion processes. We can then further separate into natural and anthropogenic (of human influence) in origin. Both natural and anthropogenic aerosols can have a variety of compositions and sources. Some examples of inorganic aerosols are mineral dust, volcanic ash, and various salts. Organic aerosols can be secondary aerosols formed by emissions from plants (biogenic - emitted by living organisms) or formed by any form of fuel burning which can be natural or anthropogenic in nature [1].

Aerosols go through many processes while in the atmosphere, they can grow by condensation of low volatility vapours and vice versa by evaporation of vapours. When two particles collide they may coagulate, which increases the size of the particle and decreases the number of particles. Aerosols may then be removed from the atmosphere by either dry deposition, where particles deposit on a surface, or wet deposition, where particles are incorporated into falling hydrometeors, i.e. liquid, icy, or mixed droplets. The most likely loss process for a particle depends on its size. Aerosols are generally categorised into four size modes: nucleation mode particles (from a stable cluster ~ 1 nm – 10 nm), Aitken mode particles (10 – 100 nm), accumulation mode (100 – 2500 nm) and coarse mode (2.5 µm – 100 µm). Figure 1.1 shows a typical urban atmospheric distribution of these different modes, and presents key formation and removal mechanisms for each mode. Particles in the nucleation mode are formed from gas to particle processes and the main loss process is coagulation with other particles. Aitken mode

particles are mostly primary particles from combustion that then grow via condensation of gases. Accumulation mode particles are formed via coagulation of smaller particles, or condensation onto smaller particles. The accumulation mode gets its name from the fact that the particle loss processes are least effective in this size range, allowing particles to accumulate. Coarse mode particles are primary particles which are formed by mechanical processes, such as salt, soil dust, etc. The main loss process for these particles is dry deposition as they have relatively high sedimentation velocities [2].
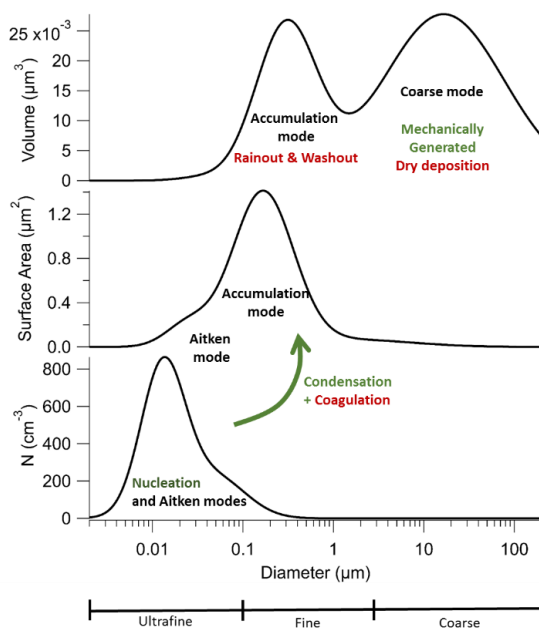
Figure 1.1: Number, surface area, and volume distributions of typical urban aerosols. Adapted from figures in [1] and using model size distributions for an urban atmosphere from [2].

In urban areas, ultrafine particles (< 100 nm) are often measured close to point sources of emissions, for example next to industry or a busy road. The number concentration of these particles decreases as distance from the source increases. The majority of the surface area of particles is found in the accumulation mode and so this is the major sink for condensable gases.

In the presence of haze, the coagulation loss for particles in the nucleation mode is hugely increased, as is the sink for condensable gases. Understanding sources and sinks of aerosols is vital in order to be able to quantify their effect on climate and health.

1.1.2   Climate and health effects

Aerosols affect the global climate in two ways, directly, via aerosol-radiation interactions, and indirectly via aerosol-cloud interactions. The direct effect is through scattering, reflection, and absorption of radiation directly by aerosols. The indirect effect is through scattering, reflection and absorption of radiation by clouds formed by aerosols. The majority of both effects is scattering and reflecting, resulting in a negative temperature forcing on the global climate, black carbon aerosols are the exception as they absorb radiation. Aerosols cause the indirect effect due to their role as cloud condensation nuclei (CCN) which then can form clouds. To become CCN, aerosols must grow large enough as CCN are typically around 100 nm. Primary and secondary aerosols both contribute similarly to the total global CCN and aerosol budget. Figure 1.2 from IPCC 2013 shows that for radiative forcing, aerosol-radiation interactions (direct effect) and aerosol-cloud interactions (indirect effect) are mostly negatively forcing, but also have large error bars [3]. As the total forcing from aerosols may be offsetting over 1.5 W m^{-2} (almost 1 °C) it is important to understand aerosol formation and growth, and try to learn more precisely what the offset is, so that proper steps can be taken to combat climate change.
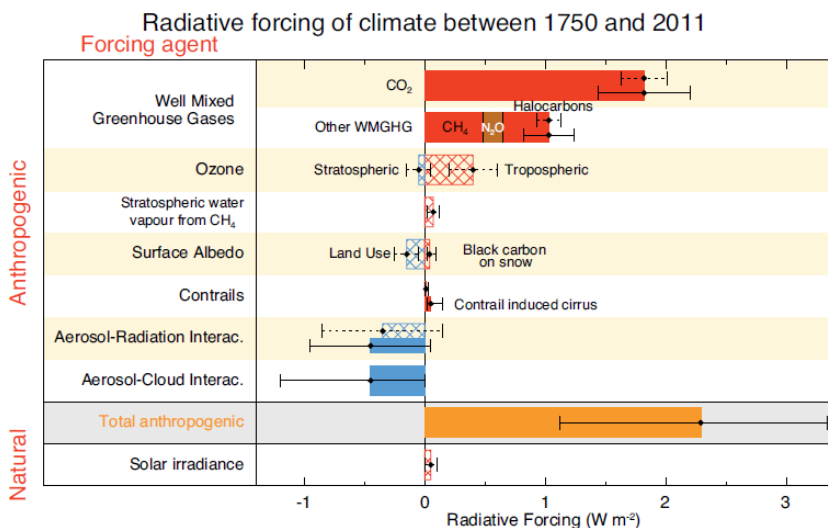
Figure 1.2: Figure from IPCC 2013 showing the radiative forcing (RF) and effective radiative forcing (ERF) of climate change during the industrial era. The solid bars show the RF by concentration change of various forcing agents. The hatched bars show ERF. The black error bars represent the uncertainty [3].

As well as their effect on the climate, aerosols also have a negative impact on health. Figure 1.3 shows deposition as a function of particle size for different areas of the respiratory tract. We can see that the size of the particle has a large impact on where the particles will deposit. This will in turn determine what impact the particles have on the body. Large enough particles (10-30 µm) will deposit in the nose and throat, and will most likely be removed by mucus. Smaller particles (3-10 µm) are able to deposit deeper in the lungs into the trachea, bronchi and bronchioles. Even smaller still (0.1-3 µm) can deposit even deeper in the lungs on the pulmonary alveoli and the smallest of particles (<0.1 µm) can penetrate pulmonary tissue and enter the blood stream and cause cardiovascular diseases [4]. Pathophysiological effects of the different deposition sites are shown in Table 1.1, from [5]. The composition of particles will also have an impact, for example, oxidative aerosols will cause tissue damage, and transition metal particles can cause toxicity and carcinogenic effects when inhaled [6]. Gas deposition depends on its solubility in water, some common pollutants are also listed in Figure 1.3. The WHO has reported

that in 2019 lower respiratory infections were the fourth leading cause of deaths globally, making it the world's most deadly communicable disease. This is even promoted to the second leading cause of death in low-income countries. Lower respiratory infections are also the fourth leading cause of disability-adjusted life years (DALYs), where one DALY is equivalent to losing one year of full health [7], [8]. Due to the fact that small particles have the potential to cause more damage, $PM_{2.5}$ (mass concentration of particles less than 2.5 μm) and PM_{10} (mass concentration of particles less than 10 μm) are typical monitored species in cities and often policies to decrease health effects of pollution are based on these measurements [9].
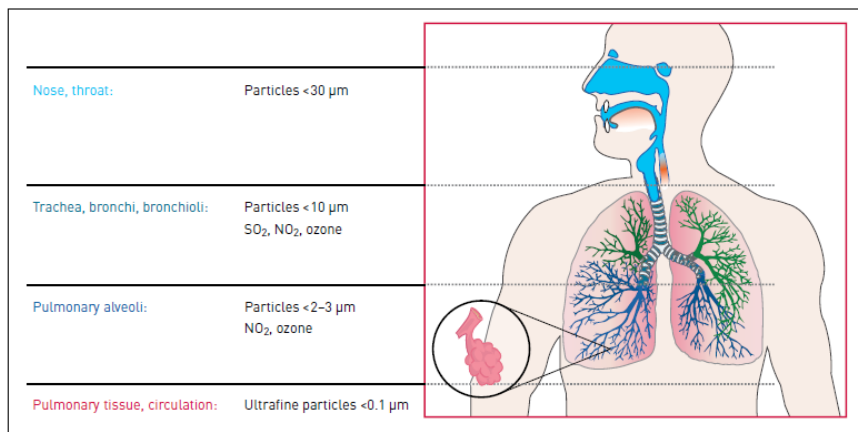

Figure 1.3: Figure from [5] showing the most likely deposition places of different sized aerosols.

Table 1.1: Re-formatted from [5] listing general pathophysiological effects of different deposition sites of inhaled pollutants.

Trachea, Bronchi	♦ Irritation of mucous membranes, local inflammation, changes in mucous compounds, immigration of inflammatory and immune defence cells ♦ Impairment of ciliary activity, impairment of epithelial clearance, e.g. of upward transport of particles, bacteria, etc. ♦ Constriction of bronchia through muscular spasm and swelling of mucosa
Pulmonary Alveoli	♦ Impairment of ability of immune cells to ingest and dissolve foreign material and debris ♦ Local inflammation, change in permeability of cell membranes ♦ Transfer of inflammatory proteins and of ultrafine particles in the pulmonary tissue and the circulation
Circulation	♦ Inflammation in endothelia of blood vessels, enhanced formation of plaques, coagulation, thrombosis ♦ Changes in regulation of autonomic nervous system, e.g. heart rate variability.

1.2   New particle formation and growth

Nucleation makes up around 50% of the total CCN global budget, and can even approach 100% in certain environments [10]. Nucleation of aerosols is a gas-to-particle process where a stable critical cluster is formed from gas molecules, it is a first order phase transition and typically requires overcoming an energy barrier.

Nucleation is often represented by measured new particle formation rate, J_x, where x is the diameter of the particle. Particles of a certain size (usually 1-3 nm) are measured, and the formation rate of these particles is calculated by the simplified Equation (1.1), where the loss rates are subtracted from the change in concentration over time, to give the formation rate of a certain particle size in molecules cm^{-3} s^{-1}. N_x is the concentration of particles of x diameter in particles cm^{-3} and t is the time in seconds.

$$J_x = \frac{dN_x}{dt} - losses \qquad (1.1)$$

Once a critical cluster is formed, in order to grow into the accumulation mode, where particle lifetimes are longest and particles can become cloud condensation nuclei (CCN), it needs to grow to ~100 nm without being removed by one of the removal processes shown in Figure 1.1. The likelihood of this happening will depend on the relationship between loss rates and growth rates. As previously discussed, the major sink for nucleation mode particles is coagulation with larger particles, and so the survival rate will depend heavily on the ratio between the growth rate and condensation sink (CS). The nucleation mode can also be referred to as the "valley of death" as this is the size range where particles are least likely to survive growth. Figure 1.4 shows ambient measurements of nucleation and growth. The red "banana" marked by a black border is a nucleation event which starts with a relatively clean particle background, where a large amount of small particles grow up to around 100 nm. After this time there is a pollution event, characterised by the presence of large particles forming a high condensation sink (orange rectangle), and there are no longer many small (< 30 nm) particles.
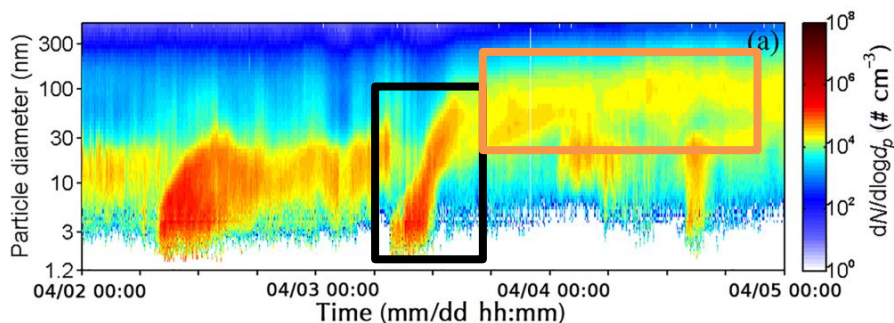
Figure 1.4: Ambient particle size distributions from [11] intended to represent a typical new particle formation and pollution event from a city. The measurements were taken in Beijing between the 2nd and 4th April 2016.

Nucleation scientists have already explored many different parameters of nucleation in different environments. The current state of the art is that the ternary system H_2SO_4-NH_3-H_2O is generally agreed to be the responsible mechanism for the majority of new particle formation in urban areas, and dimethylamine (DMA) and other amines can enhance nucleation rates several orders

of magnitude [12]. There is continuously ongoing research into nucleating species, for example; in marine environments, iodine oxoacids are key nucleation species, highly oxygenated molecules (HOMs) of terpenes are the major nucleating gases over boreal forests, and HOMs of aromatic compounds will participate in nucleation and growth in polluted areas [13]–[15].

Figure 1.5 shows new particle formation rates of 1.7 nm versus growth rates for < 3 nm particles, from experiments at the CLOUD chamber at CERN. These results are overlaid onto ranges of growth and new particle formation (NPF) rates from atmospheric observations. Here we can observe that while the nucleation rates span four orders of magnitude, the growth rates only span one. If we focus on one chemistry, for example H_2SO_4+NH_3+Org at 278 K, adding DMA to the system results in a 10 to 15 times increase in nucleation, but no increase in growth rate. This is because, while amines increase the nucleation rate, they do not contribute to growth, due to their low concentration. The takeaway message is that, although polluted areas with ammonia, amines, sulfuric acid and HOMs may have higher particle formation rates, we cannot explain the sustained particle number in polluted areas, since the growth measured should not be high enough to overcome the condensation sink.
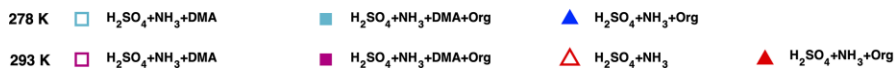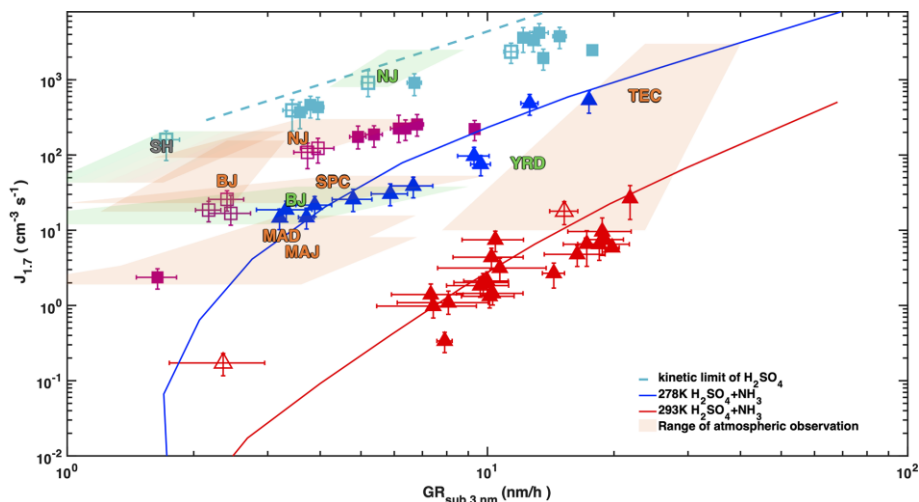
Figure 1.5: Formation rates versus growth rates for different chemical systems from CLOUD experiments with ambient ranges, from [12]. Experiments at the CLOUD chamber were measured at 278 K (blue and cyan) and 293 K (red and magenta). Filled shapes are experiments in the presence of organics, and vice versa for open symbols. Squares are experiments with DMA present and triangles without. The solid lines represent simulated rates using a kinetic model. The coloured letters represent mean values and the shaded areas represent the ranges of atmospheric observations in the following locations: Shanghai (SH) [16], Beijing spring and winter (BJ) [11], [17], Madrid (urban: MAD and suburban: MAJ) [18], Po Valley regional (San Pietro Capofiume, SPC) [19], Nanjing summer and winter (NJ) [20], Yangtze River Delta regional (YRD) [21], and Tecamac (TEC) [22]. The colour of the text and shaded areas indicate the temperature of the measurements where < 288 K is green and > 288 K is orange and all year is in grey.

The survival probability of any given particle is calculated by Equation (1.2) [23]:

$$J_2 = J_1 \exp\left[0.23 \frac{CS'}{GR'}\left(\frac{1nm}{d_1} - \frac{1nm}{d_2}\right)\right] \tag{1.2}$$

Where J_1 and d_1 are the formation rate and diameter of the larger particle and J_2 and d_2 are of the smaller particle, the condensation sink (CS) term CS' = CS*β/ (10^{-4} s^{-1}) and the growth rate (GR) term GR' = GR/ (1 nm hr^{-1}). β is the collision efficiency of clusters to the condensation sink;

when every collision results in coagulation then $\beta = 1$. Figure 1.6 is from [23] and shows how J_3 varies with increasing CS'/GR'. J_{A-D} are calculated using Equation (1.2) and the data points are from various atmospheric observations. There is a clear disconnect between the model and the data. Key assumptions in J_A are that growth between 1.5 and 3 nm is 1 nm hr^{-1}, and $\beta = 1$. J_B changes the assumption to 2 nm hr^{-1}, J_C assumes that the clusters between 1.5 and 2 nm are scavenged at 10% efficiency ($\beta = 0.1$), and J_D includes the changes from J_B and J_C. The authors therefore state that if "the small clusters are not scavenged as efficiently as the measured value of CS indicates" or "growth rates of the smallest clusters were much larger (by a factor of 5–20)", this could explain the observations.
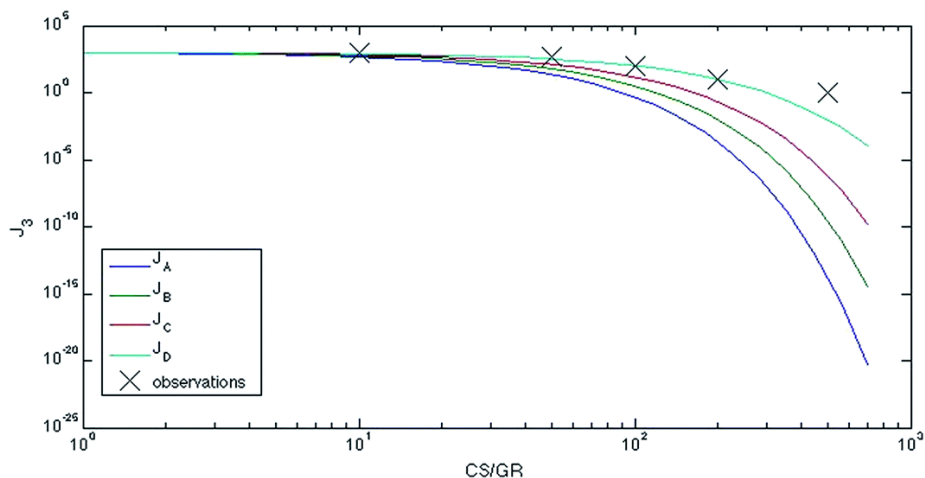
Figure 1.6: Figure from [23] CS/GR vs J_3 for observations and four different models. J_{A-D} were calculated using equation (1.2). J_A: GR = 1 nm hr^{-1}, $\beta = 1$. J_B: GR = 2 nm hr^{-1}, $\beta = 1$. J_C: GR = 1 nm hr^{-1}, $\beta = 0.1$. J_D: GR = 2 nm hr^{-1}, $\beta = 0.1$. Observations are from Hyytiälä, Finland (Remote), San Pietro Capofiume, Italy (Urban), and Shanghai, China (Urban).

From Figure 1.5 we know that growth rates up to 20 nm hr^{-1} are possible with normal urban atmospheric conditions. However, there is no experimental proof that these growth rates would in fact increase survival, nor is there evidence that cluster scavenging by a condensation sink is

as efficient as is currently believed, i.e. β = 1. These will be main goals of this thesis and are explained in more detail in the section Objectives.

1.3   Ammonium nitrate

Ammonium nitrate (NH_4NO_3) is an important constituent of aerosols, especially in winter due to its semi-volatile nature. NH_4NO_3 is formed on particles by the partitioning of gas phase NH_3 and HNO_3 to the particle, and subsequent salt formation.

1.3.1   Sources of ammonia

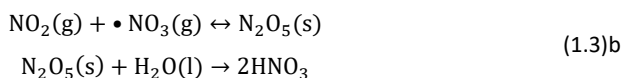Ammonia is ubiquitous in the troposphere and has many sources. The major sources, in order of descending global emissions, are agricultural, natural (oceans, soil, animals), and biomass burning [1]. Although agricultural emissions dominate the global emissions, in an urban area non-agricultural emissions, such as urban waste and fossil fuel related emissions such as traffic, can be just as important sources. Urban concentrations range from a few ppbv, to tens of ppbv [24]–[26].

1.3.2   Sources of nitric acid

Nitric acid is formed in the atmosphere through two main pathways, Equations (1.3 a-b). Equation (1.3)a is the dominant chemistry in the daytime, due to the presence of •OH from photolysis by sunlight. Equations (1.3)b are heterogeneous, and the main chemistry during the night due to the presence of •NO_3.

$$NO_2(g) + \bullet\, OH(g) + M \rightarrow HNO_3(g) + M \tag{1.3a}$$

$$NO_2(g) + \bullet\, NO_3(g) \leftrightarrow N_2O_5(s)$$
$$N_2O_5(s) + H_2O(l) \rightarrow 2HNO_3 \tag{1.3b}$$
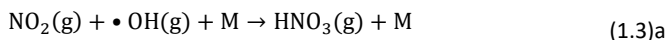
Nitric acid daytime urban concentrations are typically up to a few ppbv, the concentration varies dramatically throughout the day due to the change in chemistry, HNO_3 concentrations are higher during the daytime, and lower at night.

1.3.2.1 NO_x

Since nitric acid is formed from NO_2, it is important to know the sources and reactions of NO_2. NO_2 is in constant equilibrium with NO in the atmosphere, and both are often discussed together and referred to as NO_x. Natural sources of NO_x include emissions from soils and lightning, which are globally significantly lower than anthropogenic sources. Anthropogenic emissions are dominated by those from fossil fuel combustion and industrial processes, but other sources are agriculture, and biomass and biofuel burning [1], [3]. Sources from traffic are of key importance in cities, and also cause inhomogeneities in the NO_X concentrations. A typical mass fraction of nitrate in urban aerosols is 10-20% but is highly temperature dependent, with higher values in winter. Values as high as 39-43% of PM_1 are reported during severe haze episodes in winter in Kim *et al.* [27]–[30].

1.3.3   Contribution to aerosols

Recent studies show that nitrate concentrations in aerosols can be especially high, exceeding typical urban mass fractions by a few percent, during haze events in megacities and in nucleation events, implying that nitrate may be a key player in haze formation or maintenance [31]–[35]. Figure 1.7 and Figure 1.8 show the mass fractions and time-series of aerosols during a pollution event in Beijing, during which not only is nitrate a large fraction, but it also increases throughout the pollution period from 6% during the clean periods to 12% in the polluted periods [32].
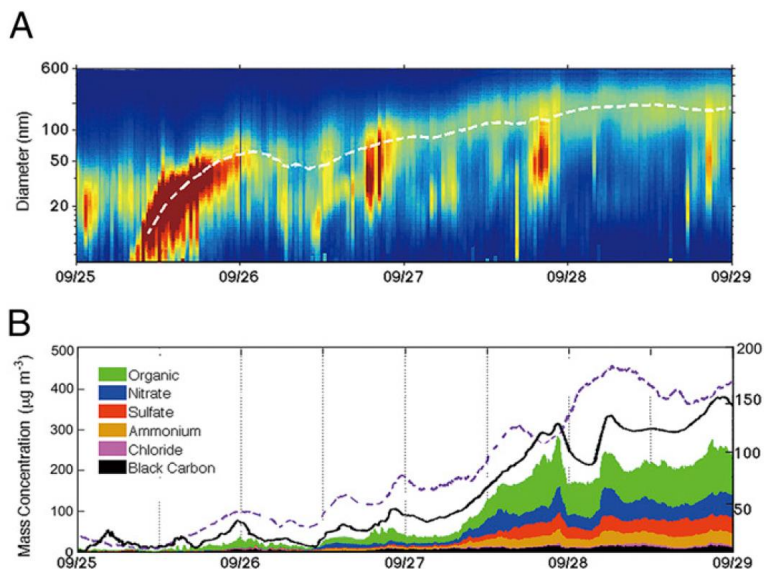
Figure 1.7: Aerosol nucleation and growth from a campaign during a pollution event in Beijing from [32]. **A** shows particle size distributions and the mean diameter (white dashed line). **B** shows the PM$_{2.5}$ mass concentration as the black solid line, mean diameter as the purple dashed line, and PM$_1$ chemical composition (legend of **B**).
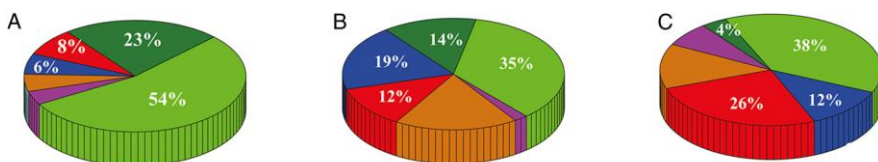
Figure 1.8: Particle chemical compositions from a progressing nucleation and pollution event from [32]. **A-C** are from the same experiment as A in Figure 1.7. They were taken at different times during the experiment meant to represent the clean (**A**) transition (**B**) and polluted (**C**) periods. **A** shows 80 nm particle composition, **B** is 100 nm and **C** is 240 nm. The sizes were chosen to be close to the mean size at the time of measurement.

Condensation of ammonium nitrate onto aerosols involves three fully reversible processes shown in Equations (1.4)-(1.6).

$$NH_3(g) \rightleftarrows NH_3(s) \tag{1.4}$$

$$HNO_3(g) \rightleftarrows HNO_3(s) \tag{1.5}$$

$$NH_3(s) + HNO_3(s) \rightleftarrows NH_4 \cdot NO_3(s) \tag{1.6}$$
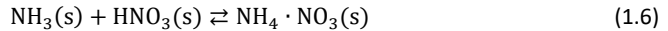
Mozurkewich [36] gives a temperature (T) dependent overall dissociation constant (K_p) of ammonium nitrate for solid-vapour in Equation (1.7), this is valid for conditions where the relative humidity (RH) is lower than the deliquescence relative humidity (DRH).

$$\ln(K_p/ppb^2) = 118.87 - \frac{24084}{T} - 6.025 \ln(T) \tag{1.7}$$

The saturation of ammonium nitrate is defined as $S = NH_3(g) \times HNO_3(g)/Kp$. Therefore, if $S > 1$ then the concentration product of $NH_3(g)$ and $HNO_3(g)$ is greater than the value of K_p and condensation of ammonium nitrate can occur.

Figure 1.9 shows the temperature dependence of K_p, which varies several orders of magnitude compared to temperature variation of 10s of degrees, typical ambient temperature changes within a year.

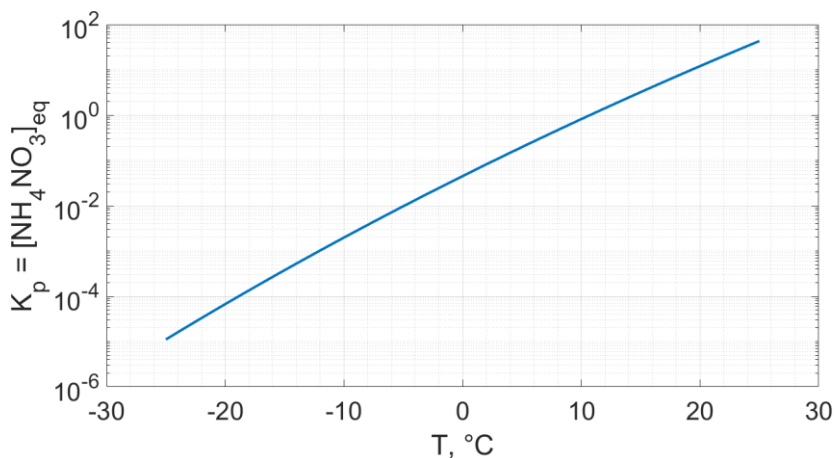**Figure 1.9: Temperature dependence of K_p between -25 and +25 °C calculated using Equation (1.7).**

Measurements from polluted environments show us that nitrate concentrations in particles vary throughout the day, with the maximum concentrations in the early morning, and minimum concentrations in the afternoon [37]. This can be partially attributed to the fact that lower temperatures drive more condensation. Other effects that contribute to the maximum in the morning are the changing boundary layer and rush hour. Evaporation due to higher temperature in the afternoon is responsible for the minimum in concentration. Another result of the temperature dependence of K_p is that typically the fraction of particulate mass from ammonium nitrate is highest in winter and lowest in summer, as the higher temperatures favour evaporation of ammonia and nitric acid, and vice versa. The equilibrium value of $NH_3 \times HNO_3$ is lower at lower temperatures, and thus more ammonium nitrate can condense onto particles for the same gas phase concentrations than at higher temperatures [1], [38]. An exception to this is in areas where the sources of nitric acid and/or ammonia are much higher in summer than winter, for example emissions from agriculture. However, in urban areas the sources of nitric acid may be higher in winter, especially if many households use coal or other fuels for heating, as NO_X emissions are associated with fossil fuel and biofuel burning. NO_X concentrations are also increased in winter due to compression of the boundary layer [39].

Despite nitric acid being an important constituent of aerosol mass, nitric acid was assumed to be too volatile to contribute to early growth of particles, and the presence of nitrate was deemed to be due to condensation on larger particles only, and is also contributed to by organo-nitrates [37], [40]. Nitric acid has also not been observed to participate in nucleation. In previous studies at the CLOUD chamber at CERN, nitric acid has been detected in the particle phase in particles < 6 nm by a FIGAERO-CIMS (Filter Inlet for Gases and AEROsols – Chemical Ionisation Mass Spectrometer), suggesting that nitric acid may contribute to early growth of aerosols (unpublished results, CLOUD 2017).

1.4   The CLOUD experiment

The CLOUD (Cosmics Leaving OUtdoor Droplets) chamber at CERN (European Organization for Nuclear Research) was initially conceptualised in order to investigate the effect of galactic cosmic rays on new particle formation. It has since evolved to study new particle formation under many different atmospherically relevant conditions, as well as studying aerosol chemistry, growth, ice nucleation, and further relevant topics.

The chamber is 26.1 cubic meters and made of stainless steel where the inside is electro polished, a schematic of the chamber is shown in Figure 1.10. By varying different flows of wet and dry air into the chamber, we have the capability to keep constant relative humidity. The CLOUD chamber is also equipped with temperature control from −65 - +100 °C precise to ± 0.1 °C. Trace gases used each have a separate injection system so that there is no contamination between different experiments. The chamber is also equipped with light sources of different wavelengths allowing for focus on different photochemistry in different experiments.

The CLOUD facilities are ideal for studying new particle formation and growth since the stainless steel walls allow the chamber to be cleaned very efficiently. This allows for secondary aerosols to be formed and grown from controlled gases without unwanted influence from contaminants.

Furthermore, the experiment is equipped with state of the art instrumentation for monitoring many variables and concentrations.
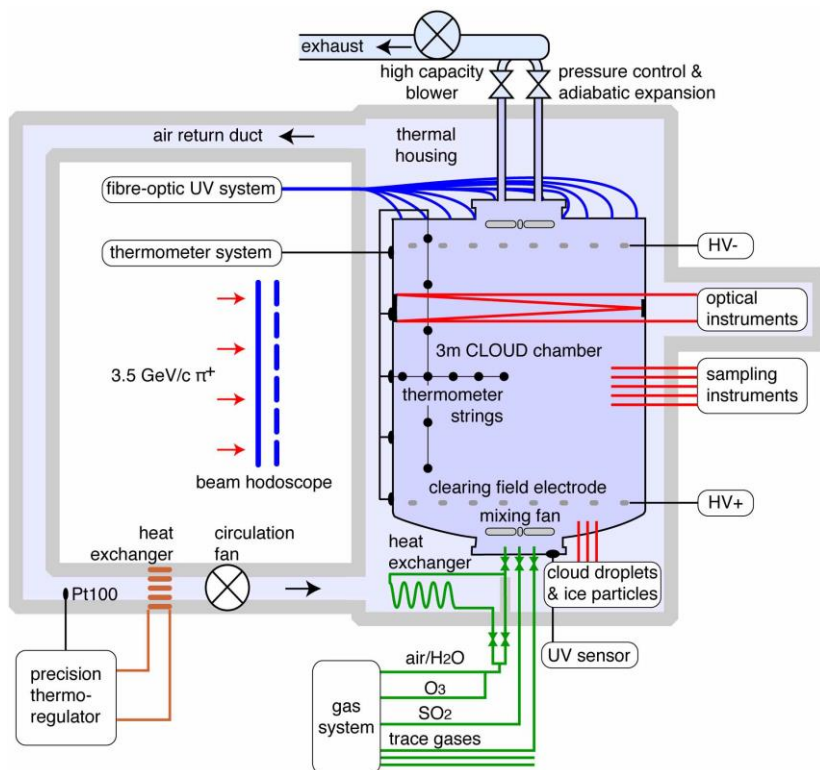
Figure 1.10: Schematic of the CLOUD chamber at CERN as of 2013 (from [41]).

Concentration time-series of trace gases NO, SO_2 and ozone are measured by gas monitors; ECO Physics, CLD 780TR, Thermo Fischer Scientific Inc. 42i-TLE, and Thermo Environmental Instruments, TEI 49C respectively. NO_2 is measured by a cavity attenuated phase shift NO_2 monitor (CAPS NO_2, Aerodyne Research Inc.). A custom-made cavity-enhanced differential optical absorption spectrometry instrument (CE-DOAS) was also deployed to measure NO_2 and HONO. Relative humidity and temperature of the chamber are also measured constantly.

Temperature is monitored by mid-plane internal PT100 temperature sensors inside the CLOUD chamber, at five different distances from the chamber wall. The sensor closest to the midpoint of the chamber is used as the chamber's reference temperature, and the other four are used to monitor homogeneity of temperature. Relative humidity is measured by two instruments, dew point mirrors (EdgeTech) and an in-situ tuneable diode laser (TDL) hygrometer (KIT, CERN).

There are several mass spectrometers that measure volatile organic compounds (VOCs), semivolatile VOCs (SVOCs), HOMs, sulfuric acid, nitric acid, ammonia, and dimethylamine (DMA). Two custom built proton transfer reaction time of flight mass spectrometers (PTR-ToF-MS) measure VOCs and SVOCs. These are a selective reagent ionization time of flight mass spectrometer (SRI-ToF-MS) and a PTR3-ToF-MS described in [42] and [43] respectively. HOMs and H_2SO_4 are measured by two NO_3^- chemical ionisation atmospheric pressure interface ToF-MS (CI-API-ToF-MS). One instrument is equipped with an Aerodyne inlet, and the second uses a home-made inlet with corona discharge for ion generation, described in [44]. HNO_3 is measured by a Br^- CI-API-ToF-MS. Ammonia and DMA are measured by a water cluster CI-API-ToF-MS, described in [45].

Particle measurements are taken by several instruments with the total size range covered being 1.8 – 487 nm. These instruments are, in size order, a particle size magnifier (PSM) [46], a differential mobility analyser train (DMA-Train) [47], a nano-scanning electrical mobility spectrometer (nSEMS) [48], a nano-scanning mobility particle sizer (nano-SMPS), and a long SMPS.

Formation rates are calculated from particle number distributions measured by the PSMs. Growth rates can be calculated from all instruments, and where instruments overlap inter-comparisons can ensure more certain results. Other parameters such as the condensation sink, are also calculated from particle size distributions.

Figure 1.11 shows a typical CLOUD nucleation experiment. Here, we identify the three parts of any experiment, the experiment itself, and cleaning before and after. This example was an experiment with nucleation and growth by H_2SO_4 and NH_3. SO_2, O_3 and NH_3 were injected and

kept constant in step 1. Particles cannot form from these gases and so there is no new formation, the fans in the chamber are at 100% power so as to clean particles and condensable gases from previous experiments. Additionally, a high voltage electric field is created within the chamber in order to remove ions by use of a field cage with voltages applied to two electrodes inside of the chamber. In step 2, the light is turned on, in this case a UV light, so that photolysis of O_3 leads to •OH formation, and reaction of SO_2 and OH forms H_2SO_4. This shape of particle formation and growth is often referred to as a "banana". The banana grows to around 10 nm and then the experiment is deemed finished, as we can calculate nucleation and growth rates from this banana (often the goal of experiments). The lights are then turned off and stage 3 is a second cleaning stage in preparation for the next experiment. Due to these experiments taking place during the long shutdown 2 at CERN, all experiments were performed without use of the 3.5 48 GeV/c secondary pion beam (π beam) from the CERN PS.
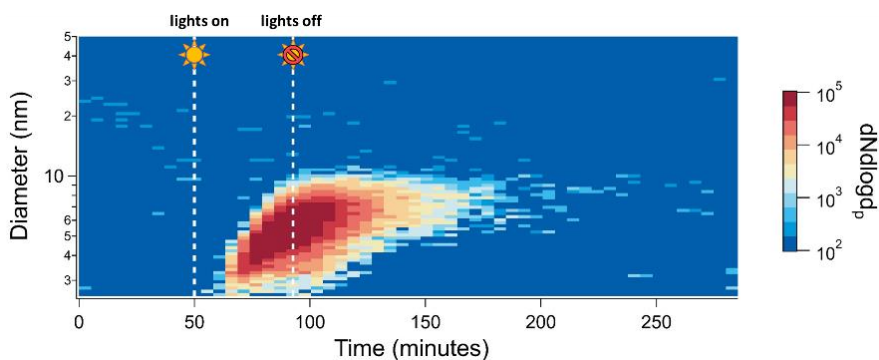
Figure 1.11: Particle size distribution evolution during a nucleation experiment from CLOUD experiments in 2018, meant to represent a typical experiment plan. Step 1 is a cleaning stage before nucleation begins, lights are off so there is no photochemistry, fans are high so as to increase turbulence and therefore wall losses of particles and condensable gases that may have been present from the previous experiment. A high voltage electric field is also generated to remove all ions from the chamber. This step is also used to get the gases required for step 2 to steady state. Step 2 is the nucleation and growth experiment, UV lights are on so that production of •OH and therefore oxidised condensable gases occurs and the fans are set to the optimum speed for chamber mixing. Nucleation then begins and the stage is ended by turning off the lights when the particles are large enough for the purpose of the experiments. Step 3 is then a repeat of step 1.

1.5   Modelling nucleation and growth of aerosols

Models can be used to verify understanding of experimental measurements, as well as to further explore different conditions. A kinetic model of sulphuric acid and ammonia nucleation and growth was developed in [12] based on the general dynamic equation from [1]. The model was validated using data from CLOUD chamber and ambient measurements. This model was further developed to include growth from NH_4NO_3 at different temperatures and was further validated using CLOUD data. Briefly, NH_4NO_3 growth is modelled analogous to CCN formation. This model is described in detail in sections 0 and 0.

1.6   Objectives

As has been highlighted in this Introduction, there are gaps in the current knowledge of formation and growth of aerosols in urban environments. Since it has been shown that aerosols have an important effect on climate and local climate, as well as health, unravelling the mystery of particle survival in polluted environment is fundamental if we want to mitigate these issues. Understanding the drivers behind these phenomena will allow us to more accurately model the atmosphere and understand our impact on it, as well as making informed decisions on policies to reduce air pollution.

This thesis will be made up of three results chapters, the first chapter will focus on investigating the role of ammonium nitrate condensation in the growth of aerosols.

The first question to answer is whether or not ammonium nitrate condensation can occur in small (<10 nm) aerosols, and have an impact on the growth rates of the particles. The variables investigated are the effect of concentrations of nitric acid and ammonia, and temperature. The second question will then be whether nitric acid and ammonia can cause nucleation of new aerosols in the absence of other known nucleating species.

The second chapter will investigate experimentally how high growth rates affect survival of particles under high condensation sinks. The experiments presented are undertaken at the CLOUD chamber at CERN, and will generate a high condensation sink and attempt nucleation and growth under these conditions. These experiments will also be used to determine the effect of a condensation sink on cluster loss rate. Furthermore a kinetic model is developed to simulate ammonium nitrate growth on aerosols and to verify survival of particles under high condensation sink as measured in CLOUD.

Chapter 3 will focus on altering the kinetic model from Chapter 2 to an ambient box model. The simulations will include typical urban inhomogeneities of temperature change due to vertical mixing of an air packet, and local emissions of NH_3 from traffic. This chapter will answer whether these rapid and small perturbations from equilibrium are sufficient to grow particles through the valley of death and sustain haze.

2 Rapid growth of new atmospheric particles by nitric acid and ammonia condensation

Mingyi Wang[1,2,30], Weimeng Kong[3,30], Ruby Marten[4], Xu-Cheng He[5], Dexian Chen[1,6], Joschka Pfeifer[7], Arto Heitto[8], Jenni Kontkanen[5], Lubna Dada[5], Andreas Kürten[9], Taina Yli-Juuti[8], Hanna E. Manninen[7], Stavros Amanatidis[3], António Amorim[10], Rima Baalbaki[5], Andrea Baccarini[4], David M. Bell[4], Barbara Bertozzi[11], Steffen Bräkling[12], Sophia Brilke[13], Lucía Caudillo Murillo[9], Randall Chiu[14], Biwu Chu[5], Louis-Philippe De Menezes[7], Jonathan Duplissy[5,15], Henning Finkenzeller[14], Loic Gonzalez Carracedo[13], Manuel Granzin[9], Roberto Guida[7], Armin Hansel[16,17], Victoria Hofbauer[1,2], Jordan Krechmer[18], Katrianne Lehtipalo[5,19], Houssni Lamkaddam[4], Markus Lampimäki[5], Chuan Ping Lee[4], Vladimir Makhmutov[20], Guillaume Marie[9], Serge Mathot[7], Roy L. Mauldin[1,2,21], Bernhard Mentler[16], Tatjana Müller[9], Antti Onnela[7], Eva Partoll[16], Tuukka Petäjä[5], Maxim Philippov[20], Veronika Pospisilova[4], Ananth Ranjithkumar[22], Matti Rissanen[5,23], Birte Rörup[5], Wiebke Scholz[16,17], Jiali Shen[5], Mario Simon[9], Mikko Sipilä[5], Gerhard Steiner[16,24], Dominik Stolzenburg[5,13], Yee Jun Tham[5], António Tomé[25], Andrea C. Wagner[9,14], Dongyu S. Wang[4], Yonghong Wang[5], Stefan K. Weber[7], Paul M. Winkler[13], Peter J. Wlasits[13], Yusheng Wu[5], Mao Xiao[4], Qing Ye[1,2,26], Marcel Zauner-Wieczorek[9], Xueqin Zhou[4], Rainer Volkamer[14], Ilona Riipinen[27], Josef Dommen[4], Joachim Curtius[9], Urs Baltensperger[4], Markku Kulmala[5,15,28,29], Douglas R. Worsnop[5,18], Jasper Kirkby[7,9], John H. Seinfeld[3], Imad El-Haddad[4], Richard C. Flagan[3] & Neil M. Donahue[1,6,2,26]

[1]Center for Atmospheric Particle Studies, Carnegie Mellon University, Pittsburgh, PA, USA.
[2]Department of Chemistry, Carnegie Mellon University, Pittsburgh, PA, USA.
[3]Division of Chemistry and Chemical Engineering, California Institute of Technology, Pasadena, CA, USA.
[4]Laboratory of Atmospheric Chemistry, Paul Scherrer Institute, Villigen, Switzerland.
[5]Institute for Atmospheric and Earth System Research (INAR), University of Helsinki, Helsinki, Finland.
[6]Department of Chemical Engineering, Carnegie Mellon University, Pittsburgh, PA, USA.
[7]CERN, the European Organization for Nuclear Research, Geneva, Switzerland.
[8]Department of Applied Physics, University of Eastern Finland, Kuopio, Finland.
[9]Institute for Atmospheric and Environmental Sciences, Goethe University Frankfurt, Frankfurt am Main, Germany.
[10]CENTRA and Faculdade de Ciências da Universidade de Lisboa, Campo Grande, Lisbon, Portugal.
[11]Institute of Meteorology and Climate Research, Karlsruhe Institute of Technology, Karlsruhe, Germany.
[12]Tofwerk, Thun, Switzerland.
[13]Faculty of Physics, University of Vienna, Vienna, Austria.
[14]Department of Chemistry and CIRES, University of Colorado at Boulder, Boulder, CO, USA.
[15]Helsinki Institute of Physics, University of Helsinki, Helsinki, Finland.
[16]Institute for Ion Physics and Applied Physics, University of Innsbruck, Innsbruck, Austria.
[17]Ionicon Analytik, Innsbruck, Austria.
[18]Aerodyne Research, Billerica, MA, USA.
[19]Finnish Meteorological Institute, Helsinki, Finland.
[20]P.N. Lebedev Physical Institute of the Russian Academy of Sciences, Moscow, Russia.
[21]Department of Atmospheric and Oceanic Sciences, University of Colorado at Boulder, Boulder, CO, USA.
[22]School of Earth and Environment, University of Leeds, Leeds, UK.
[23]Aerosol Physics Laboratory, Physics Unit, Faculty of Engineering and Natural Sciences, Tampere University, Tampere, Finland.
[24]Grimm Aerosol Technik Ainring, Ainring, Germany.
[25]Institute Infante Dom Luíz, University of Beira Interior, Covilhã, Portugal.
[26]Department of Engineering and Public Policy, Carnegie Mellon University, Pittsburgh, PA, USA.
[27]Department of Applied Environmental Science, University of Stockholm, Stockholm, Sweden.
[28]Joint International Research Laboratory of Atmospheric and Earth System Sciences, Nanjing University, Nanjing, China.
[29]Aerosol and Haze Laboratory, Beijing Advanced Innovation Center for Soft Matter Science and Engineering, Beijing University of Chemical Technology, Beijing, China.
[30]These authors contributed equally: Mingyi Wang, Weimeng Kong.

2.1 Declaration of author contribution

Although I am not the first author of this publication, my contribution has been significant. In the 2017 CLOUD campaign I started my Doctoral studies, it was here where Mingyi Wang from CMU first detected nitrate in sub 10 nm particles. After these results, I led the Urban experimental planning for the next CLOUD campaign. After we decided on the parameters we wanted to explore I modelled every planned experiment in order to calculate •OH concentrations, and subsequent reaction with NO_2 to form HNO_3, SO_2 to form H_2SO_4, and HOMs from VOCs. I then calculated the necessary injection rates and other chamber conditions needed for each stage. As well as planning the experiments I was the lead coordinator on ensuring that the experiments went to plan, as well as adapting ongoing experiments as new information came to light. Throughout the campaign and afterwards we had ongoing meetings in order to understand the newly discovered mechanism where I was a key contributor to discussions. As well as taking a leading role in experimental planning, execution and analysis, I was also responsible for several instruments measuring during the experiments, including the NO (NO, ECO Physics, CLD 780TR) and NO_2 (CAPS NO2, Aerodyne Research Inc.) instruments, whose time-series were essential for determining the production rate of HNO_3. I also took part in the manuscript writing.

2.3   Abstract

New-particle formation is a major contributor to urban smog [16], [49], but how it occurs in cities is often puzzling [23]. If the growth rates of urban particles are similar to those found in cleaner environments (1–10 nanometers per hour), then existing understanding suggests that new urban particles should be rapidly scavenged by the high concentration of pre-existing particles. Here we show, through experiments performed under atmospheric conditions in the CLOUD chamber at CERN, that below about +5 degrees Celsius, nitric acid and ammonia vapours can condense onto freshly nucleated particles as small as a few nanometers in diameter. Moreover, when it is cold enough (below −15 degrees Celsius), nitric acid and ammonia can nucleate directly through an acid–base stabilization mechanism to form ammonium nitrate particles. Given that these vapours are often one thousand times more abundant than sulfuric acid, the resulting particle growth rates can be extremely high, reaching well above 100 nanometers per hour. However, these high growth rates require the gas-particle ammonium nitrate system to be out of equilibrium in order to sustain gas-phase supersaturations. In view of the strong temperature dependence that we measure for the gas-phase supersaturations, we expect such transient conditions to occur in inhomogeneous urban settings, especially in wintertime, driven by vertical mixing and by strong local sources such as traffic. Even though rapid growth from nitric acid and ammonia condensation may last for only a few minutes, it is nonetheless fast enough to shepherd freshly nucleated particles through the smallest size range where they are most vulnerable to scavenging loss, thus greatly increasing their survival probability. We also expect nitric acid and ammonia nucleation and rapid growth to be important in the relatively clean and cold upper free troposphere, where ammonia can be convected from the continental boundary layer and nitric acid is abundant from electrical storms [50], [51].

2.4   Introduction

The formation of new particles may mask up to half of the radiative forcing caused since the industrial revolution by carbon dioxide and other long-lived greenhouse gases [3]. Present-day particle formation is thought to predominantly involve sulfuric acid vapours globally [10], [52], [53]. Subsequent particle growth is richer, often involving organic molecules [54]. Often growth is the limiting step for the survival of particles from freshly nucleated clusters to diameters of 50 or 100 nm, where they become large enough to directly scatter light and also to seed cloud formation [55], [56].

New-particle formation in megacities is especially important [16], in part because air pollution in megacities constitutes a public health crisis [57], but also because the regional climate forcing associated with megacity urban haze can be large [58]. However, new-particle formation in highly polluted megacities is often perplexing, because the apparent particle growth rates are only modestly faster (by a factor of roughly three) than growth rates in remote areas, whereas the vapour condensation sink (to background particles) is up to two orders of magnitude larger (Figure 2.5, SI). This implies a very low survival probability in the 'valley of death', where particles with diameters (d_p) of 10 nm or less have high Brownian diffusivities and will be lost by coagulational scavenging unless they grow rapidly [52], [59].

Ammonium nitrate has long been recognized as an important yet semivolatile constituent of atmospheric aerosols [60]. Especially in winter and in agricultural areas, particulate nitrate can be a substantial air-quality problem [61]. However, the partitioning of nitric acid and ammonia vapours with particulate ammonium nitrate is thought to rapidly reach an equilibrium, often favouring the gas phase when it is warm.

Because ammonium nitrate is semivolatile, nitric acid has not been thought to play an important role in new-particle formation and growth, where very low vapour pressures are required for constituents to be important. Such constituents would include sulfuric acid [62] but also very low vapour pressure organics [63], [64] and iodine oxides [65]. However, it is saturation ratio

and not vapour pressure per se that determines the thermodynamic driving force for condensation, and nitric acid can be three or four orders of magnitude more abundant than sulfuric acid in urban environments. Thus, even a small fractional supersaturation of nitric acid and ammonia vapours with respect to ammonium nitrate has the potential to drive very rapid particle growth, carrying very small, freshly nucleated particles through the valley of death in a few minutes. These rapid growth events can exceed 100 nm h^{-1} under urban conditions—an order of magnitude higher than previous observations—and the growth will continue until the vapours are exhausted and conditions return to equilibrium. Such transients will be difficult to identify in inhomogeneous urban environments, yet have the potential to explain the puzzling observations of new-particle formation in highly polluted megacities.

2.5   Nucleation measurements in CLOUD at CERN

Here we report experiments performed with mixtures of nitric acid, sulfuric acid and ammonia vapours under atmospheric conditions in the CERN CLOUD chamber (Cosmics Leaving OUtdoor Droplets; [66] see Methods for experimental details) from 21 September to 7 December 2018 (CLOUD 13). We varied the temperature from +20 °C to −10 °C, in one case cooling progressively from −15 °C to −25 °C. We adjusted levels of sulfuric acid (H_2SO_4), ammonia (NH_3) and nitric acid (HNO_3), as well as aromatic precursors, to span the ranges typical of polluted megacities. In Figure 2.1 we show two representative events at −10 °C. For Figure 2.1a) we oxidized SO_2 with OH to form H_2SO_4 in the presence of 1,915 parts per trillion volume (pptv) ammonia. The resulting 'banana' is typical of such experiments and of ambient observations under relatively clean conditions, with a single nucleation mode that appears shortly after the onset of nucleation and grows at roughly 20 nm h^{-1}. In Figure 2.1b) we repeated this experiment but also with 5.8 parts per billion volume (ppbv) NO_2, which was oxidized by OH to produce 24 pptv of HNO_3 vapour. The resulting size distribution initially resembles the first case, but when the particles reach about 5 nm, their growth rate accelerates to roughly 45 nm h^{-1}. This activation is reminiscent of cloud-droplet activation and thus suggestive of 'nano-Köhler' behaviour and the Kelvin curvature effect [67].

We repeated these experiments over a range of conditions, either forming HNO_3 from NO_2 oxidation or injecting it directly into the CLOUD chamber from an ultrapure evaporation source. We observed this activation and rapid growth behaviour consistently. In Figure 2.1c) we show the resulting rapid growth rates after activation at -10 °C (green) and $+5$ °C (purple), plotted against the product of the measured gas-phase HNO_3 and NH_3 mixing ratios. Growth rates are based on the 50% appearance time—the time at which particle number concentrations in each size bin of the rapid growth regime reach 50% of their maximum. Both a strong correlation and a clear temperature dependence are evident; when it is colder, the particles grow at the same rate for a much lower product of vapour concentrations. This is consistent with semivolatile uptake of both species, rate limited by the formation of ammonium nitrate.

To confirm this, we measured the composition of the particles using a filter inlet for gases and aerosols (FIGAERO) iodide (I^-) chemical ionization mass spectrometer (CIMS), along with the gas-phase vapour concentrations via several CIMS methods. In Figure 2.2 we show another rapid growth event, this one at $+5$ °C (indicated in Figure 2.1c) with a black outlined purple square). We started with an almost perfectly clean chamber and only vapours present (SO_2, HNO_3 and NH_3) at constant levels (Figure 2.2a). Here we injected the HNO_3 without photochemical production so we could independently control HNO_3 and sulfuric acid. The FIGAERO showed no measurable signal in the absence of particles, indicating negligible crosstalk from vapours. We then turned on ultraviolet lights in order to form OH radicals and to initiate SO_2 oxidation to H_2SO_4. Figure 2.2b) shows the resulting number distribution; as in Figure 2.1b), particles appear, grow slowly, and then activate and grow at 700 nm h^{-1}. We again show the 50% appearance time of both modes. In Figure 2.2c) we show the associated volume distribution. Within 15 min of the onset of particle formation, the volume is dominated by the upper mode near 200 nm. Finally, in Figure 2.2d) we show a FIGAERO thermogram (signal versus desorption temperature) for particles collected between 10 min and 40 min after the onset of photochemistry. Their composition is dominated by nitrate, with a much smaller but notable sulfate contribution; the semivolatile nitrate desorbs at a much lower temperature than the sulfate. The I^- chemical

ionization is not sensitive to NH_3, but both nitrate and sulfate exist presumably as ammonium salts in the particles.
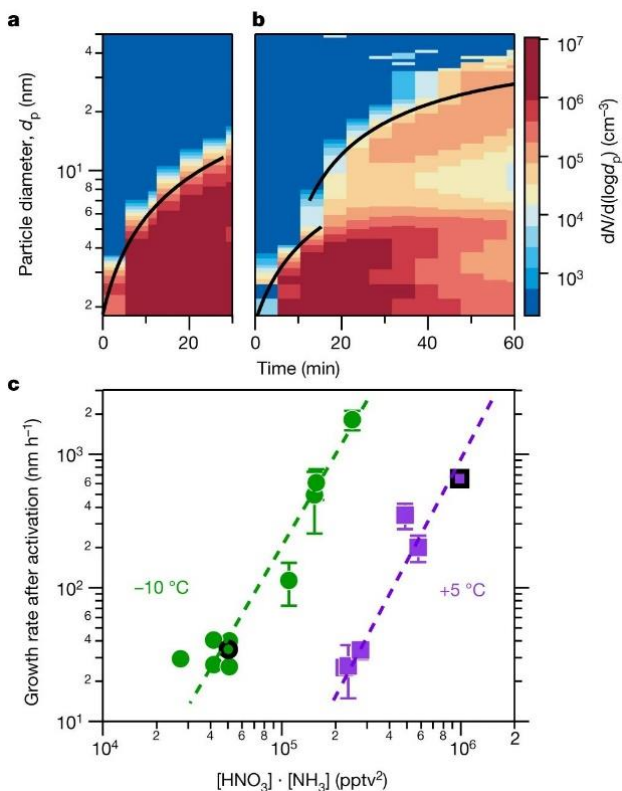

Figure 2.1: Rapid growth events observed in the CERN CLOUD chamber. a) Particle nucleation and growth (particle growth rate, dd_p/dt) at −10 °C from a mixture of 0.44 pptv sulfuric acid and 1,915 pptv ammonia at 60% relative humidity. Particles form and grow to roughly 10 nm in 30 min. The black curve shows the linear fit to the 50% appearance times. **b)** Particle formation and growth under identical conditions to those in a, but with the addition of 24 pptv of nitric acid vapour formed via NO_2 oxidation. Once particles reach roughly 5 nm, they experience rapid growth to much larger sizes, reaching more than 30 nm in 45 min. **c)** Observed growth rates after activation versus the product of measured nitric acid and ammonia levels at +5 °C and −10 °C. The point corresponding to the rapid growth regime for $d_p > 6$ nm in b is a black-outlined green circle, and the point corresponding to Figure 2.2 is a black-outlined purple square. Growth rates at a given vapour product are substantially faster at −10 °C than at +5 °C, consistent with semivolatile condensation that is rate limited by ammonium nitrate formation. Error bars are 95% confidence limits on the fitting coefficients used to determine growth rates. The overall systematic scale uncertainties of ±10% on the NH_3 mixing ratio and ±25% on the HNO_3 mixing ratio are not shown.
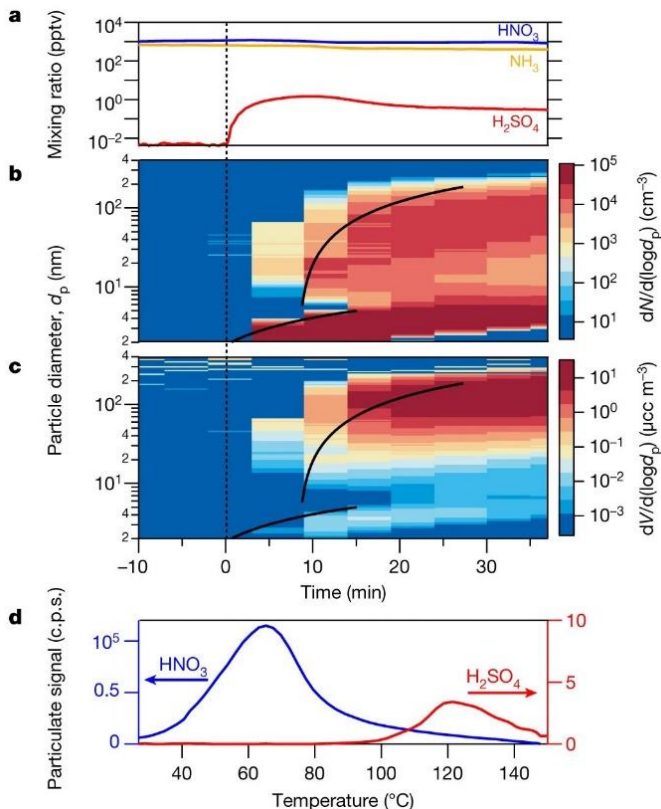
Figure 2.2: Chemical composition during a rapid growth event at +5 °C and 60% relative humidity. This growth event is indicated in Figure 2.1c) with a black-outlined purple square. **a)** Gas-phase nitric acid (NO_3), ammonia (NH_3) and sulfuric acid (H_2SO_4) mixing ratios versus time in an event initiated by SO_2 oxidation, with constant nitric acid and ammonia. **b)** Particle diameters and number distributions versus time, showing a clean chamber (to the left of the vertical dotted line), then nucleation after sulfuric acid formation and rapid growth once particles reach 2.3 nm. Black curves are linear fits to the 50% appearance times. **c)** Particle volume distributions from the same data, showing that 200 nm particles dominate the mass after 15 min. 1 µcc = 1 cm^{-6}. **d)** FIGAERO thermogram from a 30 min filter sample after rapid growth (c.p.s., counts per second). The particle composition is dominated by nitrate with a core of sulfate, consistent with rapid growth by ammonium nitrate condensation on an ammonium sulfate (or bisulfate) core (note the different *y*-axis scales; the instrument is not sensitive to ammonia). A thermogram from just before the formation event shows no signal from either nitrate or sulfate, indicating that vapour adsorption did not interfere with the analysis.

In addition to the correlation of activated particle growth rates with the product of HNO_3 and NH_3 at a given temperature, the observed activation diameter (d_{act}) shows a strong dependence on this product. The activation diameter is evident as a clear kink in the 50% appearance curve, as well as a notable absence of particles in the slower-growth mode above d_{act}. In Figure 2.2a) in the Supplementary Information (SI) we show an example of how we determine d_{act}, using the emergence of a bimodal size distribution as the defining feature. In Figure 2.3a) we plot the observed activation diameter at each temperature in a phase space, with [HNO_3] on the log$x$ axis and [NH_3] on the log$y$ axis (both in pptv). The number within each symbol is the observed activation diameter for that experiment. We show the saturation ratio (S) of ammonium nitrate at each temperature via a series of diagonal lines in this log–log space (slope = −1); specifically, we show S = 1, 5 and 25, emphasizing S = 1 as a thick solid line. We also indicate 1:1 [HNO_3]:[NH_3] with a dashed grey line (slope +1); points to the upper left (most of the values) are 'nitric acid limited', with more ammonia than nitric acid. All of these concentrations are well within the ranges typically observed in wintertime megacity conditions [68].

For both +5 °C and −10 °C, we consistently observe a relationship between S and d_{act} (we never achieved saturation at +20 °C and did not observe rapid growth). We observe no activation for S values of less than 1, and activation for S values greater than 1, with logd_{act} being inversely proportional to log([HNO_3]·[NH_3]) at each temperature (Figure 2.6b, SI). Notably, d_{act} can be well under 10 nm and as low as 1.6 nm. This suggests that nitric acid and ammonia (ammonium nitrate) condensation may play a role in new-particle formation and growth within the valley of death, where very small particles are most vulnerable to loss by coagulation [53].

We also performed experiments with only nitric acid, ammonia and water vapour added to the chamber (sulfuric acid contamination was measured to be less than 2×10^{-3} pptv). For temperatures of less than −15 °C and S values of more than 10^3, we observed nucleation and growth of pure ammonium nitrate particles (Figure 2.3c). We progressively cooled the chamber to −24 °C, while holding the vapours at a constant level (Figure 2.3b). The particle-formation rate ($J_{1.7}$) rose steadily from 0.006 cm^{-3} s^{-1} to 0.06 cm^{-3} s^{-1} at −24 °C. In Figure 2.7 (SI) we show a pure ammonium nitrate nucleation experiment performed at −25 °C under vapour conditions

reported for the tropical upper troposphere [50] (30–50 pptv nitric acid and 1.8 ppbv ammonia), showing that this mechanism can produce several 100 cm^{-3} particles per hour.

Our experiments show that semivolatile ammonium nitrate can condense on tiny nanoparticles, consistent with nano-Köhler theory [67]. To confirm this we conducted a series of simulations using the monodisperse thermodynamic model MABNAG (model for acid-base chemistry in nanoparticle growth) [69], which treats known thermodynamics, including curvature (Kelvin) effects for a single evolving particle size. We show the points of the MABNAG simulations as triangles in Figure 2.3a). MABNAG consistently and quantitatively confirms our experimental findings: there is little ammonium nitrate formation at S values of less than 1.0, as expected; and activation behaviour with ammonium nitrate condensation ultimately dominating the particle composition occurs at progressively smaller d_{act} values as S rises well above 1.0. The calculated and observed d_{act} values are broadly consistent. In Figure 2.4 we show two representative MABNAG growth simulations for the two points indicated with open and filled diamonds in Figure 2.3a); the simulations show no ammonium nitrate formation when conditions are undersaturated, but substantial formation when conditions are saturated, with activation behaviour near the observed d_{act} = 4.7 nm. We show the calculated composition as well as diameter versus time for these and other cases in Figure 2.8 (SI).
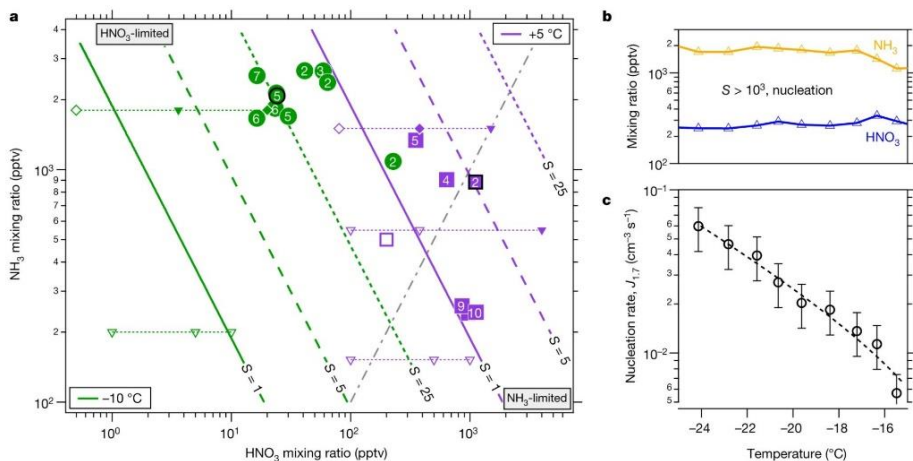
Figure 2.3: Phase space for rapid growth and nucleation. a) Ammonium nitrate saturation ratios versus gas-phase nitric acid and ammonia mixing ratios at 60% relative humidity. The coloured lines (slope = −1) represent $S = 1$ (bold), $S = 5$ (dashed) and $S = 25$ (dotted), at −10 °C (green) and +5 °C (purple). The slope = +1 dot-dashed grey line indicates a 1:1 ammonia:nitric-acid stoichiometry; the phase space to the upper left of this line is nitric-acid limited. Observed activation diameters (in nm) for measured nitric-acid–ammonia pairs are plotted as numbers inside solid circles and squares; open symbols show no activation. Activation occurs only for S values of more than 1, and the activation diameter decreases as S increases. Points from MABNAG simulations are shown with open triangles for no activation and filled triangles for activation; simulations indicated with diamonds are shown in detail in Figure 2.4 and Figure 2.8 (SI). Points from runs shown in Figure 2.1 and Figure 2.2 are emphasized with a thick black outline. **b)** Mixing ratios for ammonia and nitric acid vapour during a pure ammonium nitrate nucleation scan from −16 °C to −24 °C. **c)** Particle-formation (nucleation) rates ($J_{1.7}$) during the nucleation scan, showing a strong inverse relationship with temperature at constant HNO_3 and NH_3, with H_2SO_4 concentrations of less than 0.002 pptv and relative humidity starting at 60% and ending at 40%. The bars indicate 30% estimated total errors on the nucleation rates, although the overall systematic scale uncertainties of ±10% on the NH_3 mixing ratio and ±25% on the HNO_3 mixing ratio are not shown.
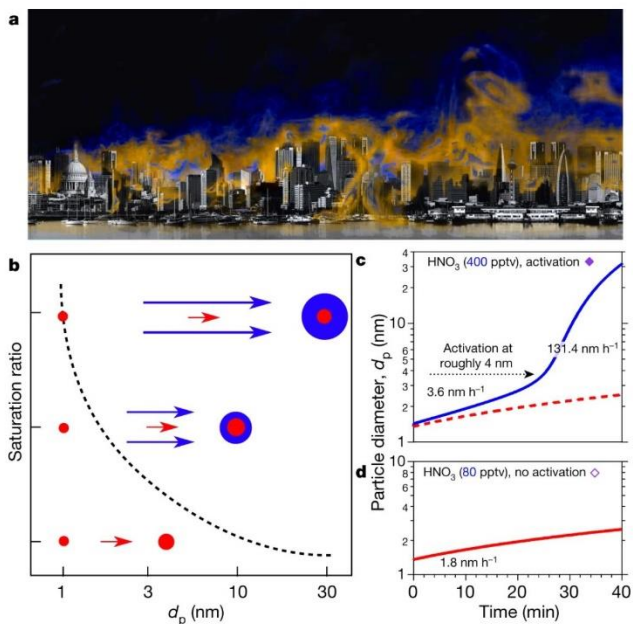
Figure 2.4: Conditions for rapid growth. Persistent supersaturations of ammonia and nitric acid with respect to ammonium nitrate will be sustained by inhomogeneity in urban conditions with high source strength. This will be sufficient to accelerate particle growth in the range 1–10 nm, where survival is threatened by the high coagulation sink of pre-existing particles from pollution. **a)** Conceptual image of urban conditions, where inhomogeneities in the concentrations of ammonia and nitric acid vapour and in temperatures are caused by non-uniform sources and large-scale eddies. **b)** Particles nucleate and grow slowly as (base-stabilized) sulfate (red). The activation size (shown with d_p on the *x*-axis) correlates inversely with the ammonium nitrate saturation ratio (shown qualitatively on the *y*-axis), as indicated by the dashed curve. Available concentrations of gas-phase nitric acid can exceed those of sulfuric acid by a factor of 1,000, so modest supersaturation drives rapid growth (blue) above an activation diameter determined by particle curvature (the Kelvin term). **c-d)** Monodisperse thermodynamic growth calculations (from MABNAG simulations) for high (**c**) and low (**d**) saturation ratios of ammonium nitrate, corresponding to **b** and to the closed and open diamonds towards the upper right in Figure 2.3a). For a saturation ratio near 4, activation is predicted to occur near 4 nm, consistent with our observations.

We also conducted nano-Köhler simulations [67], shown in Figure 2.6c) (SI), which confirm the activation of ammonium nitrate condensation at diameters less than 4 nm, depending on the size of an assumed ammonium sulfate core. For a given core size the critical supersaturation required for activation at −10 °C is a factor of two to three higher than at +5 °C, consistent with the observed behaviour shown in Figure 2.3a). While particles of 1–2 nm contain only a handful

of acid and base molecules, the MABNAG and nano-Köhler simulations based on bulk thermodynamics—with only a Kelvin term to represent the unique behaviour of the nanoparticles—capture the activation and growth behaviours we observe.

2.6 Atmospheric implications

Our findings suggest that the condensation of nitric acid and ammonia onto nanoparticles to form ammonium nitrate (or, by extension, aminium nitrates in the presence of amines) may be important in the atmosphere. This process may contribute to urban new-particle formation during wintertime via rapid growth. It may also play a role in free-tropospheric particle formation, where sufficient vapours may exist to allow nucleation and growth of pure ammonium nitrate particles. We observe these behaviours in CLOUD for vapour concentrations well within those typical of the atmosphere.

Rapid growth may contribute to the often puzzling survival of newly formed particles in megacities, where particles form at rates consistent with sulfuric-acid–base nucleation and appear to grow at typical rates (roughly 10 nm h^{-1}) in the presence of extremely high condensation sinks that seemingly should scavenge all of the tiny nucleated particles. As shown in Figure 2.5 in the SI, the ratio of $10^4 \times$ condensation sink (CS; in units of s^{-1}) to growth rate (GR; in nm h^{-1}) during nucleation events in Asian megacities typically ranges between 20 and 50, where the survival probability of particles with sizes of between 1.5 nm and 3 nm should drop precipitously [23]. However, the observed growth rates are based on appearance times in measured ambient size distributions—just as in Figure 2.1 and Figure 2.2—and thus reflect a spatial and temporal average of air masses passing over a sampling site during the course of a day. Rapid growth rates can reduce CS:GR by a factor of ten or more, effectively displacing urban ratios into a range characteristic of remote regions (Figure 2.5b, SI). The empirically derived nucleation rates in Figure 2.5b, SI) correlate positively with high CS:GR, consistent with high production rates of condensable vapours; however, the complicated microphysics of particles smaller than 10 nm make a simple determination of the growth rate difficult. Urban conditions are however far less homogeneous than those of CLOUD, or even of remote boreal forests such

as Hyytiälä. Because survival probability depends exponentially on CS:GR (refs. [23], [52]), but spatial (and temporal) averaging as well as ambient mixing are linear, real urban conditions may contain pockets conducive to transient rapid growth and thus unusually high survival probability that are blurred in the (averaged) observations.

The key here is that nitric acid vapour and ammonia are often at least one thousand times more abundant than sulfuric acid vapour. Thus, although they tend towards equilibrium with ammonium nitrate in the particle phase, even a modest perturbation above saturation can unleash a tremendous thermodynamic driving force for condensational growth, nominally up to one thousand times faster than growth by sulfuric acid condensation. This may be brief, but because of the disparity in concentrations, even a small deviation in saturation ratio above 1.0 may drive rapid growth for a short period at several nanometers per minute, as opposed to several nanometers per hour. The particles will not experience rapid growth for long, but they may grow fast enough to escape the valley of death.

We illustrate rapid growth in Figure 2.4. Under most urban conditions, nucleation and early growth up to the activation size are likely to be controlled by sulfuric acid and a base (ammonia or an amine), shown by the red 'cores' in Figure 2.4b). During the day (even in wintertime)—when NO_2 is oxidized by OH in the gas phase to produce nitric acid at rates of up to 3 ppbv h^{-1}, and ammonia from traffic, other combustion emissions and agriculture can reach 8 ppbv (ref. [68])—nitric acid and ammonia will not equilibrate, but rather will approach a modest steady-state supersaturation that drives ammonium nitrate formation to balance the production and emissions. However, this steady state will only be reached after several e-folding time periods set by the particle condensation sink. Typically, new-particle formation occurs at the lower end of the condensation-sink distribution (even under urban conditions) [16], [52], so this timescale will be several minutes, or a length scale of hundreds of meters in the horizontal and tens of meters in the vertical. There are ample sources of inhomogeneity on this timescale, including inhomogeneous sources such as traffic on major roadways and vertical mixing (with an adiabatic lapse rate of −9 °C km^{-1}) [68]. Further, large eddy simulations of a megacity (Hong Kong) confirm widespread eddies with spatial scales of tens to hundreds of meters and velocity perturbations

of the order 1 m s^{-1} (ref. [70]). This is consistent with the sustained inhomogeneity required for the rapid growth we demonstrate here, shown conceptually in Figure 2.4a). It is thus likely that dense urban conditions will typically include persistent inhomogeneities that maintain supersaturation of nitric acid and ammonia with sufficient magnitude to drive rapid growth, as indicated by the blue 'shell' in Figure 2.4b). Our thermodynamic models support the phenomenology of Figure 2.4b), as shown in Figure 2.4c, d, although the composition is likely to be an amorphous mixture of salts (Figure 2.8, SI). Rapid growth may be sufficient for particles to grow from vulnerable sizes near 2.5 nm to more robust sizes larger than 10 nm. For example, repeated nucleation bursts with very rapid growth were observed in the ammonia- and nitric-acid-rich Cabauw site in the Netherlands during the EUCAARI campaign [71].

It is common for chemical transport models to use an equilibrium assumption for ammonium nitrate partitioning, because—on the timescale of the coarse spatial grids and long time steps characteristic of large-scale models—the ammonium nitrate aerosol system should equilibrate with respect to the bulk submicrometer-size particles. Further, because rapid growth appears to be rate limited by the formation of ammonium nitrate, the covariance of base and nitric acid sources and concentrations may be essential. Even typical megacity steady-state vapour concentrations fall somewhat above the green points in Figure 2.3a) (towards larger mixing ratios). For constant production rates, as the temperature falls the ammonium nitrate saturation lines shown in Figure 2.3a) will sweep from the upper right towards the lower left, moving the system from rough equilibrium for typical urban production and emission rates when it is warmer than about +5 °C, to a sustained supersaturation when it is colder. Just as equilibrium organic condensation and partitioning results in underestimated growth rates from organics in the boreal forest [72], equilibrium treatments of ammonium nitrate condensation will underestimate the role of nitric acid in nanoparticle growth, especially for inhomogeneous urban environments.

Although the pure ammonium nitrate nucleation rates in Figure 2.3c) are too slow to compete in urban new-particle formation, this mechanism may provide an important source of new particles in the relatively clean and cold upper free troposphere, where ammonia can be

convected from the continental boundary layer [73] and abundant nitric acid is produced by electrical storms [50]. Theoretical studies have also suggested that nitric acid may serve as a chaperone to facilitate sulfuric-acid–ammonia nucleation [74]. Larger (60–1,000 nm) particles consisting largely of ammonium nitrate, along with more than 1 ppbv of ammonia, have been observed by satellite in the upper troposphere during the Asian monsoon anticyclone [50], and abundant 3–7-nm particles have been observed in situ in the tropical convective region at low temperature and condensation sink [51]. Although these particles are probably formed via nucleation, the mechanism is not yet known. However, our experiment under similar conditions (Figure 2.7, SI) shows that it is plausible that pure ammonium nitrate nucleation and/or rapid growth by ammonium nitrate condensation contributes to these particles in the upper troposphere.

Our results indicate that the condensation of nitric acid and ammonia is likely to be an important new mechanism for particle formation and growth in the cold upper free troposphere, as supported by recent observations [50], [51]. Furthermore, this process could help to explain how newly formed particles survive scavenging losses in highly polluted urban environments [23]. As worldwide pollution controls continue to reduce SO_2 emissions sharply, the importance of NO_X and nitric acid for new-particle formation is likely to increase. In turn, controls on NO_X and ammonia emissions may become increasingly important, especially for the reduction of urban smog.

2.7 Online content

Any methods, additional references, Nature Research reporting summaries, source data, extended data, supplementary information, acknowledgements, peer review information; details of author contributions and competing interests; and statements of data and code availability are available at https://doi.org/10.1038/s41586-020-2270-4.

2.8 Acknowledgements

2.9 Author contributions

M.W., R.M., J. Dommen, U.B., J. Kirkby, I.E-H. and N.M.D. planned the experiments. M.W., W.K., R.M., X-C.H., D.C., J.P., A.K., H.E.M., S.A., A.B., S. Bräkling, S. Brilke, L.C.M., B.C., L-P.D.M., J. Duplissy, H.F., L.G.C., M.G., R.G., A. Hansel, V.H., J.K., K.L., H.L., C.P.L., V.M., G.M., S.M., B.M., T.M., A.O., E.P., T.P., M.P., V.P., M.R., B.R., W.S., J.S., M. Simon, M. Sipilä, G.S., D.S., Y.J.T., A.T.,

2.10 Competing interests

2.11 Supplementary Information

2.11.1 Methods

2.11.1.1 The CLOUD Facility

We conducted our measurements at the CERN CLOUD facility, a 26.1 m^3 electropolished stainless-steel chamber that enables new-particle-formation experiments under the full range of tropospheric conditions with scrupulous cleanliness and minimal contamination [66], [75]. The CLOUD chamber is mounted in a thermal housing, capable of keeping temperature constant in a range between −65 °C and +100 °C with ±0.1 °C precision [76], and relative humidity between 0.5% and 101%. Photochemical processes are initiated by homogeneous illumination with a built-in ultraviolet fibre-optic system, including four 200-W Hamamatsu Hg–Xe lamps at wavelengths between 250 nm and 450 nm and a 4-W KrF excimer ultraviolet laser at 248 nm with adjustable power. Ion-induced nucleation under different ionization levels is simulated with a combination of electric fields (±30 kV) and a high-flux beam of 3.6-GeV pions (π+), which can artificially scavenge or enhance small ions. Uniform spatial mixing is achieved with magnetically coupled stainless-steel fans mounted at the top and bottom of the chamber. The characteristic gas mixing time in the chamber during experiments is a few minutes. The loss rate of condensable vapours and particles onto the chamber walls is comparable to the ambient condensation sink. To avoid contamination, the chamber is periodically cleaned by rinsing the walls with ultrapure water and heating to 100 °C for at least 24 h, ensuring extremely low contaminant levels of sulfuric acid (less than 5×10^4 cm^{-3}) and total organics (less than 50 pptv) [63], [77] The CLOUD gas system is also built to the highest technical standards of cleanliness and performance. The dry air supply for the chamber is provided by boil-off oxygen (Messer, 99.999%) and boil-off nitrogen (Messer, 99.999%) mixed at the atmospheric ratio of 79:21. Highly pure water vapour, ozone and other trace gases can be precisely added at the pptv level.

2.11.1.2   Typical experimental sequence

To investigate the role of nitric acid in new-particle formation, we performed particle growth experiments at T = −10 °C, +5 °C and +20 °C, and (for the most part) at relative humidities of approximately 60%. A typical experiment started with illumination of the chamber at constant ozone (O_3) to photochemically produce •OH radicals. The subsequent oxidation of premixed SO_2, NO_2 and anthropogenic volatile organic compounds (VOCs; that is, toluene or cresol) led to the production of H_2SO_4, HNO_3 and highly oxygenated organic molecules (HOMs), respectively. As a result, nucleation was induced, followed (once the particles reached an activation diameter, d_{act}) by rapid growth via condensation of nitric acid and ammonia. In some experiments, we also injected nitric acid vapour directly into the CLOUD chamber from an ultrapure source to cover a wide range of conditions. In addition, to prove consistency we also carried out experiments with a biogenic precursor, α-pinene, replacing anthropogenic VOCs, as well as experiments without any organic vapours. For the experiments we focus on here, the HOM concentrations were either zero or small enough to have a minor effect on the experiment. In one case, we cooled the particle-free chamber (with fewer than 1 particle per cm^{-3}) continuously from −10 °C to −25 °C, while holding nitric acid and ammonia at a constant level, but with no sulfuric acid (less than 5×10^4 cm^{-3} or 2×10^{-3} pptv). We observed new-particle formation purely from nitric acid and ammonia at temperatures of −15 °C and lower. The nucleation rate grew as the temperature dropped. Moreover, as shown in Figure 2.7, at −25 °C new-particle formation events appeared to be quenched when we swept out primary ions with the electric field, and did not return until the field was turned off to allow primary ion production by galactic cosmic rays to again accumulate (roughly 700 cm^{-3}). We list the chamber conditions and key parameters for all the experiments here in Table 2.1.

2.11.1.3   Instrumentation

To measure gas-phase nitric acid, we deployed a bromide chemical ionization atmospheric pressure interface time-of-flight (CI-APi-TOF) mass spectrometer [78], [79] equipped with a commercial inlet (Airmodus) to minimize wall contact of the sample [80]. We flowed

dibromomethane (CH_2Br_2) into the ion-molecule reaction inlet to produce the primary reagent ion Br^-. During its collision with HNO_3, Br^- reacts either to form a cluster or via a proton transfer from the HNO_3 to form NO_3^-:

$$Br^- + HNO_3 \rightarrow HNO_3 \cdot Br^- \tag{2.1}$$

$$Br^- + HNO_3 \rightarrow HBr \cdot NO_3^- \tag{2.2}$$
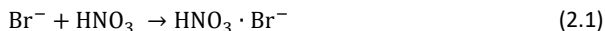
To take the variation in the total reagent ions into account, we quantified nitric acid concentrations according to:

$$[HNO_3] = \frac{[NO_3^-]}{[Br^-] + [H_2O \cdot Br^-]} \times C \tag{2.3}$$

where C (in units of pptv) is a calibration coefficient obtained by measuring HNO_3/N_2 mixtures with known nitric acid concentrations. The nitric acid source was a portable permeation tube, kept constantly at 40 °C. An N_2 flow of 2 litres per minute was introduced into the permeation device to carry out the nitric acid vapour. To determine the permeation rate of nitric acid, we passed the outflow of the permeation tube through an impinger containing deionized water, and analysed the resulting nitric acid solution by spectrophotometry. Line losses during experiments and calibration procedures were calculated separately. We determined the corrected calibration coefficient to be 7,364 pptv.

Gas-phase ammonia was measured by a water cluster CI-APi-TOF mass spectrometer (described elsewhere, [45]). The crossflow ion source coupled to a TOF mass spectrometer enables the selective measurement of basic compounds (for example, ammonia) by using positively charged water clusters as primary ions. Owing to the low reaction times (less than 1 ms), the instrument responds rapidly to changing chamber conditions with a detection limit of ammonia of 0.5 pptv.

Gas-phase sulfuric acid and HOMs were routinely measured with a detection limit of approximately 5×10^4 cm^{-3} by two nitrate CI-APi-TOF mass spectrometers. One instrument was equipped with the Airmodus inlet and an X-ray generator as the ion source; the other deployed

a home-made inlet and a corona discharge for ion generation [44]. An electrostatic filter was installed in front of each instrument to remove ions and charged clusters formed in the chamber. Sulfuric acid and HOMs were quantified following calibration and loss correction procedures described previously [63], [66], [81].

VOCs were monitored by a proton transfer reaction time-of-flight mass spectrometer (PTR-TOF-MS; Ionicon Analytik); this also provides information about the overall cleanliness regarding VOCs in the chamber. The technique has been extensively described previously [43]. Direct calibration using diffusion sources allows us to determine VOC mixing ratios with an accuracy of 5% and a typical detection limit of 25 pptv (ref. [82]).

Gas monitors were used to measure ozone (O3; Thermo Environmental Instruments TEI 49C), sulfur dioxide (SO$_2$; Thermo Fisher Scientific 42i-TLE) and nitric oxide (NO; ECO Physics, CLD 780TR). Nitrogen dioxide (NO$_2$) was measured using a cavity-attenuated phase-shift NO2 monitor (CAPS NO2, Aerodyne Research) and a homemade cavity-enhanced differential optical absorption spectroscopy (CE-DOAS) instrument. The relative humidity of the chamber was determined using dew point mirrors (EdgeTech).

We measured the particle-phase composition via thermal desorption using an iodide-adduct chemical ionization time-of-flight mass spectrometer equipped with a filter inlet for gases and aerosols (FIGAERO-CIMS) [83], [84]. FIGAERO is a manifold inlet for a CIMS with two operating modes. In one mode, gases are directly sampled into a 100-mbar turbulent flow ion-molecule reactor while particles are concurrently collected on a polytetrafluoroethylene (PTFE) filter via a separate dedicated port. In the other mode, the filter is automatically moved into a pure N$_2$ gas stream flowing into the ion-molecule reactor while the N$_2$ is progressively heated to evaporate the particles via temperature-programmed desorption. Analytes are then chemically ionized and extracted into a TOF-MS, achieving a detection limit below 10^6 cm^{-3}.

Particle-size distributions between 1.8 nm and 500 nm were monitored continuously by a differential mobility analyser train (DMA-Train), a nano-scanning electrical mobility spectrometer (nSEMS), a nano-scanning mobility particle sizer (nano-SMPS), and a long-SMPS.

The DMA-Train was constructed with six identical DMAs operating at different, but fixed, voltages. Particles transmitted through the DMAs were then detected by either a particle-size magnifier (PSM) or a CPC, depending on the size ranges. An approximation of the size distribution with 15 size bins was acquired by logarithmic interpolation between the six channels [47]. The nSEMS used a new, radial opposed migration ion and aerosol classifier (ROMIAC), which is less sensitive to diffusional resolution degradation than the DMAs [85], and a soft X-ray charge conditioner. After leaving the classifier, particles were first activated in a fast-mixing diethylene glycol stage [86], and then counted with a butanol-CPC. The nSEMS transfer function that was used to invert the data to obtain the particle-size distribution was derived using three-dimensional finite-element modelling of the flows, electric field and particle trajectories [87], [88]. The two commercial mobility particle-size spectrometers, nano-SMPS and long-SMPS, have been fully characterized, calibrated and validated in several previous studies [89]–[91].

2.11.1.4   Determination of growth rate

The combined particle-size distribution was reconstructed using measurement data from DMA-Train at 1.8–4.3 nm, nSEMS at 4.3–18.1 nm, nano-SMPS at 18.1–55.2 nm and long-SMPS at 55.2–500 nm, and synchronized with long-SMPS measurement time. We list the sizing and resolution information of these instruments in Table 2.2. As depicted in Figure 2.9a, the four instruments showed excellent agreement in their overlapping regions of the size ranges. The total number concentration obtained by integrating the combined size distribution agreed well with measurement by an Airmodus A11 nano-condensation nucleus counter (nCNC) and a TSI 3776 ultrafine condensation particle counter (UCPC) (Figure 2.9b). Particle growth rate, dd_p/dt, was then determined from the combined size distributions using the 50% appearance time method [64], as a clear front of a growing particle population could be identified during most rapid growth events (Figure 2.10). For the rapid growth rates, which are the principal focus here, the SMPS measurements provided the major constraint.

2.11.1.5   Determination of activation diameter

The activation diameter (d_{act}) was interpreted as the size at which growth accelerated from the slow, initial rate to the rapid, post-activation rate. The activation diameter was determined using the particle-size distribution acquired from DMA-Train or nSEMS at small sizes (less than 15 nm). At the activation diameter, the growth rate calculated from the 50% appearance time usually experienced a sharp change, from below 10 nm h^{-1} to (often) over 100 nm h^{-1}, depending on concentrations of supersaturated HNO$_3$ and NH$_3$ vapours. A fast growth rate leads to a relatively low steady-state concentration of particles just above the activation diameter; the activation event often resulted in a notable gap in the particle-number size distribution. In some cases, a clear bimodal distribution was observed, with the number concentration in one size bin plunging below 10 counts cm^{-3}, while the counts at larger sizes rose to more than 100 counts cm^{-3}; the centroid diameter of the size bin at which the number concentration dropped was then defined as the activation diameter (Figure 2.6a).

2.11.1.6   Calculation of saturation ratio

We model the ammonium nitrate formed in the particle phase as solid in our particle growth experiments, given that the relative humidity (roughly 60%) was less than the deliquescence relative humidity (DRH), given by [1]:

$$\ln(\mathrm{DRH}) = \frac{723.7}{T} + 1.6954 \tag{2.4}$$

The dissociation constant, K_p, is defined as the product of the equilibrium partial pressures of HNO$_3$ and NH$_3$. K_p can be estimated by integrating the van't Hoff equation [92]. The resulting equation for K_p in units of ppb^2 (assuming 1 atm of total pressure) [36] is:

$$\ln K_p = 118.87 - \frac{24{,}084}{T} - 6.025 \ln T \tag{2.5}$$

The saturation ratio, S, is thus calculated by dividing the product of measured mixing ratios of HNO_3 and NH_3 by the dissociation constant. The dissociation constant is quite sensitive to temperature changes, varying over more than two orders of magnitude for typical ambient conditions. Several degrees of temperature drop can lead to a much higher saturation ratio, shifting the equilibrium of the system towards the particle phase drastically. As illustrated in Figure 2.11, with an adiabatic lapse rate of $-9\,°C\,km^{-1}$ during fast vertical mixing, upward transport of a few hundred meters alone is sufficient for a saturated nitric acid and ammonia air parcel to reach the saturation ratio capable of triggering rapid growth at a few nanometers.

2.11.1.7   Determination of nucleation rate

The nucleation rate, $J_{1.7}$, is determined here at a mobility diameter of 1.7 nm (a physical diameter of 1.4 nm) using particle size magnifier (PSM). At 1.7 nm, a particle is normally considered to be above its critical size and, therefore, thermodynamically stable. $J_{1.7}$ is calculated using the flux of the total concentration of particles growing past a specific diameter (here at 1.7 nm), as well as correction terms accounting for aerosol losses due to dilution in the chamber, wall losses and coagulation. Details can be found in our previous work [93].

2.11.1.8   The MABNAG model

To compare our measurements to thermodynamic predictions (including the Kelvin term for curved surfaces), we used the model for acid-base chemistry in nanoparticle growth (MABNAG) [69]. MABNAG is a monodisperse particle population growth model that calculates the time evolution of particle composition and size on the basis of concentrations of condensing gases, relative humidity and ambient temperature, considering also the dissociation and protonation between acids and bases in the particle phase. In the model, water and bases are assumed always to be in equilibrium state between the gas and particle phases. Mass fluxes of acids to and from the particles are determined on the basis of their gas phase concentrations and their equilibrium vapour concentrations. In order to solve for the dissociation- and composition-dependent equilibrium concentrations, MABNAG couples a particle growth model to the

extended aerosol inorganics model (E-AIM) [94], [95]. Here, we assumed particles in MABNAG to be liquid droplets at +5 °C and −10 °C, at 60% relative humidity. The simulation system consisted of four compounds: water, ammonia, sulfuric acid and nitric acid. The initial particle composition in each simulation was 40 sulfuric acid molecules and a corresponding amount of water and ammonia according to gas-particle equilibrium on the basis of their gas concentrations. With this setting, the initial diameter was approximately 2 nm. Particle density and surface tension were set to 1,500 kg m^{-3} and 0.03 N m^{-1}, respectively. In Figure 2.8, we show that MAGNAG computations confirm that nitric acid and ammonia at the measured concentrations can activate small particles and cause rapid growth, and also confirm that the activation diameter depends on the ammonium nitrate saturation ratio, consistent with our measured diameter (diamonds in Figure 2.3a).

2.11.1.9   Nano-Köhler theory

To prove consistency, we also calculated the equilibrium saturation ratios of ammonium nitrate above curved particle surfaces according to nano-Köhler theory [67]. This theory describes the activation of nanometer-sized inorganic clusters to growth by vapour condensation, which is analogous to Köhler theory describing the activation of cloud condensation nuclei (CCN) to cloud droplets. Here, we assumed seed particles of ammonium sulfate, and performed calculations for three seed-particle diameters (d_s = 1.4 nm, 2.0 nm and 2.9 nm) at +5 °C and −10 °C, and at 60% relative humidity. The equilibrium vapour pressures of HNO$_3$ and NH$_3$ over the liquid phase, and the surface tension and density of the liquid phase, were obtained from an E-AIM [94], [95]. The equilibrium saturation ratios of ammonium nitrate were calculated as described in the Methods section 'Calculation of saturation ratio', also including the Kelvin term. The resulting Köhler curves, showing the equilibrium saturation ratio as a function of particle diameter, are presented in Figure 2.6c). The maxima of each curve corresponds to the activation diameter (d_{act}); saturation ratios of 10–50 lead to d_{act} values of 3–5 nm, consistent with our measurements in Figure 2.3a). We summarize detailed results in Table 2.1.

2.11.1.10   Ambient nucleation and growth

In Table 2.3 we compile ambient observations of nucleation rates, growth rates and the ambient condensation sink. In most cases these are derived from evolving particle-size distributions. We summarize these observations in Figure 2.5.

2.11.2 Supplementary Information figures and tables
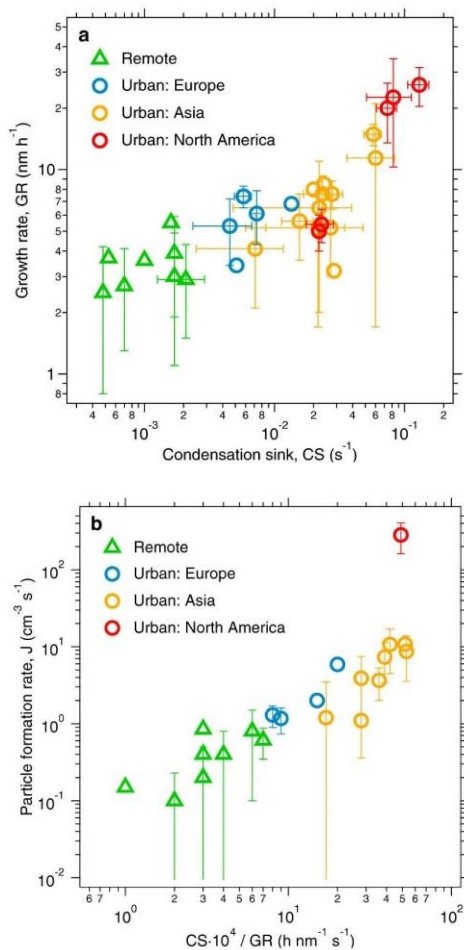
Figure 2.5: New-particle-formation events observed in various remote and urban environments (see Table 2.3 for a complete set of references). a) Growth rates (GR) versus condensation sinks (CS), showing that both are higher in polluted urban environments than in other environments. **b)** Particle-formation rates (*J*) versus a measure of particle loss via coagulation (CS × 10^4/GR, similar to the McMurry L parameter), showing high new-particle-formation rates in urban conditions where the condensation sinks were so high compared to the growth rate that survival of nucleated particles should be very low. *J* and GR were calculated over the size range from a few nanometers to over 20 nm, except for *J* at Shanghai [96] and Tecamac [97], which were calculated from 3 nm to 6 nm. The bars indicate 1σ total errors.
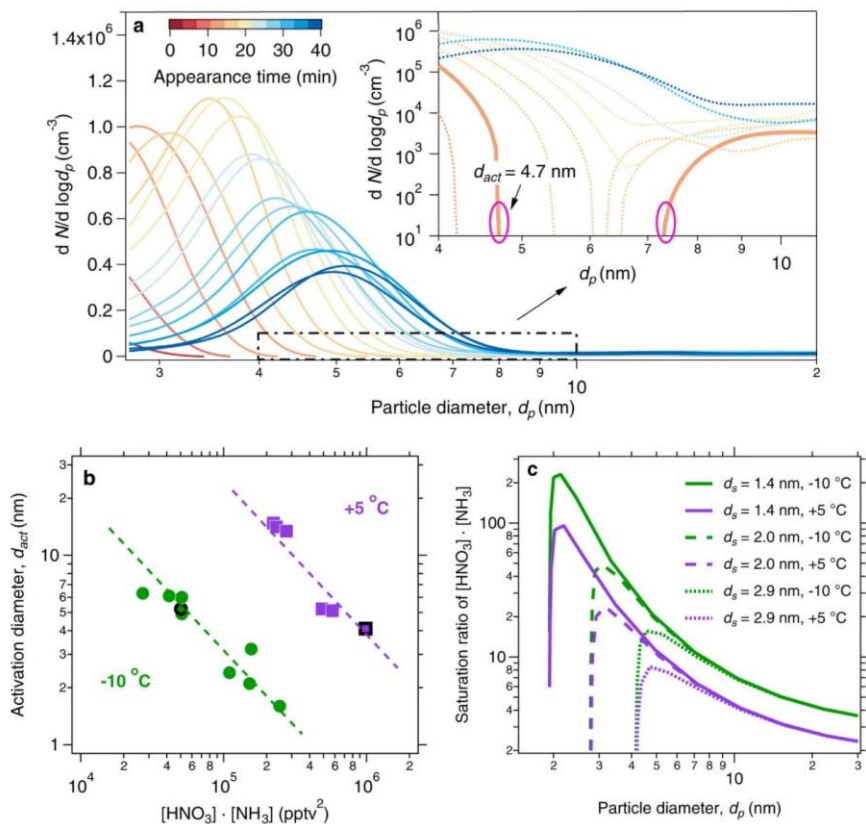
Figure 2.6: Activation diameter of newly formed particles. a) Determination of the activation diameter, d_{act}, from a rapid growth event at +5 °C, in the presence of nitric acid, ammonia and sulfuric acid. The solid orange trace in the insert indicates the first size distribution curve that exhibited a clear bimodal distribution, which appeared roughly 7 min after nucleation. We define the activation diameter as the largest observed size of the smaller mode. In this case, d_{act} = 4.7 nm, which agrees well with the value obtained from MABNAG simulations (roughly 4 nm) under the same conditions as in Figure 2.4. **b)** Activation diameter versus vapour product. Measured activation diameters at a given temperature correlate inversely with the product of nitric acid and ammonia vapours, in a log-log space. An amount of vapour product that is approximately one order of magnitude higher is required for the same d_{act} at +5 °C than at −10 °C, because of the higher vapour pressure (faster dissociation) of ammonium nitrate when it is warmer. **c)** Equilibrium particle diameter (d_p) at different saturation ratios of ammonium nitrate, calculated according to nano-Köhler theory. Purple curves are for +5 °C and green curves are for −10 °C (as throughout this work). The line type shows the diameter of the seed particle (d_s). The maximum of each curve corresponds to the activation diameter (d_{act}). A higher supersaturation is required for activation at lower temperature.
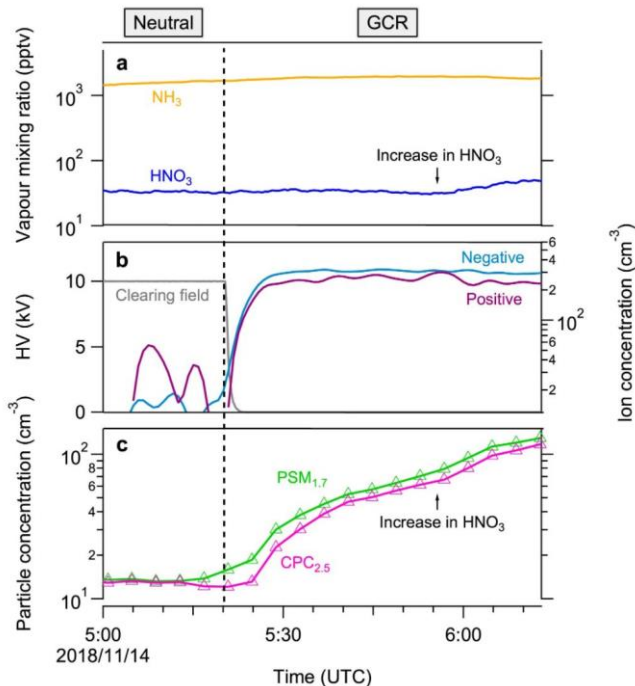
Figure 2.7: A typical measurement sequence. Nucleation was carried out purely from nitric acid and ammonia, with no sulfuric acid (measured to less than 5×10^4 cm^{-3} or 2×10^{-3} pptv), as a function of coordinated universal time (UTC), at 60% relative humidity and −25 °C. **a)** Gas-phase ammonia and nitric acid mixing ratios. The run started with injection of the nitric acid and ammonia flow into the chamber to reach chosen steady-state values near 30 pptv and 1,500 pptv, respectively. The nitric acid flow was increased at 5:53 on 14 November 2018 to prove consistency. **b)** Clearing-field voltage and ion concentrations. Primary ions were formed from galactic cosmic rays (GCR). The clearing-field high voltage (HV) was used to sweep out small ions at the beginning of the run, and turned off at 05:21 on 14 November 2018 to allow the ion concentration to build up to a steady state between GCR production and wall deposition. **c)** Particle concentrations at two cut-off sizes (1.7 nm and 2.5 nm). Particles formed slowly in the chamber under 'neutral' conditions with the HV clearing field on and thus without ions present. The presence of ions ('GCR' condition) caused a sharp increase in the particle-number concentration by about one order of magnitude, with a slower approach to steady state because of the longer wall-deposition time constant for the larger particles. Particle numbers rose again with rising nitric acid.
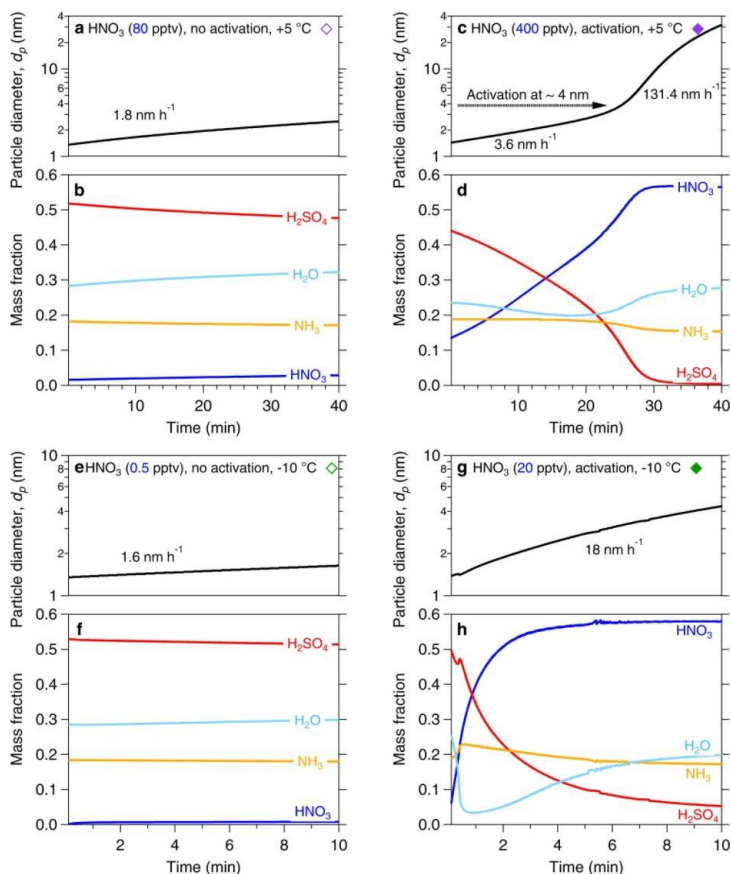
Figure 2.8: Comparison of growth rates and chemical composition in four simulations at +5 °C and −10 °C with the thermodynamic model MABNAG. The simulation points are shown in Figure 2.3a) (filed diamonds, with activation; open diamonds, without activation). **a**, **c**, **e**, **g**, Temporal evolution of the particle diameter. **b**, **d**, **f**, **h**, Temporal evolution of the particle-phase chemical composition. The left-hand column (**a**, **b**, **e**, **f**) shows simulations without activation. The right-hand column (**c**, **d**, **g**, **h**) shows simulations with activation. We set the HNO_3 mixing ratios at 80 pptv and 400 pptv with 1,500 pptv NH_3 at +5 °C, and set the HNO_3 mixing ratios at 20 pptv and 0.5 pptv with 1,500 pptv NH_3 at −10 °C, to simulate unsaturated (**a**, **b**, **e**, **f**) and supersaturated (**c**, **d**, **g**, **h**) conditions, respectively. All other conditions were held constant for the simulations, with the $[H_2SO_4]$ at 2×10^7 cm^{-3} and relative humidity at 60%. Activation corresponds to a rapid increase in the nitric acid (nitrate) mass fraction; the simulations for activation conditions suggest that water activity may be an interesting variable influencing activation behaviour. The activated model results (**c**, **d**, **g**, **h**) confirm that supersaturated nitric acid and ammonia lead to rapid growth of nanoparticles. The simulated activation diameter at +5 °C is roughly 4 nm, similar to that from the chamber experiment (4.7 nm, Figure 2.3a); at −10 °C the simulated activation diameter is less than 2 nm, smaller than observed.
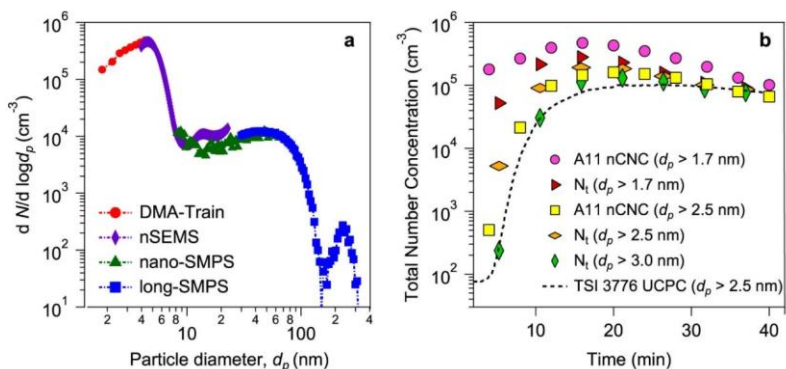
Figure 2.9: Combined particle-size distribution and total concentrations from four particle characterization instruments. a) Combined size distributions, $n°_N(d_p)=d_N/d(\log d_p)$, from four electrical mobility particle-size spectrometers of different, but overlapping, detection ranges. The DMA-Train, nSEMS and nano-SMPS data were averaged every five minutes to coordinate with the long-SMPS scanning time resolution. The tail of the size distribution of large particles outside the detection range was extrapolated by fitting a lognormal distribution. **b)** Comparison of the integrated number concentrations from the combined size distributions in a with total number counts obtained from fixed-cutoff-size condensation particle counters. We obtained the total number concentration of particles, $N_t(d_{p0})$, above a cutoff size, d_{p0}, by integrating the particle-size distribution using [1]: $N_t=\int_{dp0}^{\infty}\{n_N(d_p)\times\eta_{UCPC}\}dd_p$, applying the size-dependent detection efficiency, η_{UCPC} [98], to adjust the integrated total number concentration. We plot the total number concentrations for three different cutoff sizes (d_{p0}) of 1.7 nm, 2.5 nm and 3.0 nm, obtained every 5 min, with coloured symbols as shown in the legend. We also plot measured total number concentrations from two instruments: the Airmodus A11 nCNC-system at nominal cutoff sizes of 1.7 nm and 2.5 nm, and a TSI 3776 UCPC with a nominal cutoff size of 2.5 nm. The Airmodus A11 nCNC-system consists of an A10 PSM and an A20 CPC, which determined both the size distribution of 1–4-nm aerosol particles and the total number concentration of particles smaller than 1 μm (ref. [81]). The TSI 3776 UCPC has a rapid response time and so, rather than the 5-min basis for the other points, we plot the values from this instrument with a dashed curve.
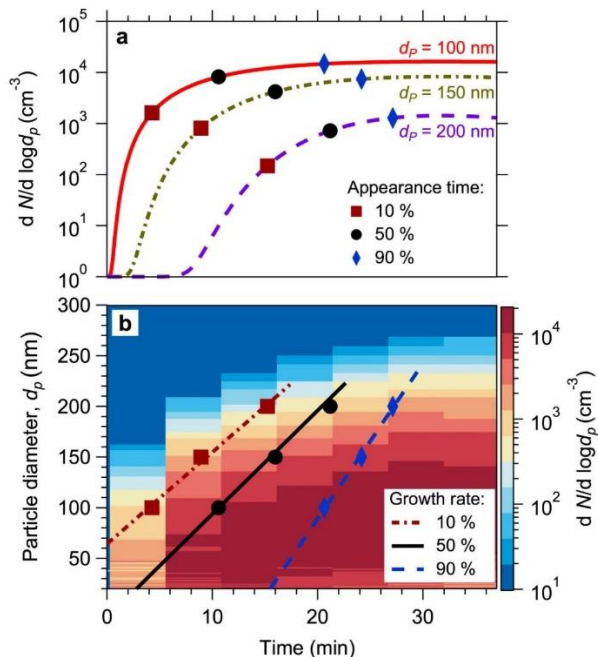
Figure 2.10: Determination of growth rate using the appearance-time method. a) Logarithmic interpolated time-dependent growth profiles for particles with diameters of 100 nm, 150 nm and 200 nm. Three appearance times, when particle number concentrations reached 10%, 50%, and 90% of their maximum, are labelled with different symbols for the three different diameters. **b)** Growth-rate calculation for a rapid growth event (as in Figure 2.2) above the activation diameter. The growth rates, in nm h^{-1}, that we report here are the slopes of linear fits to the 50% (among 10%, 50% and 90%) appearance times calculated from all sizes above the activation diameter (the slope of the solid black line and the black circles in **b**).
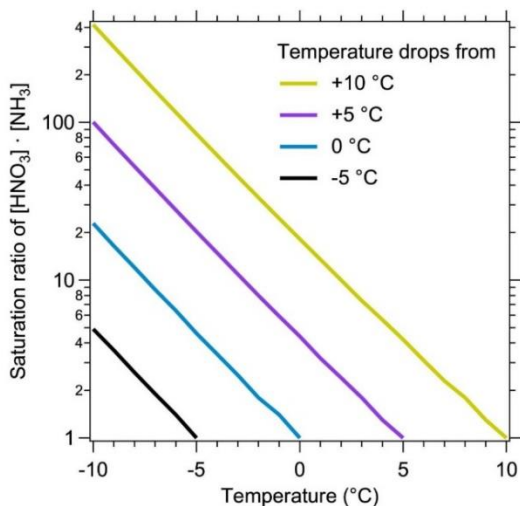
Figure 2.11: Saturation ratio as a function of temperature. At constant nitric acid and ammonia, a decline in temperature leads to an exponential increase in the saturation ratio of ammonium nitrate, shown as the product of nitric acid and ammonia vapour concentration. With an adiabatic lapse rate of −9 °C km^{-1} during adiabatic vertical mixing, upward transport of a few hundred meters alone is enough for a saturated nitric acid and ammonia air parcel to reach the saturation ratio capable of triggering rapid growth at a few nanometers.

Table 2.1: Conditions for all nucleation and growth experiments and nano-Köhler simulations discussed here

Run	T (°C)	HNO$_3$ (pptv)	NH$_3$ (pptv)	H$_2$SO$_4$ (pptv)	HOMs (pptv)	RH %	Saturation ratio of [HNO$_3$]·[NH$_3$]	d_{act} (nm)
2163.01	+20	150	2400	3.60	n/a	60	0.03	n/a
2140.06	+5	860	259	0.96	5.18	60	1.18	9.4
2140.08	+5	971	242	0.84	5.29	60	1.25	10.4
2140.10	+5	1130	244	0.88	5.25	60	1.46	10.0
2170.05	+5	292	370	3.00	n/a	60	0.57	n/a
2170.15	+5	1117	883	1.48	n/a	60	5.24	2.3
2170.20	+5	352	1387	1.48	n/a	60	2.59	4.7
2174.06	+5	640 ^{α}	904	0.46	12.01	60	3.07	3.9
2156.13	−10	228	1085	0.16	n/a	60	131.44	1.6
2156.15	−10	64	2371	0.06	n/a	60	80.90	2.1
2156.17	−10	41	2659	0.07	n/a	60	58.31	2.4
2157.06	−10	n/a	1915	0.44	0.32	60	n/a	n/a
2158.02	−10	59 ^{α}	2654	0.38	0.26	60	82.97	2.9
2158.04	−10	24 ^{α}	2131	0.46	0.28	60	27.06	4.6
2158.06	−10	24 ^{α}	2077	0.36	0.29	60	26.72	4.5
2159.02	−10	23 ^{α}	1835	0.72	0.67	60	22.15	4.5
2159.04	−10	30 ^{α}	1694	1.04	0.78	60	27.07	4.9
2160.02	−10	16 ^{α}	1663	0.60	0.25	60	14.44	5.9
2160.06	−10	16 ^{α}	2535	0.30	0.23	60	22.11	6.5
2062.01	−15 → −24	272	1647	< 0.002	n/a	60 → 40	1252.22	Nucleation
d_s = 1.4 nm	+5	n/a	n/a	n/a	n/a	60	96	2.2
d_s = 2.0 nm	+5	n/a	n/a	n/a	n/a	60	24	3.2
d_s = 2.9 nm	+5	n/a	n/a	n/a	n/a	60	8	4.7
d_s = 1.4 nm	−10	n/a	n/a	n/a	n/a	60	231	2.1
d_s = 2.0 nm	−10	n/a	n/a	n/a	n/a	60	49	3.1
d_s = 2.9 nm	−10	n/a	n/a	n/a	n/a	60	16	4.6

^{α}HNO$_3$ production via NO$_2$ photo-oxidation.

n/a, not applicable; RH, relative humidity.

Table 2.2: Specifications of the four particle-sizing instruments used here

Instrument	Components	Size Range	Size Resolution	Time Resolution
DMA-Train	TSI 3776 UCPC TSI 3776 nanoEnhancer Airmodus A10 PSM	1.8 nm – 8.0 nm	15 bins (interpolated)	5 s
nSEMS	ROMIAC TSI 3760A CPC	1.5 nm – 23 nm	240 bins	1 min
nano-SMPS	TSI 3938 SMPS TSI 3776 UCPC	2 nm – 64 nm	96 bins	1 min
long-SMPS	TSI 3071 DMA TSI 3010 CPC	20 nm – 500 nm	84 bins	5 min

Table 2.3: Ambient particle-formation rates (J), growth rates (GR) and condensation sinks (CS) in various remote and urban environments

City/Region (Country)	J^{α} (cm^{-3} s^{-1})	GR $^{\alpha}$ (nm h^{-1})	CS (s^{-1})	CS·10^4/GR (h nm^{-1} s^{-1})	Reference
Hyytiälä (Finland)	0.8 ± 0.7	3.0 ± 1.9	1.7×10^{-3}	6	[100]
Hyytiälä (Finland)	0.6 ± 0.3	2.9 ± 1.4	$2.1 \times 10^{-3} \pm 8.2 \times 10^{-4}$	7	[101]
Pallas (Finland)	0.1 ± 0.1	2.5 ± 1.7	4.8×10^{-4}	2	[100]
Pallas (Finland)	0.2	3.7	5.3×10^{-4}	1	[102]
Värriö (Finland)	0.9	3.6	1.0×10^{-3}	3	[103]
Värriö (Finland)	0.2 ± 0.3	2.7 ± 1.4	7.0×10^{-4}	3	[100]
Tomsk (Russia)	0.4	5.5	1.6×10^{-3}	3	[104]
Sörmland (Sweden)	0.4 ± 0.4	3.9 ± 2.0	1.7×10^{-3}	4	[100]
Helsinki (Finland)	2.0	3.4	5.1×10^{-3}	15	[105]
Paris (France)	n/a	6.1 ± 1.8	$7.3 \times 10^{-3} \pm 8.0 \times 10^{-4}$	12	[106]
Po Valley (Italy)	5.9	6.8	1.4×10^{-2}	20	[107]
Brookfield (UK)	1.2 ± 0.4	5.3 ± 1.9	$4.5 \times 10^{-3} \pm 2.2 \times 10^{-3}$	9	[108]
Leicester (UK)	1.3 ± 0.4	7.4 ± 0.9	$5.8 \times 10^{-3} \pm 8.7 \times 10^{-4}$	8	[108]
Beijing (China)	n/a	3.2	2.9×10^{-2}	90	[109]
Beijing (China)	10.8	5.2 ± 2.2	$2.7 \times 10^{-2} \pm 2.1 \times 10^{-2}$	52	[110]
Beijing (China)	10.7 ± 6.2	5.2 ± 3.5	$2.2 \times 10^{-2} \pm 1.3 \times 10^{-2}$	42	[111]
Beijing (China)	n/a	6.5 ± 4.5	$2.2 \times 10^{-2} \pm 1.7 \times 10^{-2}$	34	[112]
Hong Kong (China)	3.9 ± 3.5	5.6 ± 2.0	$1.6 \times 10^{-2} \pm 4.2 \times 10^{-3}$	28	[113]
Nanjing (China)	3.7 ± 1.6	7.6 ± 1.2	$2.8 \times 10^{-2} \pm 5.7 \times 10^{-3}$	36	[114]
Nanjing (China)	1.1	8.5	2.4×10^{-2}	28	[115]
Nanjing (China)	n/a	7.6 ± 1.7	$2.3 \times 10^{-2} \pm 6.7 \times 10^{-3}$	31	[20]
Shanghai (China)	8.7 ± 5.2 ^{b}	11.4 ± 9.7	$6.0 \times 10^{-2} \pm 2.4 \times 10^{-2}$	53	[96]
Shanghai (China)	n/a	8.0	2.0×10^{-2}	25	[116]
Gadanki (India)	1.2 ± 2.3	4.1 ± 2.0	$7.1 \times 10^{-3} \pm 4.6 \times 10^{-3}$	17	[117]
New Delhi (India)	7.3 ± 3.9	14.9 ± 1.8	$5.8 \times 10^{-2} \pm 8.9 \times 10^{-3}$	39	[118]
Tecamac (Mexico)	283 ± 121.0 ^{b}	26.0 ± 5.6	$1.3 \times 10^{-1} \pm 2.4 \times 10^{-2}$	49	[97]
Tecamac (Mexico)	n/a	22.6 ± 12.3	$8.2 \times 10^{-2} \pm 3.1 \times 10^{-2}$	36	[97]
Atlanta (US)	n/a	20.0 ± 6.5	$7.4 \times 10^{-2} \pm 1.3 \times 10^{-2}$	37	[52], [119]
Boulder (US)	n/a	5.4 ± 1.0	$2.3 \times 10^{-2} \pm 5.4 \times 10^{-3}$	42	[120]
Boulder (US)	n/a	5.0 ± 1.0	2.2×10^{-2}	43	[116]

$^{\alpha}$ J and GR were mostly calculated over a size range from a few nanometers to more than 20 nm.

^{b} J calculated from 3 nm to 6 nm.

Uncertainties indicate 1σ errors. From references in table

3 Survival of newly formed particles in haze conditions

Ruby Marten[1], Mao Xiao[1], Birte Rörup[2], Mingyi Wang[3], Weimeng Kong[4], Xu-Cheng He[2], Dominik Stolzenburg[2], Joschka Pfeifer[5,6], Guillaume Marie[6], Dongyu S. Wang[1], Wiebke Scholz[7], Andrea Baccarini[1,8], Chuan Ping Lee[1], Antonio Amorim[9], Rima Baalbaki[2], David M. Bell[1], Barbara Bertozzi[10], Lucía Caudillo[6], Biwu Chu[2], Lubna Dada[1], Jonathan Duplissy[2,11], Henning Finkenzeller[12], Loïc Gonzalez Carracedo[13], Manuel Granzin[6], Armin Hansel[7], Martin Heinritzi[6], Victoria Hofbauer[3], Deniz Kemppainen[2], Andreas Kürten[6], Markus Lampimäki[2], Katrianne Lehtipalo[2,14], Vladimir Makhmutov[15], Hanna E. Manninen[5], Bernhard Mentler[7], Tuukka Petäjä[2], Maxim Philippov[15], Jiali Shen[2], Mario Simon[6], Yuri Stozhkov[15], António Tomé[16], Andrea C. Wagner[6], Yonghong Wang[2], Stefan K. Weber[5], Yusheng Wu[2], Marcel Zauner-Wieczorek[6], Joachim Curtius[6], Markku Kulmala[2], Ottmar Möhler[10], Rainer Volkamer[12], Paul M. Winkler[13], Douglas R. Worsnop[17], Josef Dommen[1], Richard C. Flagan[4], Jasper Kirkby[5,6], Neil M. Donahue[3], Houssni Lamkaddam[1], Urs Baltensperger[1], Imad El Haddad[1]

[1]Laboratory of Atmospheric Chemistry, Paul Scherrer Institute, 5232 Villigen, Switzerland.
[2] Institute for Atmospheric and Earth System Research (INAR)/ Physics, Faculty of Science, University of Helsinki, 00014 Helsinki, Finland.
[3]Center for Atmospheric Particle Studies, Carnegie Mellon University, 15213 Pittsburgh, PA, USA.
[4]California Institute of Technology, Division of Chemistry and Chemical Engineering 210-41, Pasadena, CA 91125, USA.
[5]CERN, CH-1211 Geneva, Switzerland.
[6]Institute for Atmospheric and Environmental Sciences, Goethe University Frankfurt, 60438 Frankfurt am Main, Germany.
[7]Institute of Ion Physics and Applied Physics, University of Innsbruck, 6020 Innsbruck, Austria
[8]Extreme Environments Research Laboratory (EERL), École Polytechnique Fédérale de Lausanne, Sion, CH.
[9]CENTRA and FCUL, University of Lisbon, 1749-016 Lisbon, Portugal.
[10]Institute of Meteorology and Climate Research, Karlsruhe Institute of Technology, 76021 Karlsruhe, Germany.
[11]Helsinki Institute of Physics (HIP)/Physics, Faculty of Science, University of Helsinki, 00014 Helsinki, Finland
[12]Department of Chemistry & CIRES, University of Colorado Boulder, 215 UCB, Boulder, 80309, CO, USA.
[13]Faculty of Physics, University of Vienna, Boltzmanngasse 5, A-1090 Vienna, Austria.
[14]Finnish meteorological Insitute, Helsinki, Finland.
[15]Lebedev Physical Institute of the Russian Academy of Sciences, 119991, Moscow, Leninsky prospekt, 53, Russian Federation.
[16]IDL-Universidade da Beira Interior, 6201-001 Covilhã, Portugal.
[17]Aerodyne Research, 01821 Billerica, MA, USA

3.1 Abstract

Intense new particle formation events are regularly observed under highly polluted conditions, despite the high loss rates of nucleated clusters. Higher than expected cluster survival probability implies either ineffective scavenging by pre-existing particles or missing growth mechanisms. Here we present experiments performed in the CLOUD chamber at CERN showing particle formation from a mixture of anthropogenic vapours, under condensation sinks typical of haze conditions, up to 0.1 s^{-1}. We find that new particle formation rates substantially decrease at higher concentrations of pre-existing particles, demonstrating experimentally for the first time that molecular clusters are efficiently scavenged by larger sized particles. Additionally, we demonstrate that in the presence of supersaturated gas-phase nitric (HNO_3) acid and ammonia (NH_3), freshly nucleated particles can grow extremely rapidly, maintaining a high particle number concentration, even in the presence of a high condensation sink. Such high growth rates may explain the high survival probability of freshly formed particles under haze conditions. We identify under what typical urban conditions HNO_3 and NH_3 can be expected to contribute to particle survival during haze.

3.2 Introduction

Aerosols play a key role in cloud formation and climate [3], [121], [122], substantially offsetting the warming by greenhouse gases [123]. It is therefore important to understand what mechanisms are driving the formation and growth of aerosols, so that climate models can include them. Of equal importance, nucleation and growth of aerosols leads to persistent pollution in megacities, which can also be responsible for changes in local weather systems and local climate forcing [32], [58]. In addition, particulate pollution causes millions of premature deaths annually, and is one of the leading causes of deaths globally [7], [8], [57].

Once new particles have been formed, they are able to grow via condensation of vapours. The growth must be fast enough to rival coagulation with larger particles, referred to as the coagulation sink. Particles smaller than 10 nm have high Brownian diffusivity and are therefore

most vulnerable to coagulation loss [59]. The likelihood of a particle's survival is dependent on a balance between growth rate and coagulation sink. Previous understanding was that growth rates in cities are only up to a few times greater than those in clean environments [12]. Therefore, under highly polluted conditions seen in cities, newly formed particles are not expected to survive very long before sticking to larger particles. However, intense new particle formation events are regularly observed under these conditions, with particle formation rates up to hundreds of times higher than in clean environments [16], [96], [110], [124], [125], despite the high loss rates of nucleated clusters. Currently, there is a major gap in our understanding as to how the particle number concentration can be sustained under such highly polluted conditions. Higher than expected cluster survival through the most critical size range (the so-called "valley of death" between nucleated particles and ~10 nm) implies either ineffective scavenging by pre-existing particles or a missing growth mechanism [23].

Recently, Wang *et al.* [126] presented a new mechanism of rapid particle growth, affecting particles as small as a few nanometers, via condensation of HNO_3 and NH_3. Ammonium nitrate is an important semi-volatile constituent of large particles, previously thought to be too volatile to contribute to early growth. However, Wang *et al.* [126] demonstrated that in conditions of excess NH_3 and HNO_3 mixing ratios, with respect to ammonium nitrate saturation ratios, particles as small as a few nanometers can be activated to rapidly grow to much larger sizes, analogous to CCN activation. Ammonium nitrate growth affects particles once they reach a critical diameter, referred to as the activation diameter. This growth mechanism could play a key role in high survival of small particles and therefore explain the maintenance of high particle number concentration under highly polluted conditions. An alternative mechanism that has been also suggested would be that our current understanding of loss rates is incomplete, and clusters are not efficiently lost to large particles [23]. However, neither theory has been experimentally tested or verified to date. In this work, we present the first combined experimental and model results of survival of small particles in the presence of a high coagulation sink, analogous to haze.

3.3 Methods

3.3.1 The CLOUD chamber at CERN

The experiments presented were undertaken at the CLOUD (Cosmics Leaving OUtdoor Droplets) chamber at CERN (European Organization for Nuclear Research). The conditions in the chamber were controlled to 5°C and 60% relative humidity (RH). Further details on the CLOUD chamber experiments can be found in the Supplementary information (SI).

3.3.1.1 Nucleation experiments

We begin the nucleation experiments with a clean chamber and constant gas concentrations. The experiments start by injecting several precursor gases which would be expected in a city, namely NO, SO_2, toluene, α-pinene, HONO, NH_3, O_3, and dimethylamine. Through photolysis of HONO (UVA generated at 385 nm by a 400 W UVA LED saber, LS3) and/or O_3 (170 W quartz-clad high intensity Hg lamp, saber, LS1) OH radicals were produced, and subsequently condensable gases, leading to nucleation and growth of particles. HNO_3 was formed through reaction of ·OH with NO_2; organic oxidation products through reaction of ·OH with volatile organic compounds (VOCs); and H_2SO_4 through reaction of ·OH with SO_2. . In certain experiments, HNO_3 was also injected directly into the chamber. We then monitor the nucleation and growth, and when the stage is deemed finished, the lights are turned off and cleaning and preparation for the next stage begins.

3.3.1.2 High condensation sink experiments

In the high condensation sink experiments, before nucleation attempts began, we generated a high condensation sink, consisting of particles around 100 nm and larger. This was achieved by rapidly growing particles with a high amount of condensable gases (H_2SO_4, HNO_3, NH_3, DMA, and toluene organic oxidation products). Once the condensation sink reached values above 0.06 s^{-1}, the lights were turned off to halt further gas production, and the fan speed in the chamber

was increased, to remove small particles and condensable gases. After the cleaning step, the experimental run was undertaken as described previously (see nucleation experiments).

3.3.2   Modelling ammonium sulfate

The sulfuric acid and ammonia nucleation and growth model is based on the model described in detail in [12] which is developed from the general dynamic equation [1]. Briefly, the model calculates particle and gas concentrations for each time step via a sum of production and losses for each gas, cluster or particle size bin. When organic oxidation products were present in the experiments, nucleation and growth were parameterised in the model to that of the experiment. This was achieved by increasing the H2SO4 concentration used in the model to account for enhanced growth rates since this model does not include organic oxidation products.

3.3.3   Particle loss rates

For the particle loss rates in the chamber, we take into account wall loss, dilution loss, and coagulation loss (or gain). We calculate the coagulation change in each size bin using the coagulation coefficient and the general dynamic equation from [1] and solving for the change in particle number for each size bin for each time step [12], [127].

3.3.4   Modelling ammonium nitrate

We developed an ammonium nitrate growth model addition to the ammonium sulfate model. It is a polydisperse growth model, with 150 bins ranging from one ammonium sulfate cluster to 1000 nm, which also provides the time evolution of particle size and composition. We predict condensation of ammonium nitrate based on the equilibrium of NH_3 and HNO_3 in the gas phase. NH_3 and HNO_3 concentrations are also calculated by summing up production and losses at each time step (injection, photolysis, wall loss, dilution loss, condensation, etc.). For some experiments, gas phase concentration or formation rates were constrained from

measurements. As shown in [126] ammonium nitrate condensation behaves much like CCN activation, and the behaviour is consistent with the nano-Köhler theory. A mass flux is established, based on whether the ammonium nitrate is in supersaturation or not. The supersaturation was calculated based on the dissociation constant K_p [36], defined as the equilibrium product of gas phase NH_3 and HNO_3. Supersaturation of ammonium nitrate is equal to $([NH_3]_g \times [HNO_3]_g)/K_p$. The fluxes of HNO_3 and NH_3 are considered to be equal and dependent on the limiting gas, since formation of ammonium nitrate is equimolar. Therefore, we calculate the net flux of NH_3 and HNO_3 at every time step, and include a Kelvin term and activity term in order to calculate the different fluxes for different particle sizes (see Equation (3.1) SI – modelling ammonium nitrate).

3.4   Results

3.4.1   Modelling rapid growth from ammonium nitrate condensation

Experiments were undertaken at the CLOUD chamber at CERN under various concentrations of H_2SO_4, NH_3 and HNO_3 at 5 °C and 60% relative humidity, and in some instances in the presence of dimethyl amine and/or organic oxidation products formed from α-pinene or toluene. Figure 3.1c) shows experimental CLOUD (2018) and kinetic model results and the dependence of the growth rate of particles after activation by ammonium nitrate on the excess ammonium nitrate concentration. The excess ammonium nitrate is calculated by subtracting the dissociation constant K_p from the product of the gas phase NH_3 and HNO_3 concentrations, this represents the amount of gas available for condensational growth, once the particles have grown as large as the activation diameter. In the majority of CLOUD experiments presented, the limiting gas for condensation was HNO_3, as the experimental design was intended to be comparable to ambient conditions where NH_3 is usually in excess. The modelled growth rates are in good agreement with measured growth rates from CLOUD, and the model replicates qualitatively and quantitatively the evolution of the entire size distribution with particles rapidly growing by ammonium nitrate condensation once they reach a critical diameter of ~4 nm for the experiment shown.
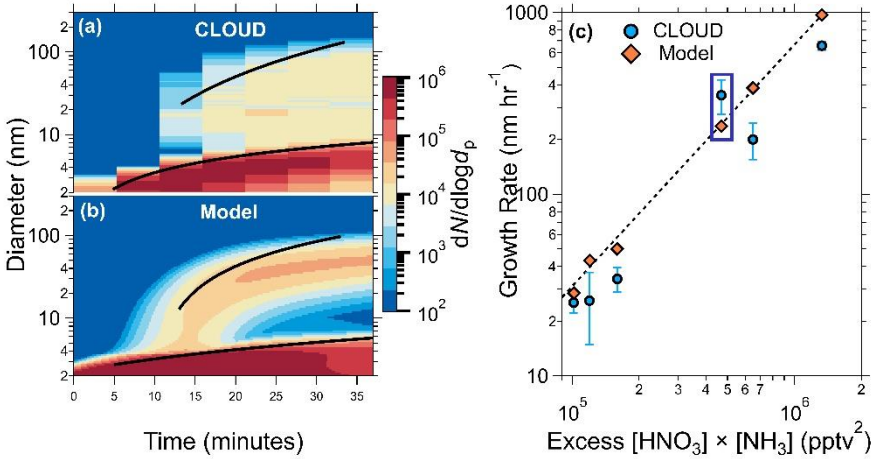
Figure 3.1: Comparison of measured and modelled growth rates a) Particle size distribution from an example CLOUD experiment showing rapid growth from NH_4NO_3 formation once the activation diameter (vapour supersaturation including the Kelvin effect) is reached. **b)** Model prediction for the experiment in **a)**. The black traces in **a)** and **b)** show the 50% appearance time. The initial experimental conditions are 1891 pptv NH_3, 352 pptv HNO_3, and 3.9×10^7 molecules cm^{-3} H_2SO_4. The inputs to the model are the production rates of HNO_3, NH_3, and H_2SO_4, and the Kelvin diameter determined from other CLOUD experiments (see SI – Modelling ammonium nitrate). **c)** Measured particle growth rates after activation versus excess $[HNO_3] \times [NH_3]$ vapour product (round points, previously shown in [126]). The excess vapour product is the supersaturation for the formation of ammonium nitrate, and is determined by subtracting the calculated equilibrium vapour product from the measured value. The round points were determined using the 50% appearance time method (see SI – growth rates). The diamond points show the growth rates obtained by fitting modelled data for each experiment. The growth rates corresponding to panels a and b are indicated by a blue box. The dashed black curve shows a power law fit through the model values of the form $y = kx^p$, with $p = 1.33$ and $k = 7 \times 10^{-6}$. All experiments were performed at 5 °C and 60% relative humidity.

3.4.2   The effect of high growth rates in the presence of high coagulation sink

We generated a high condensation sink (CS), with loss rates comparable to those found during haze, in order to verify experimentally the loss rates of small clusters, and to test the effect of high growth rates on the survival of small particles. Condensation is a sink for condensable gases and depends on the surface area, and coagulation is a sink for particles that depends on the diameter of the colliding particles. In Figure 3.2 we present two CLOUD experiments (one longer

than the other) at 5 °C and 60% relative humidity, summarising the observations (panels a-c, e and f-h, j) and our kinetic model results (panels d and i).

Run 1 of the CLOUD measurements shown in Figure 3.2 (a-c, e) presents results of an experiment in which we observed no nucleation under the initial high CS. The initial concentrations of this experiment were ~ 2.5×10^6 molecules cm^{-3} H_2SO_4, ~ 0.03 ppbv HNO_3, ~6 ppbv NH_3 and an initial CS of ~0.06 s^{-1}. During the experiment the CS steadily decayed due to dilution in the CLOUD chamber, as well as evaporation of NH_4NO_3 due to sub-saturated conditions of gas phase NH_3 and HNO_3. The gas phase NH_3 was constantly increasing, although the injection rate was constant, most likely due to increased production rate of NH_3 by evaporation, combined with a decreasing loss rate to the CS resulting in a higher steady state concentration. HNO_3 should experience the same changes in loss and production rates, but the increase in concentration in Figure 3.2a) is delayed. This is probably due to its higher wall loss rate (i.e. the walls are not an effective source and act as a sink), and the fact that HNO_3 is not in steady state at the beginning of the experiment, as each run starts with the onset of lights and therefore HNO_3 production. Nucleation of particles commenced once the CS dropped to approximately 0.03 s^{-1} (indicated with a vertical orange line). As the condensation sink decreased further, the nucleation rate continued to increase and the particles continued to grow, although at relatively slow rates. In this experiment, neither particle formation and growth nor condensation to the larger mode was sufficient to sustain the particle number and the CS.

Run 2 of the CLOUD measurements in Figure 3.2 (f-h and j) shows a second experiment, with similar initial conditions but higher HNO_3 concentration (~ 6×10^6 cm^{-3} H_2SO_4, ~0.2 ppbv HNO_3, ~1.7 ppbv NH_3, and an initial CS of ~0.06 s^{-1}). We observe that not only were the condensation sink and particle number sustained, but small particles were present from the beginning of the experiment, with measurable and continuous formation of 2.5 nm particles ($J_{2.5}$) as well as high growth rates. Since loss rates of particles to dilution are the same between the two runs, comparing the progression of the large particle mode in Figure 3.2c) and h) can elucidate much about the growth of particles. Although growth does not manifest as a typical new particle formation (NPF) and growth event in Figure 3.2h), it is clear from comparing to Figure 3.2c) that

rapid and continuous growth is occurring. In Figure 3.2c), the lower end of the large pre-existing particle mode increases in diameter due to slow growth of the particles, while the CS and particle number decreases. However, in Figure 3.2h) there are continuous particle concentrations around 10 nm and a steady CS, which can only be explained by new particle formation and rapid growth. Furthermore, as time progresses in Figure 3.2h), the particle number concentration at large sizes (indicated by colour) increases, whereas for Figure 3.2c) it is decreasing. These results indicate that, with sufficient HNO_3 and NH_3, higher growth rates at small particle sizes can shepherd small particles to larger sizes through the so-called "valley of death", and thus sustain particle number concentration and CS during haze events.

Panels e and j present size and time dependent growth rates calculated using the INSIDE method.[128], [129] Panel e shows that initially, before the onset of nucleation, the only measured growth is slow growth of large particles, most likely caused by condensable gases present other than NH_3 and HNO_3. While there are relatively low growth rates for the newly formed particles (< 4 nm) in Panel j, as soon as the activation diameter is reached the particles experience extremely rapid and continuous growth just above the activation diameter, leading to rapid condensational loss, resulting in the apparent gap in the particle-number size distribution. Similar observations of apparent gaps in the particle size distribution, due to ammonium nitrate growth, were also reported in Wang *et al.* (2020).[126] The activation diameter is increasing during the first 20 minutes of Run 2; this is visible as the leading edge of the nucleation mode is increasing in diameter (Figure 3.22 h), concurrent with lower growth rates (Figure 3.2j). As the gas phase NH_3 and HNO_3 concentrations stabilise (Figure 3.2f) the activation diameter also stabilises.

Panels d and i of Figure 3.2 show the kinetic modelling results of these runs. Each model run had initial and boundary conditions consistent with the corresponding experimental run. We initialized both simulations with a condensation sink of ~0.06 s^{-1}, comprising particles with a 100 nm modal diameter. We constrained $J_{2.5}$ and the concentrations of NH_3 and HNO_3 to the experimental values and the production rate of H_2SO_4. For Run 1 (a-e), the model agrees qualitatively and quantitatively with the observations. For Run 2 (f-j) the model agrees

qualitatively but with evident differences that we shall discuss. In Run 1, even with the rise in $J_{2.5}$ after ~ 65 min, the particles only grow a few nm before being lost, and the CS declines steadily due to ventilation without being counterbalanced by newly formed growing particles. A second simulation with $J_{2.5}$ constrained to 10 cm^{-3}s^{-1} throughout the run shows very similar results, with essentially no growth before 65 min and only feeble growth afterwards (SI Figure 3.5 a-b). Sensitivity tests show that the differences in H_2SO_4 and NH_3 between the experiments also do not have a strong influence on the particle size distribution (SI Figure 3.5 c-d). With these experiments, we demonstrate that our current understanding of coagulation loss rates of small particles, which we use in the model, is correct as the results match well with the experiments, i.e. clusters and small particles are efficiently lost to large particles, and inefficient coagulation is not the explanation for measured J rates in polluted conditions.

For Run 2 (f-j) model simulation we found the lower limit where we could reproduce this experiment was at concentrations of ~0.3 ppbv HNO_3 and ~3.8 ppbv NH_3, around two times larger than the estimated concentrations in the chamber. This discrepancy is within the estimated errors of gas concentrations for these runs (see SI). The model reproduces the observed "smear" of particles across the size distribution, with an indistinct minimum near 5 nm. However, the "CS mode" at 100 nm also grows rapidly, in contrast to the observations. The rapidly increasing diameter of the gap in between the nucleation and Aitken modes in panel (i) is most likely an artefact of the initial conditions. We thus confirm the high particle survival as well as the persistent CS, which is sustained against losses as the result of ammonium nitrate-enabled particle activation. The model-measurement differences likely arise from multiple factors, predominantly because experimental conditions were changing dynamically, making it more difficult to constrain the model accurately. As seen in Figure 3.6 - Figure 3.8 (SI) the activation diameter and especially the growth rate are very sensitive to the experimental, or ambient, conditions. Specifically, the growth rate depends on the diameter, and close to the activation diameter, d_{act}, the growth rate rapidly increases with increasing diameter. The sensitivity is especially high when HNO_3 and NH_3 are near stoichiometric equivalence, such as in this case (Figure 3.8). The activation diameter is then also sensitive to the saturation

concentration, S where a small change in S can result in a large change in activation diameter. Finally, certain data limitations (lack of particle composition measurements, lack of HNO_3 measurements etc.) meant that the model could not be constrained to all experimental conditions. The result of these effects is that, in a dynamic situation such as in the CLOUD experiments or ambient environments, we expect to observe a size distribution as we have observed, due to changes in sinks and sources resulting in rapid changes in growth rate and activation. The differences in Figure 3.2 h and i indicate that ammonium nitrate growth would not necessarily be classified as a NPF event, and thus could be overlooked in ambient data. We also do not yet include the effect of Van der Waals forces, which for sulfuric acid – NH_3 growth can enhance sub-10 nm growth by up to a factor of 2 [127]. While Van der Waals forces have a small effect on the overall results, they might contribute to high growth rates in the smallest particles without causing a higher growth at larger sizes (see SI – modelling ammonium nitrate).
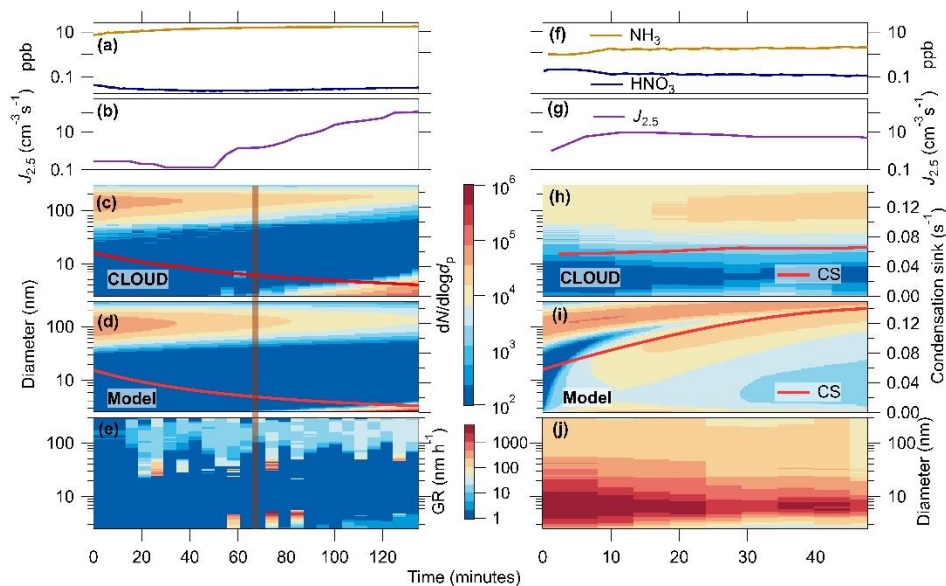
Figure 3.2: Nucleation experiments and model simulations with a high condensation sink in the CLOUD chamber. a-c) A CLOUD experiment with low HNO_3 (~0.03 ppbv) and high initial condensation sink (CS) (0.06 s^{-1}) from pre-existing particles around 100 nm size. The experimental conditions are ~ 2.5×10^6 molecules cm^{-3} [H_2SO_4], ~0.03 ppbv [HNO_3], ~5-20 ppbv [NH_3], 60% RH, and 5 °C. The initial vapour product [HNO_3] × [NH_3] gives an activation diameter of ~30 nm, i.e. particles less than 29.8 nm are in sub-saturated conditions. The CS gradually falls as the particles are flushed from the chamber (diluted) by fresh makeup gas. At 77 minutes, the CS reaches ~ 0.033 s^{-1} (indicated by an orange line) and new particles begin to appear above 2.5 nm (b and c) and grow steadily at a rate of 6.4 ± 1.0 nm hr^{-1}, in the size range 3.2 – 4.9 nm. The formation rate, $J_{2.5}$, continues to increase as the CS falls further. **d)** Model simulation using the measured initial HNO_3 and NH_3 concentrations and H_2SO_4 production rates, and an initial lognormal particle size distribution centred around 100 nm. The model closely reproduces the onset of new particle formation near 65 minutes (orange line). **e)** Size and time dependent growth rates calculated using the INSIDE method. **f-h)** A second CLOUD experiment with higher HNO_3 (0.1-0.2 ppbv) and high initial CS (0.06 s^{-1}) from pre-existing particles around 100 nm size. The experimental conditions are ~ 6×10^6 cm^{-3} [H_2SO_4], ~1.7 ppbv [NH_3], 60% RH, and 5 °C. The initial vapour product [HNO_3] × [NH_3] gives an activation diameter of ~7.5 nm, i.e. particles larger than 7.5 nm are in supersaturated conditions. Under these conditions, we measure steady new particle formation ($J_{2.5}$ = 5 – 10 $cm^{-3}s^{-1}$; panel f) and rapid growth of both the newly formed and the pre-existing particles, which maintains a high CS despite dilution of the chamber contents (panel g). **i)** Model simulation of the second CLOUD experiment. The initial vapour product for the simulation has an activation diameter of 2.5 nm, i.e. particles larger than 2.5 nm are in supersaturated conditions. The model predicts continuous new particle formation as well as rapid growth of both the new particles and the pre-existing particles. The reason for the different appearance of the measured (h) and simulated (i) size distributions is due to varying experimental conditions (see text). **j)** Size and time dependent growth rates calculated using the INSIDE method.

3.4.3   Effect of NH_3 and HNO_3 concentrations on particle survival

Results from Figure 3.1 and Figure 3.2 indicate that the model accurately captures the growth by ammonium nitrate, as well as particle loss rates; therefore, the model most likely accurately represents the underlying physics and chemistry of particle growth associated with ammonium nitrate activation. We now use the model to explore under which atmospherically relevant conditions ammonium nitrate condensation could enhance the survival of newly formed particles.

The model was run at 5 ^{o}C with NH_3 and HNO_3 concentrations ranging from 400 pptv – 4 ppbv and the condensation sink ranging from 0.01 to 0.13 s^{-1} covering a range of low particle surface area to extremely high limits. We define the survival parameter as the ratio of the formation rate of 6 nm (J_6) particles to that of 2.5 nm ($J_{2.5}$) particles at steady state, i.e. the proportion of how many particles survived between 2.5 and 6 nm. We feed the model with 2.5 nm particles ($J_{2.5}$ = 10 cm^{-3}s^{-1}) and assume no evaporation of clusters of H_2SO_4 (kinetic nucleation). All model runs have the same production rate of H_2SO_4, which, in the absence of a condensation sink, leads to ~ 10 nm hr^{-1} early growth (1.8-3.2 nm) for non-activated particles.

Figure 3.3 indicates the calculated ammonium-nitrate-driven growth rate at 3 nm of model and CLOUD experiments via symbol colour, with points plotted as survival parameter against condensation sink. The fuchsia diamond symbols represent a CLOUD run with low amounts of HNO_3, as in Figure 3.2, panels a-c. We can see that as the CS decayed and particles began to grow that the survival significantly increased compared to at higher CS. The purple diamond symbols represent the run with higher HNO_3 (Figure 3.2 panels f-h and j), and these points along with the model points show us that at high growth rates, the condensation sink has little effect on the survival, and these points even approach unity. Although there is relatively high survival at low condensation sinks (~ 0.01 s^{-1}), even with slower growth rates, at high condensation sinks the only experiments that saw high survival were those with activation and high growth rates. This confirms our theory that high growth rates are able to "shepherd" small particles through size ranges where they are most vulnerable to loss.
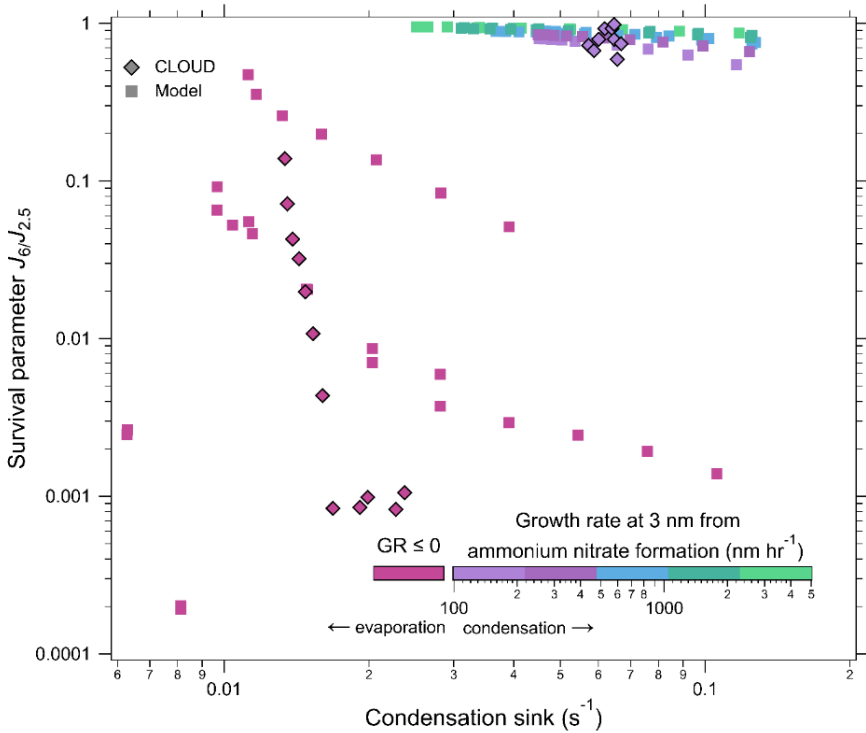
Figure 3.3: Survival parameter of newly formed particles versus condensation sink. The survival parameter is defined as the particle formation rate at 6 nm divided by the formation rate at 2.5 nm, i.e. $J_6/J_{2.5}$. CLOUD measurements are indicated by diamond symbols and model simulations by square symbols without outlines. The points are coloured according to the particle growth rate at 3 nm, calculated from the measured HNO_3 and NH_3 concentrations (Figure 3.1), the fuchsia colour indicates conditions of either no growth (GR=0) or evaporation of NH_4NO_3 (GR<0). The CLOUD experiments are those shown in Figure 3.2, the experimental conditions are listed in its caption. All the model simulations assume kinetic nucleation (zero evaporation), and ~ 10 nm hr^{-1} early growth (from H_2SO_4) for non-activated particles, in the absence of any particle condensation sink. The model assumes a constant $J_{2.5}$ of 10 cm^{-3} s^{-1}. The model conditions are 5 °C, HNO_3 and NH_3 between 400 pptv and 4 ppbv, and a condensation sink between 0.01 and 0.13 s^{-1}. Experiments where the activation diameter is sufficiently low that the non-activated growth surpasses it result in activation of particles. Activated particles grow rapidly enough to survive loss in the presence of high condensation sinks whereas non-activated particles have very low survival probabilities. The experimental measurements show that the rapid particle growth rates from ammonium nitrate formation are sufficient to overcome losses of newly formed particles in high condensation sink environments. The good agreement of the model with the experimental data confirms that particle scavenging involves unit sticking probability, as expected from previous measurements in low condensation sink environments.

3.5 Discussion and Conclusions

Figure 3.4 illustrates results from model runs over the selected concentration ranges. As can be seen, the results are almost binary, with a sharp transition from a region of no survival to a region of high survival, showing how crucial activation is for survival. In parts b and c, at high HNO_3 concentrations, the effect of the condensation sink is very small. This can also be seen in part d of the Figure 3.4, but with the calculated growth rate caused by ammonium nitrate formation (at 3 nm) on the x-axis. Growth rates from ammonium nitrate formation directly scale with the flux of HNO_3 and NH_3. The ammonium nitrate flux is dependent on the concentration of gas phase NH_3 and HNO_3, as well as on which gas is limiting, and the size of the particle, the full equations are found in the SI. The region between negative and positive growth rates (evaporation and condensation, respectively) is where we see a step in survival, and above this region the condensation sink has a smaller effect. In panel d, it is also more visible that at calculated negative growth rates the survival is highly dependent on the condensation sink (though it is always low). In this region, the survival is controlled by H_2SO_4 and NH_3 growth, as without activation HNO_3 does not contribute to nucleation and growth. Although the calculated flux, and therefore growth rate, of ammonium nitrate is negative, when there is no ammonium nitrate in the particles evaporation will not occur.

Survival of particles will depend on not only the growth rate, but also the activation diameter, since if particles are not large enough for NH_3 and HNO_3 to condense on there will be no activation. Therefore the contribution of activation to survival of particles will also depend on the pre-existing particle distribution. Since we constrain $J_{2.5}$ in our model, and the experiments with positive flux shown in Figure 3.4d-e) have activation diameters under 2.5 nm, all of the particles can be activated.
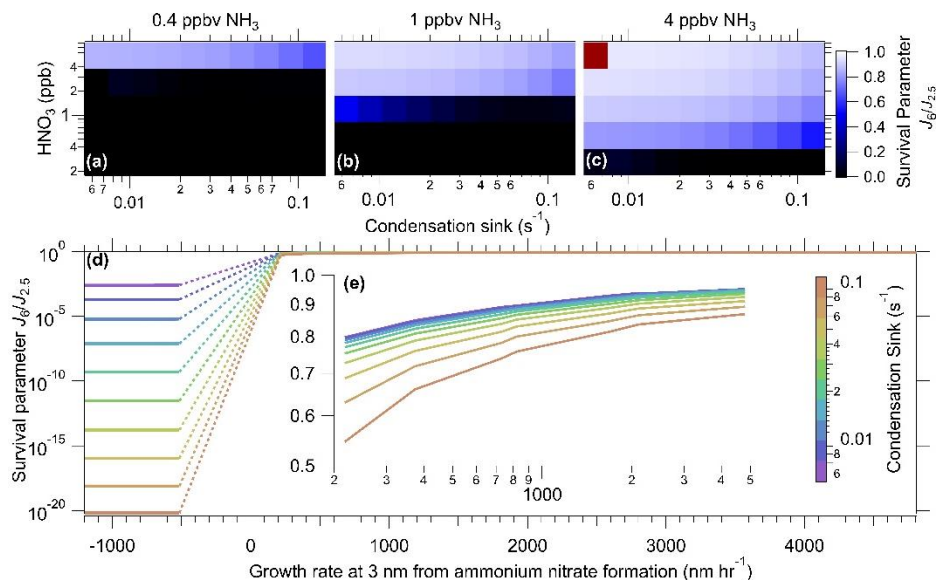
Figure 3.4: Illustration of the binary behaviour of modelled survival of newly formed particles due to ammonium nitrate formation. a-c) Modelled particle survival parameter as a function of condensation sink and concentrations of HNO_3 and NH_3 at 5 °C. The model assumes constant HNO_3 and NH_3 concentrations and H_2SO_4 production rate, and simulates a variable CS at 300 nm. The red square in panel c is a model where the CS and J rates did not stabilise within the time of the model. **d)** Particle survival parameter versus the calculated growth rate at 3 nm for different condensation sinks. When the growth is not positive, i.e. no condensation, the particle survival parameter, $J_6/J_{2.5}$, is extremely low and around 5×10^{-4} for CS = 0.005 s^{-1}. However, above the activation diameter, the total particle growth rates increase by up to a factor of 100 or more and the survival parameter approaches unity, even for condensation sinks as high as 0.1 s^{-1}. The dashed line in between positive and negative growth rates represents a range with no data points. **e)** An insert of **d)** with only growth rates above 0.

The observed differences in Figure 3.2 parts (g) and (h) give a strong indication that although these processes may happen under ambient conditions, they are most probably masked to researchers as they do not appear as typical NPF events. This is especially the case because deviations from equilibrium are expected to be brief in the ambient atmosphere, and vapour concentrations of NH_3 and HNO_3 tend rapidly towards equilibrium. However, even short perturbations above saturation may drive the rapid growth of nucleating particles at rates up to

one thousand times faster than growth by H_2SO_4 condensation, given the disparity between HNO_3 and H_2SO_4 concentrations. Particles may not experience rapid growth for long, but they can grow sufficiently fast to escape the valley of death and continue to grow via other condensable gases. In ambient conditions, transient deviations from equilibrium are expected to occur, especially in inhomogeneous urban settings with strong local sources of ammonia (e.g. from traffic or urban geometry). Since HNO_3 is usually the limiting gas, inhomogeneities in HNO_3 could have a larger impact on particle size distributions, however since NH_3 is directly emitted by a multitude of sources, it is more likely to be variable and therefore will likely have a larger impact in typical urban environments. Wang *et al.* (2020)[126] show the strong temperature dependence of ammonium nitrate formation, therefore we also expect temperature changes characteristic of vertical convection to drive the vapour concentrations of NH_3 and HNO_3 out of equilibrium. Future analysis should investigate the effect of urban and vertical mixing on the rapid growth of nucleating particles by NH_3 and HNO_3 condensation.

While Wang *et al.* (2020)[126] presented the first evidence of rapid growth by ammonium nitrate condensation, we have additionally provided the first experimental data and supporting modelling calculations demonstrating efficient scavenging of nucleating molecular clusters by larger sized particles under haze conditions. We also present experimental results of high survival of freshly nucleated particles even in the presence of a high condensation sink, confirming the hypothesis from Wang *et al.* (2020)[126] that rapid growth caused by NH_4NO_3 formation can aid in particle survival through the valley of death. These results strongly support the hypothesis that the unexplained survival of particles is due to a missing growth mechanism, and that under typical ambient conditions of a megacity at 5 °C, rapid ammonium nitrate condensation could be that missing mechanism, increasing survival of nucleated particles, and thus sustaining particle number and poor visibility during haze.

3.6 Author contributions

Conceptualization: R.M., M.X., M.W., J.Dommen, J.K., N.M.D., H.L., U.B. and I.E.H. Resources, prepared the CLOUD facility or measuring instruments: R.M., B.R., M.W., W.K., X.-C.H., D.S., J.P., G.M., D.S.W., W.S., A.B., C.P.L., R.B., L.C., B.C., J.C., L.D., J.Duplissy., H.F., L.G.C., M.G., A.H., M.H., V.H., D.K., A.K., M.K., K.L., V.M., H.E.M., B.M., O.M., T.P., M.P., J.S., M.S., Y.S., A.T., R.V., A.W., Y.Wang, S.K.W., P.M.W., Y.Wu, M.Z.-W., R.C.F., J.K., H.L., and I.E.H. Investigation: R.M., M.X., B.R., M.W., W.K., X.-C.H., D.S., J.P., G.M., D.S.W., W.S., A.B., C.P.L., A.A., R.B., D.B., B.B., L.C., L.D., J.Duplissy, H.F., L.G.C., M.G., M.H., V.H., D.K., M.L., V.M., B.M., J.S., M.S., A.T., A.W., S.K.W., Y.Wu, M.Z.-W., J.K., H.L., and I.E.H. Formal analysis: R.M., B.R., M.W., W.K., X.H., D.S., J.P., G.M., D.S.W., W.S., C.P.L., L.C., L.D., M.S., S.K.W., P.M.W., R.C.F., N.M.D., H.L., and I.E.H. Scientific discussion: R.M., M.X., B.R., M.W., W.K., X.-C.H., D.S., W.S., C.P.L., D.B., J.C., L.D., H.F., K.L., J.Dommen., R.C.F., J.K., N.M.D., H.L., U.B., and I.E.H. Writing: R.M., B.R., M.W., W.K., X.-C.H., D.S., J.P., D.S.W., J.Dommen., J.K., N.M.D., H.L., U.B., and I.E.H.

3.7 Conflicts of interest

There are no conflicts to declare

3.8 Acknowledgements

3.9   Supplementary Information

3.9.1   Summary

This supplementary information (SI) section describes the CLOUD chamber and details of experimentation and instrumentation used at CLOUD, CERN. Details of the parameters calculated from CLOUD results (such as growth rates) and details of the kinetic model set up and equations used are also presented.

3.9.2   The CLOUD chamber at CERN

The CLOUD chamber is 26.1 cubic meters, is made of stainless steel, and the inside surface is electro-polished [66], [75]. The chamber concentrations are kept homogeneous via turbulence created by two magnetically coupled stainless steel fans at the top and bottom of the chamber [130], with mixing times typically on the order of a few minutes. The dilution (ventilation) lifetime is 1.3 hours. Wall loss rates of gases and different sized particles are also well characterised [127]. Precursor gases are injected via a state-of-the-art gas system that allows us to control dilution and injection flows to control the gas concentrations with great accuracy. The trace gases are injected into the chamber along with dry air, formed by mixing 79% boil-off nitrogen and 21% boil-off oxygen (both Messer, 99.999%) and water is added from an evaporator using ultrapure water (18 MΩ cm, Millipore Corporation) in order to control the relative humidity. Note that in this study experiments were done without use of the 3.5 GeV/c secondary pion beam (π beam) from the CERN PS.

The experiments presented in this paper involved varying mixtures of gases capable of nucleation and growth; sulfuric acid, ammonia, dimethylamine, nitric acid, and HOMs generated from toluene and α-pinene. Experiments started when lights were turned on and condensable gases were formed by photolysis (and further reactions). The various lights used in these experiments resulted in a homogeneous illumination of the chamber. These different sources were: three UV sources including four 200 W Hamamatsu Hg-Xe lamps (UVH), a 170 W quartz-

clad high intensity Hg lamp (saber, LS1), and a 4 W KrF 248 nm excimer UV laser (UVX); further, UVA was generated at 385 nm by a 400 W UVA LED saber (LS3). LS1, UVH, and UVX were used to photolyse ozone, and LS3 was used to photolyse HONO, both in order to generate OH radicals. After each experiment, the particles and condensable gases were cleaned from the chamber by increasing the fan speed and thus the loss rates of particles, and gas concentrations were set up for the subsequent experiment.

The high condensation sink runs were extremely challenging to perform. For example, in instances where the condensation sink was decreasing over time, the gas phase NH_3 was constantly increasing, although the injection rate was constant. The large amount of HNO_3 generated in building up the condensation sink was also the cause of depletion of reagent ions in the Br⁻ CIMS, and so the HNO_3 was modelled for certain experiments (see modelling nitric acid).

3.9.3 Instrumentation

To measure gas-phase nitric acid, a Br⁻ chemical ionisation atmospheric pressure interface time of flight mass spectrometer (CI-API-TOF-MS) was deployed in the CLOUD chamber at CERN. We used a commercially available inlet from Airmodus for the mass spectrometer, which is optimised for minimum wall loss. The details of measurements can be found in the Methods section of [126]. During some experiments, the Br⁻ ion was depleted in the Br- CIMS due to high levels of HNO_3, and so HNO_3 was modelled from other time-series (see modelling nitric acid).

H_2SO_4 and HOMs were also measured by a CI-API-TOF-MS but with nitrate reagent ions. There were two NO_3^- CIMS present, one was equipped with an inlet from Airmodus, and the other used a home-made inlet and corona discharge for ion generation[44]. Both instruments were equipped with an electrostatic filter so as not to measure naturally formed ions from the CLOUD chamber. The detection limit of the condensable gases measured by the NO_3^- CIMS was approximately 5 x 10^4 cm⁻³. Calibration techniques for H_2SO_4 and HOMs have been described previously [63], [81].

Volatile organic compounds (VOCs) were measured by two different custom built proton transfer reaction time of flight mass spectrometers, a selective reagent ionization time of flight mass spectrometer (SRI-ToF-MS) described in [42] and the PTR3-ToF-MS described in [43]. Both instruments used H_3O^+ ions to charge compounds of the sample gas. Humidity dependent calibrations of toluene were performed by directly measuring a gas standard (Apel Riemer Environmental Inc) at specific conditions of the respective experiments. These instruments were also used to analyze the cleanliness of the chamber in between experiments.

Ammonia and DMA were measured by a water cluster CI-API-TOF-MS, this instrument is described in detail in [45]. The instrument introduced a newly designed cross-flow ion source. The authors report the limit of detection of ammonia to be ~ 0.5 pptv and predict the detection limit of DMA to be lower.

A suite of instruments covering different size ranges measured the particle number and size distribution between 1.5 nm and 487 nm. Starting with the smallest size, the instruments used were: a nano condensation nucleus counter (nCNC) [46]; a differential mobility analyser train (DMA-Train) [47]; a nano-scanning electrical mobility spectrometer (nSEMS) [48]; a nano-scanning mobility particle sizer (nano-SMPS); and a long SMPS.

The A11 nano Condensation Nucleus Counter is composed of a particle size magnifier (PSM) connected in series with a condensation particle counter (CPC). The PSM is an aerosol pre-conditioner that uses diethylene glycol (DEG) to grow aerosol particles to a size that is easily detected by the CPC. The saturator flow rate inside the PSM can be adjusted so aerosol particles of different sizes are activated. During CLOUD13, the PSM saturator flow was set to scanning, meaning it measured the particle size distribution between 1.5 and 2.5 nm [131], [132].

The DMA train is built up of 6 different DMAs in parallel, measuring the range 1.8 - 4.3 nm each with different fixed voltages, to allow different size ranges, and the particles are counted by either a PSM or CPC depending on the size; Stolzenburg *et al*. [47] describe the instrument in detail.

The nSEMS is a newly developed instrument that operates in the range of 1.5 – 25 nm. For classification of particle size, the nSEMS uses a radial opposed migration ion and aerosol classifier (ROMIAC), which is capable of measuring particle diameters down to the nanometer level with less degradation and less sensitivity to diffusional resolution degradation than the DMAs. A full description of the instrument can be found in [48].

The nano and long SMPS are commercially available instruments and have been fully characterised and described in previous studies [89]–[91]. Together, the nano-SMPS and long-SMPS scan range spanned from 4 to 487 nm. Particles larger than 487 nm were formed during runs with high condensation sinks. For these experiments, a multi-peak fitting routine was applied to deconvolve the observable size distribution into component modes, which were assumed to be lognormal in shape. The fitting results were then used to estimate the particle size distribution from 487 nm to 1036 nm. This was necessary for us to better calculate the condensation sinks and J rates, since the existence of larger particles will influence these parameters.

Ozone (O_3, Thermo Environmental Instruments, TEI 49C), sulfur dioxide (SO_2 Thermo Fischer Scientific Inc. 42i-TLE), and nitric oxide (NO, ECO Physics, CLD 780TR) were measured by gas monitors. Nitrogen dioxide was also measured but by a cavity attenuated phase shift NO_2 monitor (CAPS NO_2, Aerodyne Research Inc.). A custom-made cavity-enhanced differential optical absorption spectrometry instrument (CE-DOAS) was also used to measure NO_2 and HONO. Relative humidity of the chamber was measured by two instruments, dew point mirrors (EdgeTech) and an in situ-TDL-Hygrometer (KIT, CERN). Temperature was measured by mid-plane internal PT100 temperature sensors placed at 5 different distances from the chamber wall. The sensor that was closest to the midpoint of the chamber, 1.2 m from the wall, was used as the chamber's reference temperature.

3.9.4   Growth rates

Growth rates were calculated using the 50% appearance time method [64]. This method works best in chamber or flow tube experiments, as it relies on the identification of a growing particle distribution easily differentiated from other particles. Since the CLOUD chamber is cleaned before each experiment, and new particles are nucleated from gases rather than injected, it is easy to differentiate the growing particles. This was more difficult in the case of the high condensation sink runs, as there were many pre-existing particles of different sizes, and thus the reason why growth rates are not reported for these runs. The model was set up to give output of different size bin concentrations at every time step (0.1 s) so growth rates could be calculated in the same way as experimental data, where the sizing instrument output also gives size-distributed particle concentrations. Each size bin concentration over time is fit to the following function using a least-squares solver:

$$S_{d_p}(t) = \frac{a - b}{1 + (^t/_{t_{app}})^d} + b \qquad (3.1)$$

Size and time dependent growth rates calculated using the INSIDE method were presented in Figure 3.2.[128] This method is based on the adapted, size-integrated GDE, where the growth rate is solved for using experimental inputs for other variables. Full details of this method can be found in Pichelstorfer *et al*. (2018).[128] GDE-based GR methods might suffer from statistical fluctuations in the size-distribution measurement that may cause significant error. However, Ozon *et al*. (2021) [129] showed that for well-controlled chamber experiments, the INSIDE method agrees well with a fixed interval Kalman smoother which estimates the GR error for similar experiments to those in Figure 2a-e) to be roughly 1 nm hr^{-1}, or at maximum 50% for more dynamic situations such as in Figure 2f-j).

Where S_{d_p} is the signal or concentration of a particular diameter (d_p) bin, a and b are the background and plateau concentrations respectively, d is a free parameter which relates to the steepness of the sigmoidal increasing curve, and t_{app} is the 50% appearance time, which is equal

to the time at which 50% of the concentration (in between background and plateau) has been reached. The appearance time for each bin is then plotted against the particle diameter and a linear fit is made to present growth rates in nm hr^{-1}. For a full description see the Supporting Information of [64].

3.9.5   Formation rates

Formation rates were determined using the balance equation between the particle sources and sinks as per [133] shown in equation (3.2):

$$J_x = \frac{dN_{\geq x}}{dt} + S_{dil} + S_{wall} + S_{coag} \tag{3.2}$$

Where the units of J are (particles) cm^{-3} s^{-1} and S_{dil}, S_{wall}, and S_{coag} are terms for dilution loss, wall loss, and coagulation loss, respectively.

Formation rates of particles of diameter 2.5 nm were reported as a 2.5 nm particle is thermodynamically stable and larger than the critical radius [1]. 2.5 nm particles are also commonly measured in ambient campaigns and thus it is valuable for comparison. The total number concentration of particles with diameters 2.5 nm and above was measured using the nCNC.

3.9.6   Activation diameter

During the CLOUD experiments, when there was an activation event, the particle size bins just above the activation diameter tended to have low concentrations, due to fast growth after activation (faster than the time resolution of the instrument). The activation diameter was therefore determined by identifying the first time step where a bimodal distribution occurred, and the largest size bin of the smaller mode, where the concentration dropped, was identified as the activation diameter. For further information on this technique see the supporting information of [126].

3.9.7   Modelling ammonium nitrate

The flux of ammonia and nitric acid to a certain size particle is calculated using the following equation.

$$\phi_{i,p} = \underbrace{N_p^s \pi d_p^2}_{\text{Area: } A_p^s} \underbrace{\left(\frac{E_{i,p}^\mu \varepsilon_{i,p} e_{i,p} \alpha_{i,p} \bar{s}_i B_{i,p}}{4} \right)}_{\text{Collision speed: } s_{\text{I},p}^\perp} \underbrace{\left[c_i^v - a_{i,p}^s K_{i,p} c_i^o \right]}_{\text{Driving force: } F_{i,p}^{v,s}}$$

$$\underbrace{\phantom{N_p^s \pi d_p^2 \left(\frac{E_{i,p}^\mu \varepsilon_{i,p} e_{i,p} \alpha_{i,p} \bar{s}_i B_{i,p}}{4} \right) \left[c_i^v - a_{i,p}^s K_{i,p} c_i^o \right]}}_{\text{Flux per unit surface area: } \varphi_{i,p}^{v,s}}$$

(3.3)

$$\bar{s}_i = \sqrt{\frac{8k_b T}{\pi m_i}}$$

(3.4)

The subscript i denotes the gas species, i.e. NH$_3$ or HNO$_3$ (depending on which is limiting), and the subscript p refers to the particle size. Where N_p^s is the particle number and d_p is the diameter. The collision speed is derived from the average molecular speed (Equation (3.5)), and includes terms reflecting Van der Waals interactions between the vapour and particle (charge - dipole, dipole - induced dipole, and induced dipole - induced dipole), $E_{i,p}^\mu = E^\mu(H_{i,p})$ where $H_{i,p}$ is the Hamaker constant in Joules; the non-zero size of the vapour, $\varepsilon_{i,p} = (d_i^2 + d_p^2)/d_p^2$; and the non-infinite mass of small clusters, $e_{i,p} = \sqrt{(m_i + m_p)/m_p}$. A term for gas-phase diffusion limitations is $B_{i,p} \simeq 1$ for large Knudsen numbers. The mass accommodation coefficient, $\alpha_{i,p}$, can also be included, this was assumed to be 1 for these calculations. The driving force depends on vapour concentration, c_i^v, and saturation concentration, c_i^o, as well as the activity in the solid phase and the kelvin term. Since the Hamaker constant for ammonia is 0, the enhancement from Van der Waals interaction is only relevant in acid-limiting conditions, and has the greatest effect at lower sized particles. This enhancement was not included in the kinetic model for this paper, but it may explain some of the difficulty in duplicating the experiment in Figure 3.2 Run

2, since the enhancement of growth at small sizes would have the small particles grow faster than the large particles in the CS.

We simplify the flux per unit surface area calculation to

$$\varphi_{i,p}^{v,s} = s_{i,p}^{\perp} \, c_i^v \, \gamma_{i,p} \tag{3.5}$$

$$\gamma_{i,p} = \left| 1 - \frac{a_{i,p}^s}{a_i^v} K_{i,p} \right| \tag{3.6}$$

where $\gamma_{i,p}$ is defined as the uptake coefficient and can be defined in terms of the saturation ratio of the gas, where the saturation ratio is equal to the activity in the vapour phase divided by the activity in the solid phase times the kelvin term to account for the curvature of the surface of a particle.

$$\gamma_{i,p} = \left(1 - \frac{1}{S_{i,p}} \right) = \frac{S_{i,p} - 1}{S_{i,p}} = \frac{S_{i,p}^{XS}}{S_{i,p}} \tag{3.7}$$

$$S_{i,p} = \frac{a_i^v}{a_{i,p}^s K_{i,p}} \tag{3.8}$$

We can consider the flux as equal due to the 1:1 stoichiometry of condensation of ammonium nitrate, and thus we define a collision ratio, r_{AB}^v, which is the concentration ratio scaled by the collision speed of each molecule. The subscripts A and B are now used for acid and base.

$$\varphi_{A,p}^{v,s} = \varphi_{B,p}^{v,s} \tag{3.9}$$

$$s_{A,p}^{\perp} \, c_A^v \, \gamma_{A,p} = s_{B,p}^{\perp} \, c_B^v \, \gamma_{B,p} \tag{3.10}$$

$$\gamma_{B,p} = \frac{s_{A,p}^{\perp} \, c_A^v}{s_{B,p}^{\perp} \, c_B^v} \, \gamma_{A,p} \tag{3.11}$$

$$\gamma_{B,p} = r_{AB}^v \, \gamma_{A,p} \tag{3.12}$$

$$r_{AB}^v = \frac{s_{A,p}^{\perp} \, c_A^v}{s_{B,p}^{\perp} \, c_B^v} \tag{3.13}$$

In the case of base limiting experiments, $S_{B,p}$ is then found iteratively using the following equation, solved by combining Equations (3.7), (3.9) and (3.10). If the experiment is acid limiting, the difference in solving for $S_{A,p}$ is to replace r^v_{AB} with $1/r^v_{AB}$.

$$S_{B,p} = \frac{S_{AB,p}}{2}\left[\left(\frac{r_{AB}^v - 1}{r_{AB}^v}\right) + \sqrt{\left(\frac{r_{AB}^v - 1}{r_{AB}^v}\right)\frac{4}{r_{AB}^v S_{AB,p}}}\right] \tag{3.14}$$

Where $S_{AB,p}$ is the saturation of ammonium nitrate

$$S_{AB,p} = \frac{a_A^v a_B^v K_{AB}^{eq}}{K_{AB,p}} = \frac{x_A^v x_B^v}{K_{AB,p} K_p} \tag{3.15}$$

$$K_p = \frac{p_B^o p_A^o}{K_{AB}^{eq}} \tag{3.16}$$

Where x^v_A and x^v_B are the mixing ratios of nitric acid and ammonia respectively, K^{eq}_{AB} is the equilibrium constant for $NH_3(s) + HNO_3(s) \rightleftharpoons NH_4 \cdot NO_3(s)$, K_p is an overall dissociation constant for ammonium nitrate condensation, i.e. $NH_3(v) + HNO_3(v) \rightleftharpoons NH_4 \cdot NO_3(s)$, [36], and $K_{AB,p}$ is the Kelvin term for ammonium nitrate, correcting for the curvature effect of different sized particles.

$$K_{AB,p} = 10^{\left(d_{K10}/d_p\right)} \tag{3.17}$$

The Kelvin diameter for ammonium nitrate at 5 °C was calculated by fitting the data from CLOUD experiments (SI Figure 3.6) according to the relationship shown in Equation (3.18).

$$S_{AB,p} = 10^{\left(d_{K10}/d_{act}\right)} \tag{3.18}$$

3.9.8   Modelling nitric acid

In the two CLOUD experiments with high condensation sink (Figure 3.2), there were no accurate measurements of HNO_3 due to depleted reagent ions, and therefore the time-series presented are modelled concentrations. A box model was set up where HNO_3 was solved for based on sums of production and losses at each time step.

$$\frac{\partial HNO_3}{\partial t} = source_{injection} + source_{NO_2+\cdot OH} - loss_{wall+dilution} - loss_{condensation\ sink} \tag{3.19}$$

This model was tested on other CLOUD experiments and agreed with the measurements from the Br⁻ CI-API-TOF-MS within a factor of two.

OH was modelled in a similar way using the AtChem online solver where the chemical mechanistic information was taken from the Master Chemical Mechanism, MCM v3.3.1 [134], [135]. Inputs were measured time-series of various trace gases, photolysis rates of ozone and HONO, and chamber wall and dilution losses specific to CLOUD.
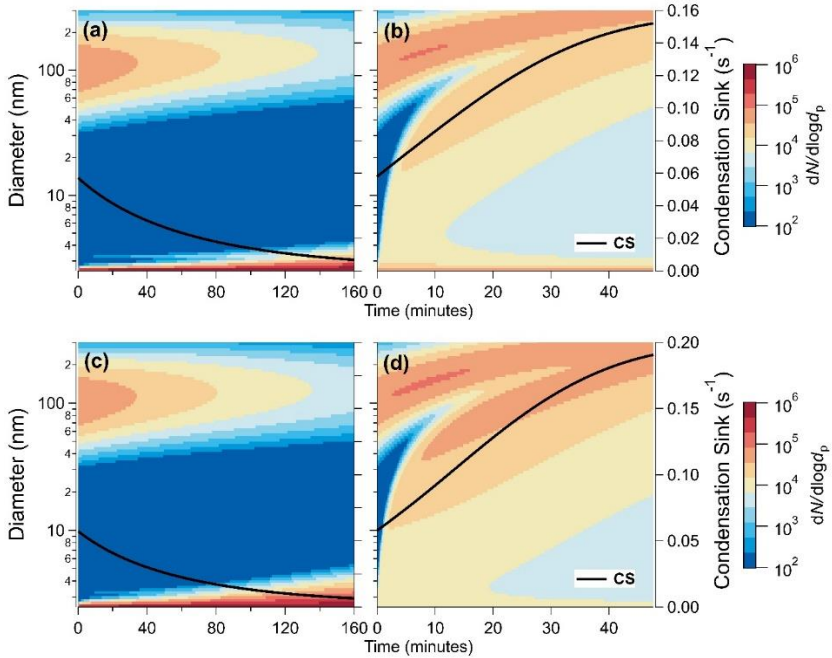
Figure 3.5: Sensitivity tests on gas phase concentrations and formation rates on modelled results of Figure 3.2. This figure is a repeat model of the runs in Figure 3.2 d and i of the main text but with **a-b)** $J_{2.5}$ constrained to 10 cm^{-3}s^{-1}, and **c-d)** $J_{2.5}$ constrained to 10 cm^{-3}s^{-1} as well as H_2SO_4 and NH_3 concentrations switched between the two experiments. All other experimental conditions are the same. The model results are similar to those in Figure 3.2 panels d and i, with little to no growth in the low HNO_3 case (a,c), and the "smear" of particles of all sizes in the high HNO_3 case (b, d).
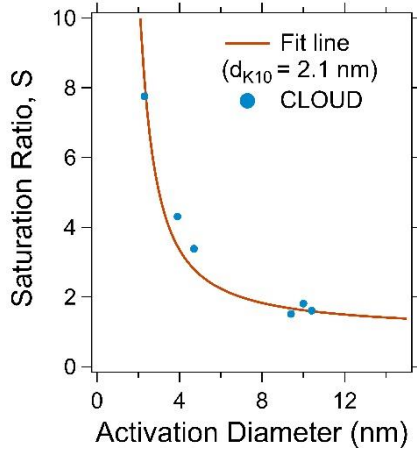
Figure 3.6: Saturation ratio vs activation diameter. Blue markers represent measured activation diameters from CLOUD experiments and saturation ratios calculated from measured HNO_3 and NH_3 gas phase concentrations. The red fit line is fit to this data and then used to calculate the Kelvin diameter for use in the model.
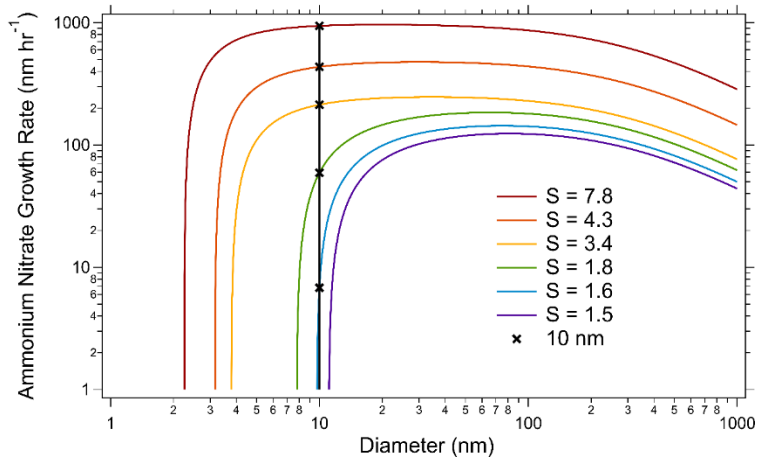

Figure 3.7: Diameter vs calculated growth rates from flux equations. The curves are calculated using the equations in the section "Modelling ammonium nitrate". The six *S* curves plotted are using *S* calculated from the HNO_3 and NH_3 gas concentrations from the six CLOUD experiments shown in Figure 3.1. It is apparent that at low diameters the growth varies dramatically, around the activation diameter for each *S* value.
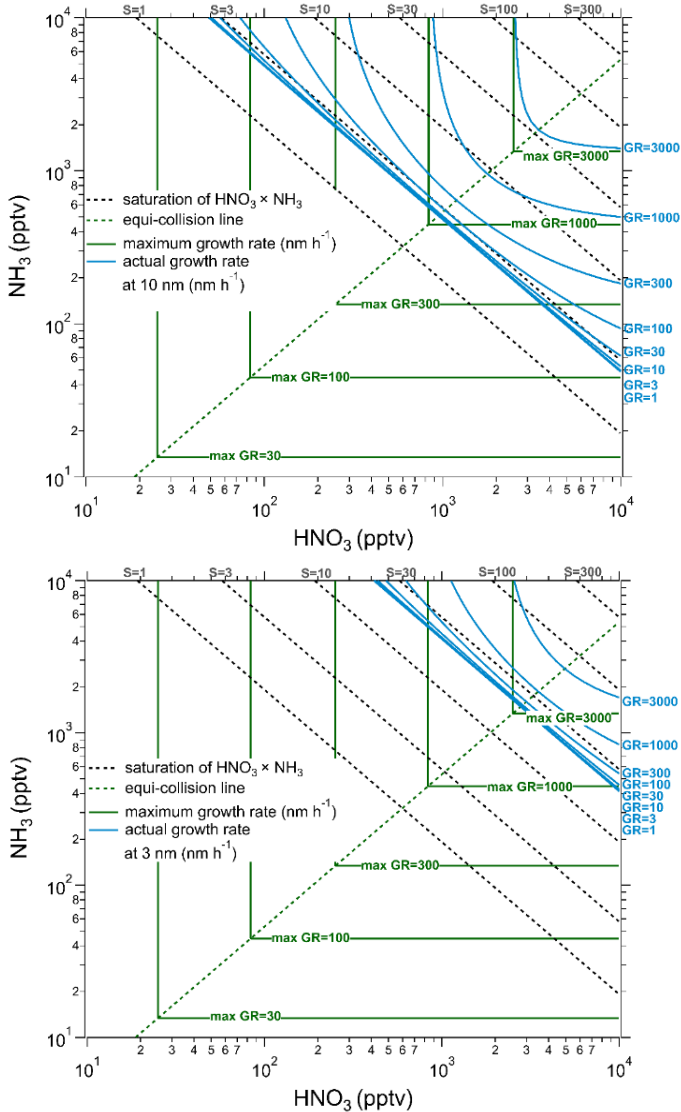
Figure 3.8: Calculated growth rates of condensation of ammonium nitrate. The phase space shown is between 1 pptv and 10,000 pptv (10 ppbv) at 5 °C. The top panel shows growth rates for a particle of 10 nm and the bottom panel shows growth rates for a particle of 3 nm (the same size used for calculating growth rates in Figure 3.2) The calculations for growth rate include the Kelvin effect using the Kelvin diameter calculated (see modelling ammonium nitrate).

4   Role of nitric acid and ammonia in particle growth in the polluted boundary layer

Ruby Marten[1], Mao Xiao[1], Birte Rörup[2], Mingyi Wang[3], Weimeng Kong[4], Xu-cheng He[2], Dominik Stolzenburg[2], Joschka Pfeifer[5,6], Guillaume Marie[6], Dongyu S. Wang[1], Wiebke Scholz[7], Andrea Baccarini[1,8], Chuan Ping Lee[1], CLOUD collaboration[5], Joachim Curtius[6], Markku Kulmala[2], Ottmar Möhler[9], Rainer Volkamer[10], Paul M. Winkler[11], Douglas R. Worsnop[12], Josef Dommen[1], Richard C. Flagan[4], Jasper Kirkby[5,6], Neil M. Donahue[3], Houssni Lamkaddam[1], Urs Baltensperger[1], Imad El Haddad[1]

[1]Laboratory of Atmospheric Chemistry, Paul Scherrer Institute, 5232 Villigen, Switzerland.
[2] Institute for Atmospheric and Earth System Research (INAR)/ Physics, Faculty of Science, University of Helsinki, 00014 Helsinki, Finland.
[3]Center for Atmospheric Particle Studies, Carnegie Mellon University, 15213 Pittsburgh, PA, USA.
[4]California Institute of Technology, Division of Chemistry and Chemical Engineering 210-41, Pasadena, CA 91125, USA.
[5]CERN, CH-1211 Geneva, Switzerland.
[6]Institute for Atmospheric and Environmental Sciences, Goethe University Frankfurt, 60438 Frankfurt am Main, Germany.
[7]Institute of Ion Physics and Applied Physics, University of Innsbruck, 6020 Innsbruck, Austria
[8]Extreme Environments Research Laboratory (EERL), École Polytechnique Fédérale de Lausanne, Sion, CH.
[9]Institute of Meteorology and Climate Research, Karlsruhe Institute of Technology, 76021 Karlsruhe, Germany.
[10]Department of Chemistry & CIRES, University of Colorado Boulder, 215 UCB, Boulder, 80309, CO, USA.
[11]Faculty of Physics, University of Vienna, Boltzmanngasse 5, A-1090 Vienna, Austria.
[12]Aerodyne Research, 01821 Billerica, MA, USA

In preparation

4.1 Abstract

Aerosols formed and grown by gas-to-particle processes are a major contributor to smog and haze in megacities, despite the competition between growth and loss rates. Rapid growth rates from ammonium nitrate formation can contribute to sustained particle number in highly polluted conditions. This process requires supersaturation of gas phase ammonia and nitric acid with respect to ammonium nitrate saturation ratios. Urban environments are inhomogeneous. In the troposphere, vertical mixing is fast, and aerosols may experience rapidly changing temperatures. In areas close to sources of pollution, gas phase concentrations can also be highly variable. In this work we present results from nucleation experiments at -10°C and 5°C in the CLOUD chamber at CERN. We verify, using a kinetic model, how long supersaturation is likely to be sustained under typical haze conditions with temperature and concentration inhomogeneities, and the impact it can have on the particle size distribution.

4.2 Introduction

Aerosols affect global and local climate by aerosol-radiation interactions and aerosol-cloud interaction, where aerosol-cloud interactions are the larger forcing agent [3]. Aerosols must grow into the 50–100 nm diameter size range to be able to act as cloud condensation nuclei (CCN) [1]. As well as acting as CCN, particles in the accumulation mode (100 – 1000 nm) are relatively stable in the atmosphere, due to their low diffusivity and slow settling velocity. Nucleation and growth of aerosols in urban environments can lead to persistent pollution, which is a leading cause of disability and death [7], [8]. Therefore it is important to investigate key drivers of nucleation and growth.

Nucleation and growth in urban environments has been studied in depth in ambient measurements, chamber experiments, and models [16], [96], [110], [124], [125]. In polluted conditions, the high number of large particles act as a high coagulation sink (CS), which is a large loss term for small particles (<10 nm) as they have high Brownian diffusivity and so collisions with larger particles are more frequent [1]. In order for newly formed particles to escape

scavenging by the CS, the growth rates need to outcompete the loss rates [59]. Aerosols grow from condensation of vapours and ambient measurements suggest that growth rates in cities are only up to a few times greater than those in clean environments, although the loss rates are much higher. Due to this, newly formed particles are not expected to be able to grow to high sizes in polluted conditions. Nevertheless, new particle formation events have often been observed, with particle formation rates up to hundreds of times higher than in clean environments [12]. Until recently there was no experimental evidence for an explanation of the persistence of high particle number concentrations sustained over long periods of time in the face of high loss processes. Wang *et al.* [126] introduced a new mechanism of ammonium nitrate formation which rapidly grows particles as small as a few nanometers to much larger sizes. Marten *et al.* [136] showed that this growth was high enough to grow small particles through the most critical size range (the "valley of death" from nucleation until approximately 10 nm) even in the presence of high condensation sinks, thus sustaining particle number concentrations. They also presented evidence that small particles are efficiently scavenged by larger particles and therefore over-estimating of loss rates is not the reason for the discrepancy in particle survival.

The mechanism of growth via ammonium nitrate formation is extremely sensitive to temperature, as the Kelvin diameter (and therefore activation diameter) as well as saturation concentration and therefore growth rates are dependent on the temperature of the system. Urban environments are inhomogeneous environments. In the troposphere, mixing is relatively fast, especially vertical mixing, which involves a change in temperature [1], [68]. Furthermore, there are many sources with highly variable emission rates which result in varying gas phase concentrations [26].

In this study we present CLOUD and model results of growth from ammonium nitrate at 5°C and -10°C, showing that the kinetic model is capable of replicating behaviour at different temperatures. Additionally we use the kinetic model to assess how perturbations in temperature and concentration of NH_3 affect the growth of ammonium nitrate, and whether

ammonium nitrate could be supersaturated in typical urban conditions on a timescale relevant to make significant changes to the existing particle size distribution.

4.3   Methods

4.3.1   CLOUD experiments

The experiments presented were undertaken in the CLOUD chamber at CERN in 2018. The CLOUD chamber is a 26.1 m^3 stainless steel nucleation chamber with controllable temperature, relative humidity, mixing speed, and irradiation [66], [75], [130]. Gas concentrations are controlled by a state of the art injection system. Experiments were performed at 5°C and -10°C, at 60% relative humidity, all experiments were conducted without use of the 3.5 48 GeV/c secondary pion beam (π beam) from the CERN PS. In order to onset nucleation, condensable gases such as sulfuric acid (H_2SO_4), ammonia (NH_3), di-methyl amine, and organic oxidation products were generated. This was achieved via photolysis of ozone and or HONO to generate OH radicals with UVA generated at 385 nm by a 400 W UVA LED saber and/or a 170 W quartz-clad high intensity Hg lamp. Rapid growth via ammonium nitrate formation was achieved by supersaturation of gas phase NH_3 and HNO_3, by injecting directly into the chamber, or producing HNO_3 via reaction of NO_2 and •OH. All precursor gases are in steady state when the experiments are started by the onset of photolysis and optimal mixing in the chamber. For further experimental details see [136].

4.3.2   Model

A kinetic model illustrating growth from ammonium nitrate formation was developed and presented in [136]. It was shown that the model could accurately replicate results from CLOUD experiments at 5°C. The model was revised to conditions at -10C. The main changes are a new Kelvin diameter fit from CLOUD experiments at -10°C (SI), and adjusting other parameters that are temperature dependent, such as the saturation concentration of ammonium nitrate (K_p), the collision rate of particles, and the deposition speed of gas phase ammonia and nitric acid. In

a few experiments at -10°C we saw an enhancement of growth from N_2O_5 uptake, for these experiments we parameterise for N_2O_5 by using additional HNO_3, and do not use these data points for fitting the Kelvin diameter. The model was further adapted to model ambient conditions, for example the wall and dilution losses of the chamber were replaced with diffusion losses for particles and gases. We also include a simulated high condensation and coagulation sink with an initial lognormal particle size distribution, which is centred around 200 nm.

4.3.2.1   *Air parcel rising*

For experiments where we simulated an air parcel rising by a change in temperature, we constrained the temperature time-series to that of an increase and decrease in height. We also adjusted the temperature sensitive parameters as explained in the previous section. The temperature change used is 15°C within 15 minutes as the air packet rises and falls.

4.3.2.2   *Concentration inhomogeneities*

In order to simulate inhomogeneities in the atmosphere, we constrained a time-series of NH_3 concentration with ambient relevant 'spikes'. We looked to ambient time-series for inspiration on how often and how high we can expect increases in NH_3 concentration (SI). This is heavily dependent on location, the time-series used is meant to simulate air parcels close to a point source of ammonia, for example near to a busy road. The spikes were separated into two categories, less frequent larger spikes, and more frequent smaller spikes. The larger spikes were 10 ppbv for 3 minutes whereas the smaller spikes were 2 ppbv for 2 minutes. The background ammonia concentration was 1 ppbv. This is a low estimation for background ammonia, but it allows for exploring the effect of small and large perturbations in the concentration. The NH_3 concentration was chosen to vary over HNO_3 since there are more available ambient time-series of NH_3 to base our time-series on, and since it is directly emitted it is more likely to be variable.

4.4   Results

Experiments involving growth from ammonium nitrate formation were undertaken at 20°C, 5°C and -10°C in the CLOUD chamber at CERN. The experiments were designed to use atmospherically relevant concentrations of all gases, due to this fact, and that the supersaturation of ammonium nitrate is temperature dependent, we did not observe any ammonium nitrate growth at 20°C. Figure 4.1a) shows results from all of the CLOUD experiments as triangular points where the newly formed particles were activated by ammonium nitrate formation. We observe that at the lower temperature, lower gas phase concentrations can result in higher growth rates. This is partially due to the fact that the saturation concentration of ammonium nitrate is lower at lower temperatures and therefore more NH_3 and HNO_3 can condense. Plotted with this data, as diamond points, are the growth rates obtained from model simulations with constrained gas phase concentrations of HNO_3 and NH_3 from CLOUD measurements. We use the Master Chemical Mechanism (MCM, [134], [135]) to model the chemistry in the chamber, using measured gas-phase time-series, measured loss rates, and photolysis rates from CLOUD. For the three points indicated in Figure 4.1a) at -10°C by a blue oval, we calculated that there was tens to hundreds of pptv N_2O_5. Original model results using HNO_3 concentrations (SI Figure 4.4) showed these points with far too low growth rates. We then parameterised for N_2O_5 by including additional HNO_3, which brought the experiment and model results closer together. The growth rates are plotted against the limiting gas for ammonium nitrate formation, which is either NH_3 or HNO_3. The limiting gas will determine how much NH_4NO_3 can be formed and thus we see increasing growth with increasing concentration. Although the relationship of GR and concentration is not strictly linear as it also depends which gas is limiting (see [136] SI for full explanation) it is used only as a method to display the data. Figure 4.1b) shows all of these data points again, but with the modelled growth rates on the x-axis and corresponding measured CLOUD growth rates on the y-axis, and a dashed line for x=y. From these two plots we can see that the kinetic model is able to replicate CLOUD results not only at 5°C but also at -10°C.
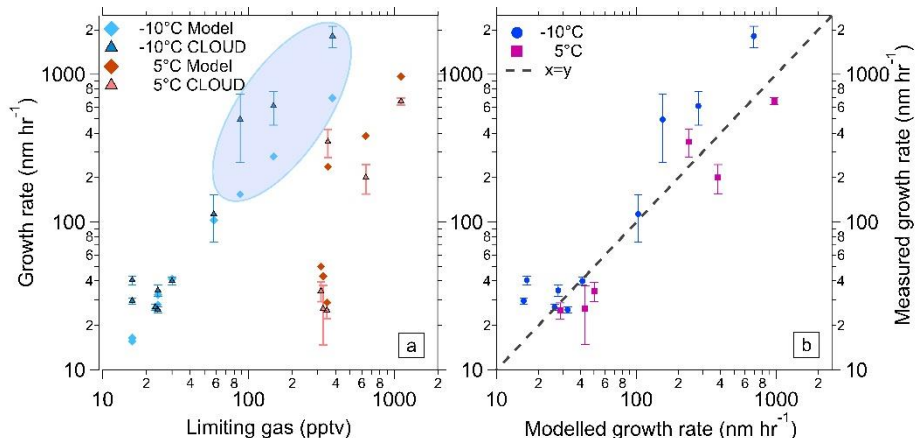
Figure 4.1: Comparison of measured and modelled growth rates at 5°C and -10°C. a) Measured (triangles with error bars) and modelled (diamonds) growth rates at 5°C and -10°C, 60% RH, versus the limiting gas for ammonium nitrate condensation, which is either ammonia or nitric acid and is experiment dependent. The CLOUD measurements were determined using the 50% appearance time method [64]. The modelled data points were determined using the same method on output from the kinetic model, constrained by measured gas phase concentrations from CLOUD experiments. The blue oval indicates experiments were N_2O_5 was also present, and may have contributed to growth. All measured data points and modelled data points at 5°C were previously presented in [126] and [136]. b) Modelled growth rates versus measured growth rates at 5°C and -10°C for all the experiments shown in **a**).

Since the model is now capable of simulating ammonium nitrate growth at different temperatures, we explored the effect of changing temperature on an air parcel in a city, i.e. an air parcel rising and therefore decreasing in temperature, on the overall size distribution. In these experiments we also include an initial particle size distribution which is lognormal and centred around 200 nm, in order to simulate a high condensation/coagulation sink. More details can be found in the Methods section and SI. Figure 4.2 shows the size distribution vs time of an air parcel with constant temperature (Figure 4.2a)), an air parcel with a decrease and subsequent increase in temperature (Figure 4.2c)) and the respective temperature profiles plotted in Figure 4.2b). The activation diameter (d_{act}) is defined as the critical size at which ammonium nitrate can condense on particles and is dependant on the temperature, gas phase concentrations of NH_3 and HNO_3, and the Kelvin diameter. d_{act} is plotted as a purple line in both Figure 4.2a) and b) and the sums of all particles above 50 nm ($N_{>50}$) are scattered as black points.

$N_{>50}$ is identical for both sets of conditions at the start, but by the end of the experiment $N_{>50}$ is substantially larger for the temperature change simulation. We can see that during both temperature drops the activation diameter decreases and particles as low as 6 nm can rapidly grow from ammonium nitrate formation. The largest newly formed particles start to rapidly grow from less than 10 nm to over 100 nm. When the temperature increases as the air parcel returns to ground level, between 35-50 minutes, there is some evaporation of NH_4NO_3, and a slight shrinking in the size distribution visible in the original condensation sink, and the crest of the newly growing particles. We observe the same effect for the second temperature change, between 70-85 minutes, and then leave the model to come to steady state conditions at ground level. Figure 4.2d) shows the size distributions at the beginning and end of the experiments with and without a change in temperature; since initial size distributions are identical only one is plotted. We can see that in the case of constant temperature, there are two distinct modes, with a minimum particle concentration around 50nm. However in the experiment with changing temperature a new mode is present, with considerably larger concentrations in the range of 30-80nm.

The nucleation rates used for these models were at the kinetic limit, i.e. assuming no evaporation of clusters. We performed sensitivity test on the nucleation rates and found that similar effects are observed with lower nucleation rates (SI Figure 4.5). With lower nucleation rates there are fewer particles present to activate, and so the effect of ammonium nitrate activation is someone lessened. It is clear that this phenomena depends on the pre-existing particle size distribution, since there need to be particles present larger than the activation diameter for ammonium nitrate to be able to condense. SI Figure 4.5 shows that when the activation is started at a later time in the model, where particles have grown larger, the effect is more pronounced. We also performed sensitivity tests of the temperature range (SI Figure 4.5) and observed that a larger temperature range also results in more pronounced activation. Although there are many factors that affect the condensation of ammonium nitrate, as long as there are particles present above the activation diameter activation will occur and rapidly grow particles to larger, more stable sizes.

These results tells us that when air is constantly vertically mixing in a polluted environment, growth from ammonium nitrate formation may help to increase the particle number of larger sizes and aid in survival of newly formed particles through the valley of death, even after returning to surface temperature and sub-saturated conditions.
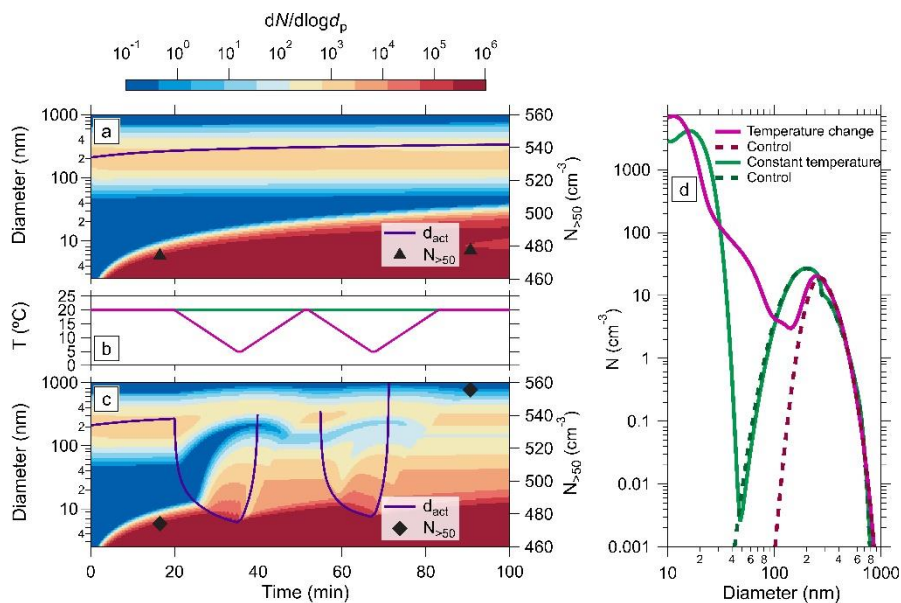

Figure 4.2 Model simulation of a temperature change in an air parcel due to vertical transport. a) Size distribution of an experiment with constant temperature with a purple trace showing d_{act} and black points indicate the total particle concentration above 50 nm. Initial conditions are 3 ppbv NH_3, 3.7ppbv HNO_3 and 1×10^7 molecules cm^{-3} H_2SO_4. **b)** Temperature profiles for a) (green) and b) (pink). **c)** Size distribution of an experiment with a temperature change simulating an air parcel moving up and down with a purple trace showing d_{act} and black points indicate the total particle concentration above 50 nm. Initial conditions are the same as in a). **d)** Particle size distributions for the points indicated in a). The experiment with the temperature change has a large increase in particles between 30-80nm, where the newly formed particles have grown to, whereas when there is no temperature change there is a much smaller change in the particle size distribution.

In polluted environments air parcels will experience inhomogeneities in gas-phase concentrations as well as vertical mixing. We therefore set up a simulation with a variable ammonia time-series, meant to represent an area close to a source with large, sporadic variations in ammonia, such as traffic [26]. We also include the same initial particle size

distribution as in the previous section. Figure 4.3a) shows an experiment with fixed production rates of HNO_3, NH_3, and H_2SO_4. By the end of the simulation we can see that the newly formed particles have grown to around 20 nm. In Figure 4.3c) the simulation in a) is repeated but with a variable NH_3 time-series, with alternate "spikes" of 10 ppbv and 2 ppbv and a background concentration of 1 ppbv. The NH_3 time-series is presented in b). We observe that the newly formed particles have grown much higher than in a), and have even grown into the original condensation sink. The particle concentration of particles above 50 nm, represented by black diamonds in a) and c), increases in c) as new particles grow, whereas it steadily decreases in a). Figure 4.3d) shows the size distributions corresponding to the first and last diamond points in a and c). The blue trace, representing the final diamond in a), differs from the starting size distribution with the appearance of the nucleation mode up to around 20 nm and by growth of the largest particles as the second mode shift right. In addition to these changes, the orange trace, which represents the end diamond in c), has dramatically increased particle number concentration up to 200 nm. This leads us to similar conclusions as from Figure 4.2, that inhomogeneities can sustain particle number by causing temporary supersaturation of ammonium nitrate, and growing particles through the valley of death.
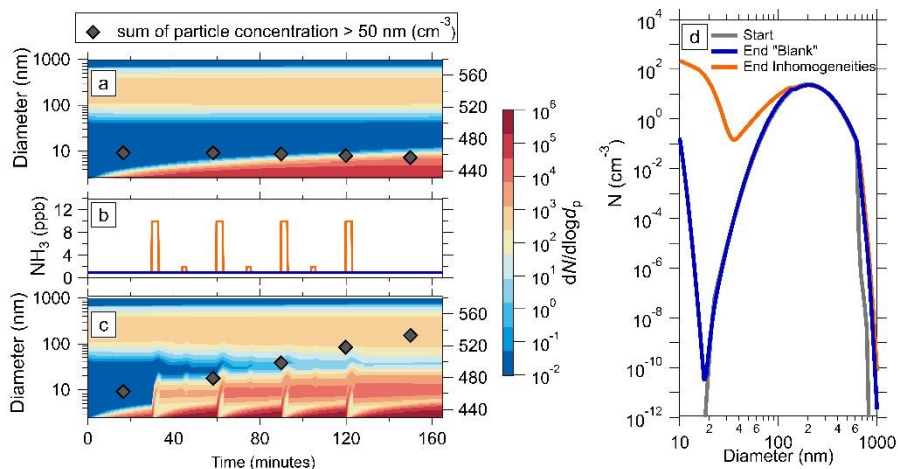
Figure 4.3 Model simulation of inhomogeneities in the NH₃ time-series. a) Model simulation at 5°C with constant injection rates of NH₃ and HNO₃ with sum of all particles above 50 nm scattered in diamond points which are steadily decreasing. Initial concentrations are 1 ppbv NH₃, 0.2 ppbv HNO₃, and 1×10^7 molecules cm^{-3} H₂SO₄. **b)** Gas phase concentrations of NH₃ from a) (blue) and b) (orange). **c)** Model experiment at 5°C with alternating 10 ppbv and 2 ppbv high 'spikes' of NH₃ concentration with duration of three and two minutes, respectively, simulating inhomogeneity. Initial conditions are the same as in a). The sum of all particles above 50 nm is scattered in diamond points and is steadily increasing. **d)** Particle size distributions at the start and end of a) and c).

In all of the simulations presented, we also model the particle composition throughout. SI Figure 4.6 shows examples of plots with the relative concentrations of ammonium nitrate and ammonium sulfate. These results show that the fraction of NH₄NO₃ is only significant during the supersaturated periods and above the activation diameter. Once sub-saturated conditions resume, the ammonium nitrate quickly evaporates. However, Figure 4.2 and Figure 4.3 show that even after NH₄NO₃ evaporates into gas phase NH₃ and HNO₃, the edge of the growing particle size distribution still survives at higher sizes than before activation. This is since H₂SO₄ more readily condenses on larger particles and the particles have grown through the valley of death and are less susceptible to loss rates.

4.5   Discussion and Conclusions

In light of these results, it is curious that similar size distributions as in Figure 4.3 have not been frequently observed in ambient measurements. SI Figure 4.7 shows the same size distribution as in Figure 4.3c) but with a time resolution of 5 minutes, and the diameter resolution and range of a long-scanning mobility particle sizer (as used in CLOUD). The features are not as distinguished as those presented from the model results. In the simulations presented in Figure 4.3c) the inhomogeneities lasted only 2-3 minutes, which would be challenging to capture on an instrument with a 5 minute resolution. This results in a smoother border of the high condensation sink and growing size distribution, with some features which could be interpreted as noise. Furthermore, usually more than one particle sizing instrument would be required to measure the diameter range and resolution presented from model results. Finally, these measurements would need to take place near to a large source of NH_3 or HNO_3, such as traffic or industry, and background sites would therefore not measure such distributions. In regards to temperature changes, ambient measurements often observe sudden increases or decreases in particles due to transport of particles, and so it is likely this phenomenon would not be easily measured.

It is important to point out that this model does not take into account the effect of relative humidity on the ammonium nitrate system. Since all of the experiments were performed with a relative humidity lower than the deliquescence relative humidity (DRH), ammonium nitrate was formed as a solid; however, this will not always be the case in ambient conditions. The DRH depends on the temperature of the system, so that at higher temperatures the DRH is lower. Above the DRH, the dissociation constant will decrease with increasing relative humidity and so conditions are even more likely to be supersaturated than in corresponding dry conditions. Ammonium nitrate ionic strength also affects the dissociation constant, where K_p decreases with increasing ionic strength. As well as dependence on temperature and relative humidity, a particle's size will also affect whether it is a solid or liquid droplet. Due to the kelvin effect, water is less likely to condense on smaller particles, and therefore even at high relative humidity small

particles will be dry. In summary, larger particles in wet conditions will be liquid, and since this affects the dissociation constant, more ammonium nitrate should be able to condense on particles and increase the effect of NH_4NO_3 growth on the particle size distribution. This effect could be verified with further chamber experiments at higher relative humidity.

In summary of these results, it is plausible that these mechanisms are occurring in a variety of different locations. As long as NH_3 and HNO_3 gas phase concentrations and nucleation are high enough, and there is a sufficient pre-existing particle distribution, small perturbations in the steady state could result in increasing the number concentrations of CCN particles, and thus sustaining pollution and haze. It is possible that such phenomena have not been observed due to factors such as location and time or diameter resolution. In order to attempt to resolve whether this growth does effect urban particle size distributions, ambient measurements of particle distributions close to point sources of ammonia and nitric acid, as well as higher time resolution gas phase concentrations, and particle compositions are needed.

We provide experimental results at -10°C, showing that temperature has a great effect on growth via ammonium nitrate formation. Our model is in good agreement with the CLOUD measurements, and shows the same temperature dependence. We furthermore present two types of inhomogeneity expected in urban areas, temperature and concentrations. We remark that short deviations that result in supersaturation can aid survival of small particles by growing them to larger sizes, and even once the steady state is resumed, the particle size distribution is substantially different. This further supports the conclusions from Wang *et al.* [126] and Marten *et al.* [136] that growth via ammonium nitrate is an important mechanism for aerosol growth and survival in polluted conditions, and may be partially responsible for sustaining high particle numbers in haze conditions [126].

4.6 Supplementary information

4.6.1 Summary

This supplementary information (SI) section describes the changes to the model for use at -10°C, the ambient measurements of ammonia used for constraining inhomogeneous time-series, as well as presenting figures of the particle composition and model results with the resolution of a long scanning mobility particle sizer (lSMPS).

4.6.2 Model at -10°C

4.6.2.1 Kelvin diameter

The Kelvin diameter for ammonium nitrate at -10 °C was calculated by fitting the data from CLOUD experiments to Equation (4.1), in the same method as for 5°C as shown in [136].

$$S_{AB,p} = 10^{\left(d_{K10}/d_{act}\right)} \tag{4.1}$$

For the experiments with a temperature change, an average Kelvin diameter of the measurements at -10°C and 5°C was used for all temperatures.

4.6.2.2 Growth rates – N_2O_5

The three experiments indicated in Figure 4.1 of the main paper had significantly higher growth rates than modelled rates, as shown in Figure 4.4. We used the Atchem online solver with inputs from the Master Chemical Mechanism (MCM, [134], [135]) for reaction rates, and measured concentrations, photolysis rates, and loss rates from the CLOUD chamber to model the N_2O_5 concentration in the chamber. Since these experiments are at -10°C we expect uptake of N_2O_5 to be fast, and therefore for simplicity we treated the N_2O_5 as additional HNO_3. For Figure 4.1 we used the minimum predicted N_2O_5 concentration from the model output and so the modelled points are a low estimate.
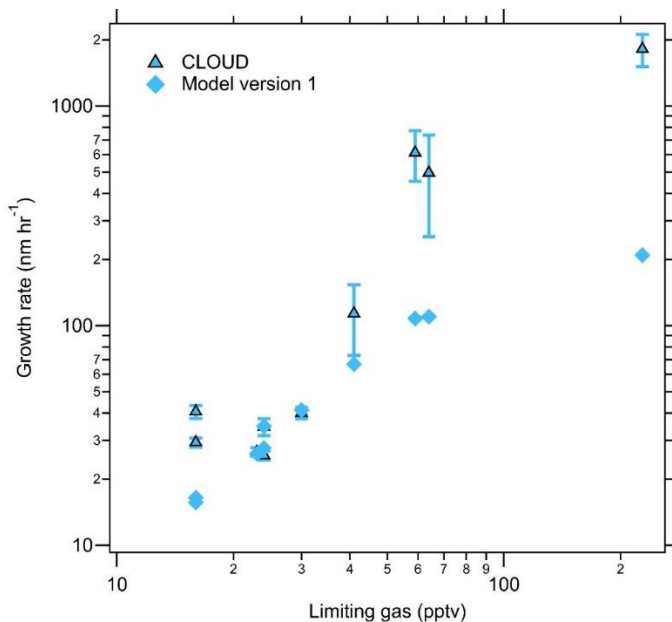
Figure 4.4: Growth rates using input of HNO₃ as the limiting gas. All of the -10°C runs were limited by HNO₃, these modelled growth rates are calculated using only the measured HNO₃ concentration, whereas for the model results presented in Figure 4.1 of the main paper the concentration of N_2O_5 was added to the HNO₃ concentration for the model constraints. Including the N_2O_5 concentrations in the model brought the model and measured growth rates closer together, and also shifted the points right on the x-axis since the gas concentration was increased.

4.6.3   Constraining NH₃ time-series

For generating Figure 4.3 of the main text, we needed to choose what magnitude and length ammonia concentration inhomogeneities we will constrain to the model. We analysed time-series from two campaigns, the first was a mobile campaign in Zurich (Switzerland) in October 2013, the second a mobile and stationary campaign in Tallinn and Tarttu (Estonia) March – April 2014.[26] For background NH₃ concentrations, we took the average over background stationary measurements in Estonia, which ranged from 1-6 ppbv. Since the HOA time-series from this study was considered to be the best traffic tracer, we looked to the HOA time-series for inhomogeneities. We used the average emission ratio of NH₃ to the HOA factor from [26] to

convert the variability in the HOA time-series to NH$_3$ concentrations. We identified two different "spike" variations in the HOA time-series. The first being smaller more frequent spikes, roughly every 5 minutes corresponding to an increase in NH$_3$ of 1-2 ppbv. The second set of inhomogeneities were larger deviations from the time-series, increasing to a NH$_3$ equivalence of 10-20 ppbv less frequently, usually every 20-30 minutes.

4.6.4   Sensitivity tests

We performed sensitivity tests of the impact of nucleation rates and temperature on the condensation of NH$_4$NO$_3$. Figure 4.5a) shows a repeat of the model shown in Figure 4.2c) with a temperature range of 15°C to 0°C and temperature dependent nucleation rates typical of 1×10^7 H$_2$SO$_4$ with 3ppb NH$_3$ and no amines.[10], [12], [121] The activation is noticeably weaker as there are not enough particles above the activation diameter. In contrast Figure 4.5b) shows the same conditions with the change in temperature shifted to a later time in the model, resulting in more particles present and a stronger activation event. This tells us that the main impact the nucleation rate will have on NH$_4$NO$_3$ formation is that it affects what the particle distribution is when the supersaturation occurs. Figure 4.5 c) shows a repeat of b) with the temperature range increased to 20°C to 0°C. These particles activate to even higher sizes, although it takes longer.
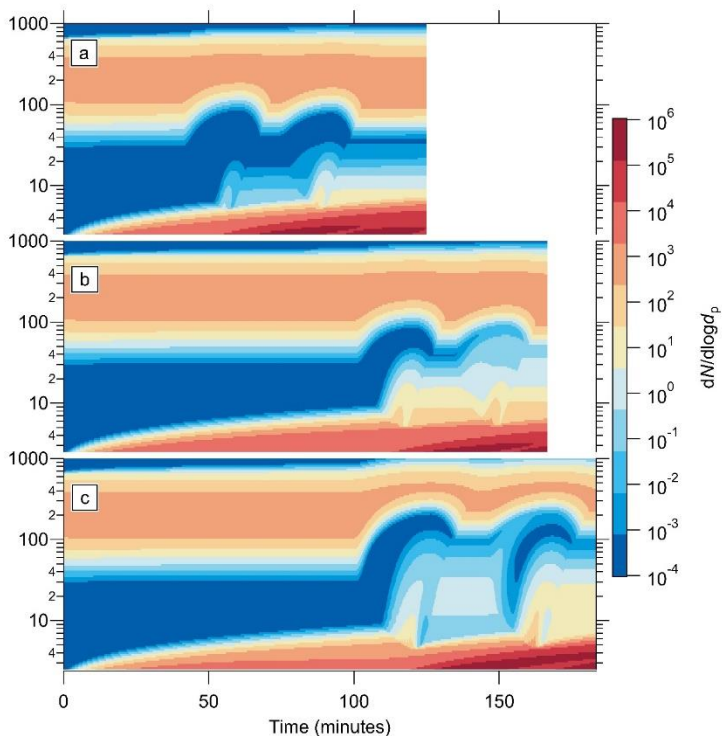
Figure 4.5: Nucleation rate and temperature sensitivity tests. a) Repeat of model presented in Figure 4.2c) with lower nucleation rates, and temperature change from 15°C to 0°C **b)** Repeat of a) but with temperature change delayed to a later time. **c)** Repeat of b) with a temperature change from 20°C to 0°C

4.6.5 Particle composition

Figure 4.6 presents two size distributions of the fraction of NH_4NO_3 in the particles from model results presented in the main paper. Figure 4.6a) is the results from Figure 4.2a) and Figure 4.6b) is the same output from Figure 4.3b). The simulated condensation sink starts with 10% NH_4NO_3 and the inputs of NH_3 and HNO_3 are saturated at 200 nm (i.e. 200 nm is the activation diameter), so before inhomogeneities are introduced there is some evaporation below 200 nm and condensation above 200 nm as the model equilibrates. We observe that the fraction of NH_4NO_3 is only significant during the supersaturated periods and above the activation diameter,

ammonium nitrate starts to evaporate once the saturation drops below one. However, Figure 4.2 and Figure 4.3 of the main text show that the particles continue to survive at higher sizes than before activation as ammonium sulfate can now condense more readily onto the rapidly grown, relatively stable, larger particles.
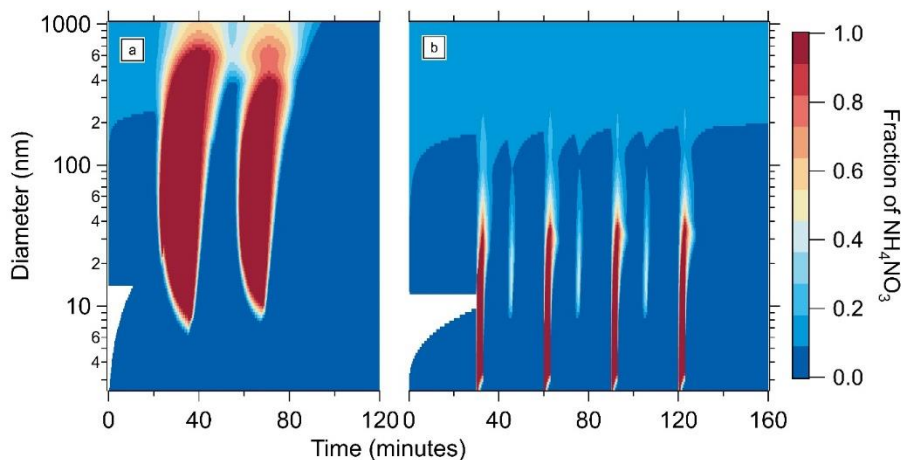
Figure 4.6: Number fraction of NH₄NO₃ from Figure 4.2 and Figure 4.3 as a function of time. Number fraction is defined as the number concentration ratio (molecules cm⁻³ / molecules cm⁻³) **a)** Model results from Figure 4.2a) (temperature change due to vertical transport). **b)** Model results from Figure 4.3b) (inhomogeneities due to spikes of NH₃). The white colour represents absence of particles.

4.6.6 Time resolution

Figure 4.7 presents output from the model simulation presented in Figure 4.3b) with the time and diameter resolution of a long SMPS (5 minutes, 89 logarithmically spaced size bins 20-480 nm). This is meant to represent the fact that such phenomena may not be easily recognised when measuring particle size distributions in ambient environments. In this instance the inhomogeneities lasted only 2-3 minutes, which an instrument with a 5 minute resolution may not detect. Figure 4.7 has much less distinct features than Figure 4.3b), and those that are visible may easily be interpreted as noise. Furthermore since the lSMPS starts at 20 nm we miss the first and largest jump in particle size, which at high supersaturations could be as low as a few

nanometers. As discussed in the main text, how these phenomena look will also depend on the pre-existing particle size distributions.
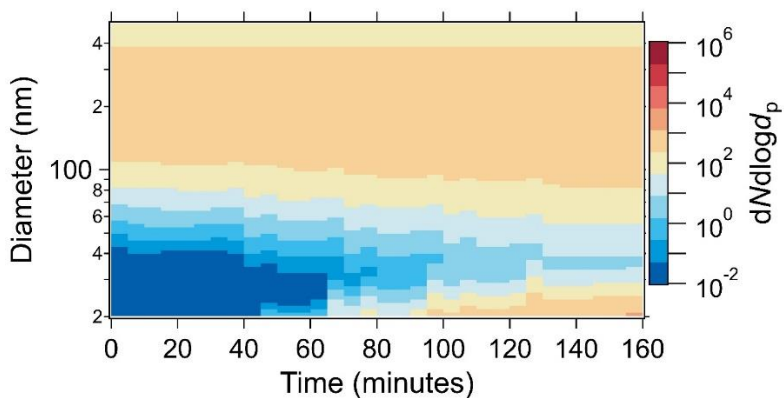

Figure 4.7: Low-resolution replication of Figure 4.3b) from the main text. The size distribution from the model output presented in Figure 4.3b) was interpolated to the size bins of the long SMPS and 5 minute time resolution. This illustrates that inhomogeneities may not be as noticeable in ambient measurements.

5 Conclusions

The assessment of the impacts of aerosols on the climate system and air quality is still plagued by large uncertainties; difficulties in predicting and quantifying ambient new particle formation in megacities are rooted in a lack of knowledge about the formation and growth mechanisms.

This thesis presents a newly discovered mechanism for growth of small particles by formation of ammonium nitrate. It was found that in supersaturation conditions of HNO_3 and NH_3, extremely high growth rates can affect particles as small as a few nanometers. This mechanism has a strong temperature dependence, consistent with the calculated uptake of NH_3 and HNO_3, which is limited by the formation of ammonium nitrate. Ammonium nitrate formation grows particles in a process consistent with the nano-Köhler theory. Accordingly, there is an activation diameter for a given product of NH_3 and HNO_3 gas phase concentrations. Above this activation diameter, ammonium nitrate can form and grow particles extremely rapidly, and so in supersaturation conditions, very small particles can grow to large sizes. Furthermore, at −25 °C pure ammonium nitrate could even nucleate at rates of several 100 particles cm^{-3} per hour in the absence of other nucleating vapours, such as sulfuric acid. However, this new mechanism of rapid growth requires relatively high concentrations of NH_3 and HNO_3. Although such concentrations are typical of an urban environment, there is also likely to be high particle number concentrations that could limit the impact of ammonium nitrate activation by scavenging small particles before they can grow.

The formation of ammonium nitrate could be a missing growth pathway that explains the higher than expected survival of new particles in polluted environments. We have examined this hypothesis experimentally, by varying the concentrations of NH_3 and HNO_3, as well as the particle condensation sink, at 5°C. Furthermore, a kinetic model was developed which is capable of replicating the experimental results. We showed that the high growth rates are sufficient to grow freshly nucleated particles even in the presence of a high condensation sink, similar to those measured during haze events. Model and experimental results were used to illustrate that survival of particles between 2.5 nm and 6 nm is drastically increased in the presence of high

concentrations of gas phase ammonia and nitric acid. We presented for the first time an explanation for high particle survival during haze conditions supported by quantitative model simulations.

Since this mechanism of rapid growth requires supersaturation of NH_3 and HNO_3, and ambient environments tend towards equilibrium, the final chapter of this thesis presented further model and experimental results at −10°C, aiming to showcase various atmospheric conditions where one could expect to observe activation and high growth rates. Using the kinetic model, we show that where there is a perturbation of equilibrium conditions, such as an increase in ammonia concentration due to local emissions from vehicular sources, or a change in temperature during vertical transport, formation of ammonium nitrate can grow particles sufficiently rapidly to escape the valley of death and continue to grow even after equilibrium conditions resume. This can only occur, however, when particles are present which are larger than the activation diameter, therefore high nucleation and early growth rates are also required. The inhomogeneities presented are based on ambient measurements and are considered to be typical of urban environments. In conclusion of this chapter, in inhomogeneous conditions that are typical in urban areas it is plausible that ammonium nitrate formation can have a significant impact on the particle size distribution in urban environments.

This thesis presents three reports on the effect of ammonium nitrate formation on urban aerosols. All of the results presented support one another in the conclusion that the previously undiscovered mechanism of ammonium nitrate driven grown is of great interest to understanding the puzzle of urban aerosols.

6 Outlook

Alongside these discoveries on the effect of NH_3 and HNO_3 on urban aerosols, a fourth report has been published presenting further results of synergistic nucleation with NH_3 HNO_3 and H_2SO_4 in upper tropospheric conditions (Wang *et al*. (2022), [137]). The results show that ammonium sulfate nucleation rates increase orders of magnitude in the presence of HNO_3, and that ammonium nitrate formation can grow these newly formed particles rapidly to high sizes. From model simulations, it is confirmed that in conditions of an Asian monsoon these processes can produce CCN which can spread across the mid-latitude northern hemisphere via transport. These results highlight the importance of ammonium nitrate formation for the upper tropospheric particle budget. However, these experiments only cover a small range of ambient relevant conditions. Further experiments are needed to explore the immense phase space of the upper troposphere, and determine the dependence of particle formation rates on vapour concentrations, temperature, and high ionization levels. Furthermore, it is vitally important to improve measurements of nucleating vapours and clusters in the upper troposphere and aim to understand their sources and sinks. Key points of interest are the formation rates of HNO_3, and transport of NH_3 into the upper troposphere, especially given that NH_3 wet scavenging is strongly dependent on cloud acidity and phase state.

Ambient measurements in urban areas are abundant, however there are many factors contributing to aerosol properties, and it can often be hard to distinguish between different variables. Therefore we look to chamber and laboratory measurements to help us to deconvolve the complexities of urban air. Since we have identified a new mechanism, the next logical step is therefore to verify that these processes do occur in ambient environments. Growth by NH_4NO_3 formation requires gas phase NH_3 and HNO_3 to be in supersaturated conditions, whereas generally supersaturation conditions do not last for a long time as the system will tend towards equilibrium. In order to understand the impact ammonium nitrate formation has on urban aerosols, we need to understand how gas phase HNO_3 and NH_3 behave in an urban environment. The key gas here is NH_3 since it is directly emitted by a multitude of sources, whereas HNO_3 is mostly formed by photolysis of NO_2, and therefore the concentration time-series is more

smoothed, and less likely to force the system out of equilibrium. Despite this, it is also important to measure nitric acid time-series as this is not currently a typical tracer in ambient measurements. In recent history, NO_X concentrations have increased in many urban areas, and SO_2 has decreased. This information, coupled with the newly presented growth mechanism of ammonia and nitric acid, should be enough motivation to implement nitric acid monitoring into ambient measurements. Key sources of ammonia are agriculture and traffic. According to Elser et al. [26], in the three European cities investigated, traffic significantly enhances the ammonia concentrations in urban environments. Agriculture sources are usually not within a city, and therefore contribute more to the background concentrations than to inhomogeneities. Emissions from traffic will be dependent on the type of fuel and vehicles present. Further investigation into constraining sources of ammonia in urban environments would allow for a high-resolution model of a city to constrain sources and variations in order to elucidate the impact of ammonium nitrate growth. This will also be important for constraining particle formation from sulfuric acid, given the quadratic dependence of formation rates on ammonia concentrations.

The impact of the phase state of the aerosols on the formation of NH_4NO_3 could also be an important relationship to understand. Above the deliquescence relative humidity (DRH) NH_4NO_3 will be in the liquid phase, and the relative humidity as well as the ionic strength will affect the dissociation constant K_p [1], [138]. Furthermore, for particles to be wet, they need to be large enough that water can condense on them, so the particles likely to be affected by the changing phase state are larger particles at high relative humidity. Understanding the effect of RH is crucial in order to understand how NH_4NO_3 affects ambient aerosols, and so further chamber experiments should be conducted under different relative humidity conditions to elucidate the effect of the phase state on the mechanism of NH_4NO_3 formation.

While most of the results we have discussed in this thesis are related to daytime conditions, N_2O_5, formed by NO_X, can also be an important contributing factor to aerosol growth during night time. We have shown that at -10°C N_2O_5 uptake is enhancing growth rates. N_2O_5 mixing ratios have been measured ranging from hundreds of pptv to a few ppbv in different urban

regions [1]. This makes N_2O_5 another interesting species to study. Combining the two processes of N_2O_5 uptake and ammonium nitrate growth, it is clear that a lot of growth of urban aerosols may be driven by NO_X. There are already many policies in place aimed at reducing NO_X concentrations in cities across the globe, for reasons other than contribution to aerosol growth. In light of these new findings, and including the fact that NO_X concentrations have been increasing, it should be clear that it is even more critical to aim to reduce NO_X emissions, especially in densely populated urban areas where particle concentrations can have a negative impact on health.

Other studies have also shown that organic acid contribution to aerosol growth can correlate with measured ammonium in particles, suggesting that these acids may be involved in mechanisms similar to ammonium nitrate formation [139]–[141]. The authors of [139] suggest that the major impact of this inclusion is altering the chemical compositions of aerosols, and thus physical properties, rather than the impact on growth rates. In either case, in order to solve the complex puzzle of urban aerosols, understanding the possibility of other growth mechanisms by formation of ammonium salts should be of great interest. There are currently many policies in place aimed at decreasing ammonia in urban areas. The results discussed show that formation of ammonium salts can affect the particle size distribution in a variety of ways; therefore, a significant reduction in gas-phase ammonia would certainly affect these mechanisms and subsequently aerosols in polluted areas.

List of figures

List of tables

References

[1]   J. Seinfeld H. and S. Pandis N., *Atmospheric Chemistry and Physics*, vol. 2nd edn. John Wiley & Sons, 2006.

[2]   R. Jaenicke, "Chapter 1 Tropospheric Aerosols," in *International Geophysics*, vol. 54, Elsevier, 1993, pp. 1–31. doi: 10.1016/S0074-6142(08)60210-7.

[3]   T. F. Stocker *et al.*, "Intergovernmental Panel on Climate Change (IPCC).," *Climate Change 2013: The Physical Science Basis*, Cambridge Univ. Press 2013.

[4]   P. H. Hoet, I. Brüske-Hohlfeld, and O. V. Salata, "Nanoparticles – known and unknown health risks," *J Nanobiotechnol*, vol. 2, no. 1, p. 12, 2004, doi: 10.1186/1477-3155-2-12.

[5]   N. Künzli, L. Perez, and R. Rapp, "Air Quality and Health." European Respiratory Society, 2010.

[6]   F. J. Kelly and J. C. Fussell, "Air pollution and airway disease: Air pollution and airway disease," *Clinical & Experimental Allergy*, vol. 41, no. 8, pp. 1059–1071, Aug. 2011, doi: 10.1111/j.1365-2222.2011.03776.x.

[7]   WHO, "WHO methods and data sources for country-level causes of death 2000-2019." World Health Organisation, 2014.

[8]   WHO, "WHO methods and data sources for global burden of disease estimates 2000-2019." World Health Organisation, 2014.

[9]   D. W. Dockery *et al.*, "An Association between Air Pollution and Mortality in Six U.S. Cities," *New England Journal of Medicine*, vol. 329, 1993, doi: doi:10.1056/NEJM199312093292401.

[10]   H. Gordon *et al.*, "Causes and importance of new particle formation in the present-day and preindustrial atmospheres: CAUSES AND ROLE OF NEW PARTICLE FORMATION," *J. Geophys. Res. Atmos.*, vol. 122, no. 16, pp. 8739–8760, Aug. 2017, doi: 10.1002/2017JD026844.

[11]   R. Cai *et al.*, "Aerosol surface area concentration: a governing factor in new particle formation in Beijing," *Atmos. Chem. Phys.*, vol. 17, no. 20, pp. 12327–12340, Oct. 2017, doi: 10.5194/acp-17-12327-2017.

[12]   M. Xiao *et al.*, "The driving factors of new particle formation and growth in the polluted boundary layer," *Atmos. Chem. Phys.*, vol. 21, no. 18, pp. 14275–14291, Sep. 2021, doi: 10.5194/acp-21-14275-2021.

[13]   X.-C. He *et al.*, "Role of iodine oxoacids in atmospheric aerosol nucleation," *Science*, vol. 371, no. 6529, pp. 589–595, Feb. 2021, doi: 10.1126/science.abe0298.

[14]   A. Baccarini *et al.*, "Frequent new particle formation over the high Arctic pack ice by enhanced iodine emissions," *Nat Commun*, vol. 11, no. 1, p. 4924, Dec. 2020, doi: 10.1038/s41467-020-18551-0.

[15]   C. Yan *et al.*, "The Synergistic Role of Sulfuric Acid, Bases, and Oxidized Organics Governing New-Particle Formation in Beijing," *Geophys Res Lett*, vol. 48, no. 7, Apr. 2021, doi: 10.1029/2020GL091944.

[16] L. Yao *et al.*, "Atmospheric new particle formation from sulfuric acid and amines in a Chinese megacity," *Science*, vol. 361, no. 6399, pp. 278–281, Jul. 2018, doi: 10.1126/science.aao4839.

[17] R. Jayaratne *et al.*, "Observations of particles at their formation sizes in Beijing, China," *Atmos. Chem. Phys.*, vol. 17, no. 14, pp. 8825–8835, Jul. 2017, doi: 10.5194/acp-17-8825-2017.

[18] C. Carnerero *et al.*, "Vertical and horizontal distribution of regional new particle formation events in Madrid," *Atmos. Chem. Phys.*, vol. 18, no. 22, pp. 16601–16618, Nov. 2018, doi: 10.5194/acp-18-16601-2018.

[19] J. Kontkanen *et al.*, "Measurements of sub-3 nm particles using a particle size magnifier in different environments: from clean mountain top to polluted megacities," *Atmos. Chem. Phys.*, vol. 17, no. 3, pp. 2163–2187, Feb. 2017, doi: 10.5194/acp-17-2163-2017.

[20] H. Yu *et al.*, "Nucleation and growth of sub-3 nm particles in the polluted urban atmosphere of a megacity in China," *Atmos. Chem. Phys.*, vol. 16, no. 4, pp. 2641–2657, Mar. 2016, doi: 10.5194/acp-16-2641-2016.

[21] L. Dai *et al.*, "Regional and local new particle formation events observed in the Yangtze River Delta region, China," *J. Geophys. Res. Atmos.*, vol. 122, no. 4, pp. 2389–2402, Feb. 2017, doi: 10.1002/2016JD026030.

[22] C. Kuang, P. H. McMurry, A. V. McCormick, and F. L. Eisele, "Dependence of nucleation rates on sulfuric acid vapor concentration in diverse atmospheric locations," *J. Geophys. Res.*, vol. 113, no. D10, p. D10209, May 2008, doi: 10.1029/2007JD009253.

[23] M. Kulmala, V.-M. Kerminen, T. Petäjä, A. J. Ding, and L. Wang, "Atmospheric gas-to-particle conversion: why NPF events are observed in megacities?," *Faraday Discuss.*, vol. 200, pp. 271–288, 2017, doi: 10.1039/C6FD00257A.

[24] Y. Chang *et al.*, "Assessing Contributions of Agricultural and Nonagricultural Emissions to Atmospheric Ammonia in a Chinese Megacity," *Environ. Sci. Technol.*, vol. 53, no. 4, pp. 1822–1833, Feb. 2019, doi: 10.1021/acs.est.8b05984.

[25] Y. Chang *et al.*, "The importance of vehicle emissions as a source of atmospheric ammonia in the megacity of Shanghai," *Atmos. Chem. Phys.*, vol. 16, no. 5, pp. 3577–3594, Mar. 2016, doi: 10.5194/acp-16-3577-2016.

[26] M. Elser *et al.*, "High contributions of vehicular emissions to ammonia in three European cities derived from mobile measurements," *Atmospheric Environment*, vol. 175, pp. 210–220, Feb. 2018, doi: 10.1016/j.atmosenv.2017.11.030.

[27] Q. Zhang *et al.*, "Understanding atmospheric organic aerosols via factor analysis of aerosol mass spectrometry: a review," *Anal Bioanal Chem*, vol. 401, no. 10, pp. 3045–3067, Dec. 2011, doi: 10.1007/s00216-011-5355-y.

[28] A. C. Aiken *et al.*, "Mexico City aerosol analysis during MILAGRO using high resolution aerosol mass spectrometry at the urban supersite (T0) – Part 1: Fine particle composition and organic source apportionment," *Atmos. Chem. Phys.*, p. 21, 2009.

[29] J. L. Jimenez *et al.*, "Evolution of Organic Aerosols in the Atmosphere," *Science*, vol. 326, no. 5959, pp. 1525–1529, Dec. 2009, doi: 10.1126/science.1180353.

[30] X. Fu *et al.*, "Persistent Heavy Winter Nitrate Pollution Driven by Increased Photochemical Oxidants in Northern China," *Environ. Sci. Technol.*, vol. 54, no. 7, pp. 3881–3889, Apr. 2020, doi: 10.1021/acs.est.9b07248.

[31] H. Kim, Q. Zhang, and Y. Sun, "Measurement report: Characterization of severe spring haze episodes and influences of long-range transport in the Seoul metropolitan area in March 2019," Aerosols/Field Measurements/Troposphere/Chemistry (chemical composition and reactions), preprint, Jun. 2020. doi: 10.5194/acp-2020-382.

[32] S. Guo *et al.*, "Elucidating severe urban haze formation in China," *Proc Natl Acad Sci USA*, vol. 111, no. 49, pp. 17373–17378, Dec. 2014, doi: 10.1073/pnas.1419604111.

[33] H. Kim, Q. Zhang, G.-N. Bae, J. Y. Kim, and S. B. Lee, "Sources and atmospheric processing of winter aerosols in Seoul, Korea: insights from real-time measurements using a high-resolution aerosol mass spectrometer," *Atmos. Chem. Phys.*, vol. 17, no. 3, pp. 2009–2033, Feb. 2017, doi: 10.5194/acp-17-2009-2017.

[34] L. T. Molina *et al.*, "An overview of the MILAGRO 2006 Campaign: Mexico City emissions and their transport and transformation," *Atmos. Chem. Phys.*, vol. 10, no. 18, pp. 8697–8760, Sep. 2010, doi: 10.5194/acp-10-8697-2010.

[35] M. Kulmala *et al.*, "Is reducing new particle formation a plausible solution to mitigate particulate air pollution in Beijing and other Chinese megacities?," *Faraday Discuss.*, vol. 226, pp. 334–347, 2021, doi: 10.1039/D0FD00078G.

[36] M. Mozurkewich, "The dissociation constant of ammonium nitrate and its dependence on temperature, relative humidity and particle size," *Atmospheric Environment. Part A. General Topics*, vol. 27, no. 2, pp. 261–270, Feb. 1993, doi: 10.1016/0960-1686(93)90356-4.

[37] J. L. Jimenez, "Ambient aerosol sampling using the Aerodyne Aerosol Mass Spectrometer," *J. Geophys. Res.*, vol. 108, no. D7, p. 8425, 2003, doi: 10.1029/2001JD001213.

[38] W. Xu, Q. Wu, X. Liu, A. Tang, A. J. Dore, and M. R. Heal, "Characteristics of ammonia, acid gases, and PM2.5 for three typical land-use types in the North China Plain," *Environ Sci Pollut Res*, vol. 23, no. 2, pp. 1158–1172, Jan. 2016, doi: 10.1007/s11356-015-5648-3.

[39] L. Xu, S. Suresh, H. Guo, R. J. Weber, and N. L. Ng, "Aerosol characterization over the southeastern United States using high-resolution aerosol mass spectrometry: spatial and seasonal variation of aerosol composition and sources with a focus on organic nitrates," *Atmos. Chem. Phys.*, vol. 15, no. 13, pp. 7307–7336, Jul. 2015, doi: 10.5194/acp-15-7307-2015.

[40] D. K. Farmer *et al.*, "Response of an aerosol mass spectrometer to organonitrates and organosulfates and implications for atmospheric chemistry," *Proceedings of the National Academy of Sciences*, vol. 107, no. 15, pp. 6670–6675, Apr. 2010, doi: 10.1073/pnas.0912340107.

[41] J. Almeida *et al.*, "Molecular understanding of sulphuric acid–amine particle nucleation in the atmosphere," *Nature*, vol. 502, no. 7471, pp. 359–363, Oct. 2013, doi: 10.1038/nature12663.

[42] E. Canaval *et al.*, "Rapid conversion of isoprene photooxidation products in terrestrial plants," *Commun Earth Environ*, vol. 1, no. 1, p. 44, Dec. 2020, doi: 10.1038/s43247-020-00041-2.

[43] M. Breitenlechner, L. Fischer, M. Hainer, M. Heinritzi, J. Curtius, and A. Hansel, "PTR3: An Instrument for Studying the Lifecycle of Reactive Organic Carbon in the Atmosphere," *Anal. Chem.*, vol. 89, no. 11, pp. 5824–5831, Jun. 2017, doi: 10.1021/acs.analchem.6b05110.

[44] A. Kürten, L. Rondo, S. Ehrhart, and J. Curtius, "Performance of a corona ion source for measurement of sulfuric acid by chemical ionization mass spectrometry," *Atmos. Meas. Tech.*, vol. 4, no. 3, pp. 437–443, Mar. 2011, doi: 10.5194/amt-4-437-2011.

[45] J. Pfeifer *et al.*, "Measurement of ammonia, amines and iodine compounds using protonated water cluster chemical ionization mass spectrometry," *Atmos. Meas. Tech.*, vol. 13, no. 5, pp. 2501–2522, May 2020, doi: 10.5194/amt-13-2501-2020.

[46] J. Vanhanen *et al.*, "Particle Size Magnifier for Nano-CN Detection," *Aerosol Science and Technology*, vol. 45, no. 4, pp. 533–542, Mar. 2011, doi: 10.1080/02786826.2010.547889.

[47] D. Stolzenburg, G. Steiner, and P. M. Winkler, "A DMA-train for precision measurement of sub-10 nm aerosol dynamics," *Atmos. Meas. Tech.*, vol. 10, no. 4, pp. 1639–1651, May 2017, doi: 10.5194/amt-10-1639-2017.

[48] W. Kong *et al.*, "The nano-scanning electrical mobility spectrometer (nSEMS) and itsapplication to size distribution measurements of 1.5–25 nm particles," Aerosols/Laboratory Measurement/Instruments and Platforms, preprint, Mar. 2021. doi: 10.5194/amt-2021-62.

[49] C. O. Stanier, A. Y. Khlystov, and S. N. Pandis, "Nucleation Events During the Pittsburgh Air Quality Study: Description and Relation to Key Meteorological, Gas Phase, and Aerosol Parameters Special Issue of *Aerosol Science and Technology* on Findings from the Fine Particulate Matter Supersites Program," *Aerosol Science and Technology*, vol. 38, no. sup1, pp. 253–264, Dec. 2004, doi: 10.1080/02786820390229570.

[50] M. Höpfner *et al.*, "Ammonium nitrate particles formed in upper troposphere from ground ammonia sources during Asian monsoons," *Nat. Geosci.*, vol. 12, no. 8, pp. 608–612, Aug. 2019, doi: 10.1038/s41561-019-0385-8.

[51] C. J. Williamson *et al.*, "A large source of cloud condensation nuclei from new particle formation in the tropics," *Nature*, vol. 574, no. 7778, pp. 399–403, Oct. 2019, doi: 10.1038/s41586-019-1638-9.

[52] P. H. McMurry, "A criterion for new particle formation in the sulfur-rich Atlanta atmosphere," *J. Geophys. Res. D*, vol. 100, no. D22S02, 2005.

[53] M. Kulmala *et al.*, "Direct Observations of Atmospheric Aerosol Nucleation," *Science*, vol. 339, no. 6122, pp. 943–946, Feb. 2013, doi: 10.1126/science.1227385.

[54] I. Riipinen *et al.*, "The contribution of organics to atmospheric nanoparticle growth," *Nature Geosci*, vol. 5, no. 7, pp. 453–458, Jul. 2012, doi: 10.1038/ngeo1499.

[55] J. R. Pierce and P. J. Adams, "Efficiency of cloud condensation nuclei formation from ultrafine particles," *Atmos. Chem. Phys.*, p. 13, 2007.

[56] C. Kuang, P. H. McMurry, and A. V. McCormick, "Determination of cloud condensation nuclei production from measured new particle formation events," *Geophys. Res. Lett.*, vol. 36, no. 9, p. L09822, May 2009, doi: 10.1029/2009GL037584.

[57] J. S. Apte, M. Brauer, A. J. Cohen, M. Ezzati, and C. A. Pope, "Ambient PM $_{2.5}$ Reduces Global and Regional Life Expectancy," *Environ. Sci. Technol. Lett.*, vol. 5, no. 9, pp. 546–551, Sep. 2018, doi: 10.1021/acs.estlett.8b00360.

[58] G. Chen, W.-C. Wang, and J.-P. Chen, "Circulation responses to regional aerosol climate forcing in summer over East Asia," *Clim Dyn*, vol. 51, no. 11–12, pp. 3973–3984, Dec. 2018, doi: 10.1007/s00382-018-4267-3.

[59] V.-M. Kerminen and M. Kulmala, "Analytical formulae connecting the 'real' and the 'apparent' nucleation rate and the nuclei number concentration for atmospheric nucleation events," *Journal of Aerosol Science*, vol. 33, no. 4, pp. 609–622, Apr. 2002, doi: 10.1016/S0021-8502(01)00194-X.

[60] S. Takahama, "Modeling the diurnal variation of nitrate during the Pittsburgh Air Quality Study," *J. Geophys. Res.*, vol. 109, no. D16, p. D16S06, 2004, doi: 10.1029/2003JD004149.

[61] W. Xu *et al.*, "Changes in Aerosol Chemistry From 2014 to 2016 in Winter in Beijing: Insights From High-Resolution Aerosol Mass Spectrometry," *J. Geophys. Res. Atmos.*, vol. 124, no. 2, pp. 1132–1147, Jan. 2019, doi: 10.1029/2018JD029245.

[62] P. H. McMurry, "Photochemical aerosol formation from SO2: A theoretical analysis of smog chamber data," *Journal of Colloid and Interface Science*, vol. 78, no. 2, pp. 513–527, Dec. 1980, doi: 10.1016/0021-9797(80)90589-5.

[63] J. Kirkby *et al.*, "Ion-induced nucleation of pure biogenic particles," *Nature*, vol. 533, no. 7604, pp. 521–526, May 2016, doi: 10.1038/nature17953.

[64] D. Stolzenburg *et al.*, "Rapid growth of organic aerosol nanoparticles over a wide tropospheric temperature range," *Proc Natl Acad Sci USA*, vol. 115, no. 37, pp. 9122–9127, Sep. 2018, doi: 10.1073/pnas.1807604115.

[65] C. D. O'Dowd *et al.*, "Marine aerosol formation from biogenic iodine emissions," *Nature*, vol. 417, no. 6889, pp. 632–636, Jun. 2002, doi: 10.1038/nature00775.

[66] J. Kirkby *et al.*, "Role of sulphuric acid, ammonia and galactic cosmic rays in atmospheric aerosol nucleation," *Nature*, vol. 476, no. 7361, pp. 429–433, Aug. 2011, doi: 10.1038/nature10343.

[67] J. Kontkanen, T. Olenius, M. Kulmala, and I. Riipinen, "Exploring the potential of nano-Köhler theory to describe the growth of atmospheric molecular clusters by organic vapors using cluster kinetics simulations," *Atmos. Chem. Phys.*, vol. 18, no. 18, pp. 13733–13754, Sep. 2018, doi: 10.5194/acp-18-13733-2018.

[68] K. Lu *et al.*, "Fast Photochemistry in Wintertime Haze: Consequences for Pollution Mitigation Strategies," *Environ. Sci. Technol.*, vol. 53, no. 18, pp. 10676–10684, Sep. 2019, doi: 10.1021/acs.est.9b02422.

[69] T. Yli-Juuti *et al.*, "Model for acid-base chemistry in nanoparticle growth (MABNAG)," *Atmos. Chem. Phys.*, vol. 13, no. 24, pp. 12507–12524, Dec. 2013, doi: 10.5194/acp-13-12507-2013.

[70] M. O. Letzel, C. Helmke, E. Ng, X. An, A. Lai, and S. Raasch, "LES case study on pedestrian level ventilation in two neighbourhoods in Hong Kong," *metz*, vol. 21, no. 6, pp. 575–589, Dec. 2012, doi: 10.1127/0941-2948/2012/0356.

[71] H. E. Manninen *et al.*, "EUCAARI ion spectrometer measurements at 12 European sites – analysis of new particle formation events," *Atmos. Chem. Phys.*, vol. 10, no. 16, pp. 7907–7927, Aug. 2010, doi: 10.5194/acp-10-7907-2010.

[72] J. R. Pierce *et al.*, "Quantification of the volatility of secondary organic compounds in ultrafine particles during nucleation events," *Atmos. Chem. Phys.*, vol. 11, no. 17, pp. 9019–9036, Sep. 2011, doi: 10.5194/acp-11-9019-2011.

[73] C. Ge, C. Zhu, J. S. Francisco, X. C. Zeng, and J. Wang, "A molecular perspective for global modeling of upper atmospheric NH_3 from freezing clouds," *Proc Natl Acad Sci USA*, vol. 115, no. 24, pp. 6147–6152, Jun. 2018, doi: 10.1073/pnas.1719949115.

[74] L. Liu *et al.*, "The role of nitric acid in atmospheric new particle formation," *Phys. Chem. Chem. Phys.*, vol. 20, no. 25, pp. 17406–17414, 2018, doi: 10.1039/C8CP02719F.

[75] J. Duplissy *et al.*, "Effect of ions on sulfuric acid-water binary particle formation: 2. Experimental data and comparison with QC-normalized classical nucleation theory: BINARY PARTICLE FORMATION EXPERIMENTS," *J. Geophys. Res. Atmos.*, vol. 121, no. 4, pp. 1752–1775, Feb. 2016, doi: 10.1002/2015JD023539.

[76] A. Dias *et al.*, "Temperature uniformity in the CERN CLOUD chamber," *Atmos. Meas. Tech.*, vol. 10, no. 12, pp. 5075–5088, Dec. 2017, doi: 10.5194/amt-10-5075-2017.

[77] R. Schnitzhofer *et al.*, "Characterisation of organic contaminants in the CLOUD chamber at CERN," *Atmos. Meas. Tech.*, vol. 7, no. 7, pp. 2159–2168, Jul. 2014, doi: 10.5194/amt-7-2159-2014.

[78] T. Jokinen *et al.*, "Atmospheric sulphuric acid and neutral cluster measurements using CI-APi-TOF," *Atmos. Chem. Phys.*, vol. 12, no. 9, pp. 4117–4125, May 2012, doi: 10.5194/acp-12-4117-2012.

[79] H. Junninen *et al.*, "A high-resolution mass spectrometer to measure atmospheric ion composition," *Atmos. Meas. Tech.*, vol. 3, no. 4, pp. 1039–1053, Aug. 2010, doi: 10.5194/amt-3-1039-2010.

[80] F. L. Eisele and D. J. Tanner, "Measurement of the gas phase concentration of H_2SO_4 and methane sulfonic acid and estimates of H_2SO_4 production and loss in the atmosphere," *J. Geophys. Res.*, vol. 98, no. D5, pp. 9001–9010, May 1993, doi: 10.1029/93JD00031.

[81] J. Tröstl *et al.*, "The role of low-volatility organic compounds in initial particle growth in the atmosphere," *Nature*, vol. 533, no. 7604, pp. 527–531, May 2016, doi: 10.1038/nature18271.

[82] M. Gautrois and R. Koppmann, "Diffusion technique for the production of gas standards for atmospheric measurements," *Journal of Chromatography A*, vol. 848, no. 1–2, pp. 239–249, Jul. 1999, doi: 10.1016/S0021-9673(99)00424-0.

[83] M. Wang *et al.*, "Reactions of Atmospheric Particulate Stabilized Criegee Intermediates Lead to High-Molecular-Weight Aerosol Components," *Environ. Sci. Technol.*, vol. 50, no. 11, pp. 5702–5710, Jun. 2016, doi: 10.1021/acs.est.6b02114.

[84] F. D. Lopez-Hilfiker *et al.*, "A novel method for online analysis of gas and particle composition: description and evaluation of a Filter Inlet for Gases and AEROsols (FIGAERO)," *Atmos. Meas. Tech.*, vol. 7, no. 4, pp. 983–1001, Apr. 2014, doi: 10.5194/amt-7-983-2014.

[85] W. Mui, H. Mai, A. J. Downard, J. H. Seinfeld, and R. C. Flagan, "Design, simulation, and characterization of a radial opposed migration ion and aerosol classifier (ROMIAC)," *Aerosol Science and Technology*, vol. 51, no. 7, pp. 801–823, Jul. 2017, doi: 10.1080/02786826.2017.1315046.

[86] D. Wimmer *et al.*, "Performance of diethylene glycol-based particle counters in the sub-3 nm size range," *Atmos. Meas. Tech.*, vol. 6, no. 7, pp. 1793–1804, Jul. 2013, doi: 10.5194/amt-6-1793-2013.

[87] H. Mai and R. C. Flagan, "Scanning DMA Data Analysis I. Classification Transfer Function," *Aerosol Science and Technology*, vol. 52, no. 12, pp. 1382–1399, Dec. 2018, doi: 10.1080/02786826.2018.1528005.

[88] H. Mai, W. Kong, J. H. Seinfeld, and R. C. Flagan, "Scanning DMA data analysis II. Integrated DMA-CPC instrument response and data inversion," *Aerosol Science and Technology*, vol. 52, no. 12, pp. 1400–1414, Dec. 2018, doi: 10.1080/02786826.2018.1528006.

[89] Z. Jurányi, M. Gysel, E. Weingartner, N. Bukowiecki, L. Kammermann, and U. Baltensperger, "A 17 month climatology of the cloud condensation nuclei number concentration at the high alpine site Jungfraujoch," *J. Geophys. Res.*, vol. 116, no. D10, p. D10204, May 2011, doi: 10.1029/2010JD015199.

[90] J. Tröstl *et al.*, "Fast and precise measurement in the sub-20nm size range using a Scanning Mobility Particle Sizer," *Journal of Aerosol Science*, vol. 87, pp. 75–87, Sep. 2015, doi: 10.1016/j.jaerosci.2015.04.001.

[91] A. Wiedensohler *et al.*, "Mobility particle size spectrometers: harmonization of technical standards and data structure to facilitate high quality long-term observations of atmospheric particle number size distributions," *Atmos. Meas. Tech.*, vol. 5, no. 3, pp. 657–685, Mar. 2012, doi: 10.5194/amt-5-657-2012.

[92] K. G. Denbigh, *The Principles of Chemical Equilibrium: With Applications in Chemistry and Chemical Eengineering*. Cambridge University Press, 1981.

[93] K. Lehtipalo *et al.*, "Multicomponent new particle formation from sulfuric acid, ammonia, and biogenic vapors," *Sci. Adv.*, vol. 4, no. 12, p. eaau5363, Dec. 2018, doi: 10.1126/sciadv.aau5363.

[94] S. L. Clegg and J. H. Seinfeld, "Thermodynamic Models of Aqueous Solutions Containing Inorganic Electrolytes and Dicarboxylic Acids at 298.15 K. 1. The Acids as Nondissociating Components," *J. Phys. Chem. A*, vol. 110, no. 17, pp. 5692–5717, May 2006, doi: 10.1021/jp056149k.

[95] S. L. Clegg and J. H. Seinfeld, "Thermodynamic Models of Aqueous Solutions Containing Inorganic Electrolytes and Dicarboxylic Acids at 298.15 K. 2. Systems Including Dissociation Equilibria," *J. Phys. Chem. A*, vol. 110, no. 17, pp. 5718–5734, May 2006, doi: 10.1021/jp056150j.

[96] S. Xiao *et al.*, "Strong atmospheric new particle formation in winter in urban Shanghai, China," *Atmos. Chem. Phys.*, vol. 15, no. 4, pp. 1769–1781, Feb. 2015, doi: 10.5194/acp-15-1769-2015.

[97] K. Iida, M. R. Stolzenburg, P. H. McMurry, and J. N. Smith, "Estimating nanoparticle growth rates from size-dependent charged fractions: Analysis of new particle formation events in Mexico City," *J. Geophys. Res. D Atmospheres*, vol. 113, no. D05207, 2008.

[98] G. Mordas, H. E. Manninen, T. Petäjä, P. P. Aalto, K. Hämeri, and M. Kulmala, "On Operation of the Ultra-Fine Water-Based CPC TSI 3786 and Comparison with Other TSI Models (TSI 3776, TSI 3772, TSI 3025, TSI 3010, TSI 3007)," *Aerosol Science and Technology*, vol. 42, no. 2, pp. 152–158, Jan. 2008, doi: 10.1080/02786820701846252.

[99] K. Lehtipalo *et al.*, "The effect of acid–base clustering and ions on the growth of atmospheric nano-particles," *Nat Commun*, vol. 7, no. 1, p. 11594, Sep. 2016, doi: 10.1038/ncomms11594.

[100] M. D. Maso *et al.*, "Aerosol size distribution measurements at four Nordic field stations: identification, analysis and trajectory analysis of new particle formation bursts," *Tellus B: Chemical and Physical Meteorology*, vol. 59, no. 3, pp. 350–361, Jan. 2007, doi: 10.1111/j.1600-0889.2007.00267.x.

[101] M. D. Maso *et al.*, "Formation and growth of fresh atmospheric aerosols: eight years of aerosol size distribution data from SMEAR II, Hyytiälä, Finland," vol. 10, p. 15.

[102] M. Komppula *et al.*, "Observations of new particle formation and size distributions at two different heights and surroundings in subarctic area in northern Finland: NEW PARTICLE FORMATION IN NORTHERN FINLAND," *J. Geophys. Res.*, vol. 108, no. D9, p. n/a-n/a, May 2003, doi: 10.1029/2002JD002939.

[103] H. Vehkamaki *et al.*, "Atmospheric particle formation events at Va¨rrio¨ measurement station in Finnish Lapland 1998–2002," *Atmos. Chem. Phys.*, p. 9, 2004.

[104] M. D. Maso *et al.*, "Aerosol particle formation events at two Siberian stations inside the boreal forest," vol. 13, p. 12.

[105] T. Hussein *et al.*, "Observation of regional new particle formation in the urban atmosphere," *Tellus B: Chemical and Physical Meteorology*, vol. 60, no. 4, pp. 509–521, Jan. 2008, doi: 10.1111/j.1600-0889.2008.00365.x.

[106] M. Pikridas *et al.*, "In situ formation and spatial variability of particle number concentration in a European megacity," *Atmos. Chem. Phys.*, vol. 15, no. 17, pp. 10219–10237, Sep. 2015, doi: 10.5194/acp-15-10219-2015.

[107] A. Hamed *et al.*, "Nucleation and growth of new particles in Po Valley, Italy," *Atmos. Chem. Phys.*, p. 22, 2007.

[108] S. M. L. Hama, R. L. Cordell, G. P. A. Kos, E. P. Weijers, and P. S. Monks, "Sub-micron particle number size distribution characteristics at two urban locations in Leicester," *Atmospheric Research*, vol. 194, pp. 1–16, Sep. 2017, doi: 10.1016/j.atmosres.2017.04.021.

[109] J. Gao, F. Chai, T. Wang, S. Wang, and W. Wang, "Particle number size distribution and new particle formation: New characteristics during the special pollution control period in Beijing," *Journal of Environmental Sciences*, vol. 24, no. 1, pp. 14–21, Jan. 2012, doi: 10.1016/S1001-0742(11)60725-0.

[110] Z. B. Wang *et al.*, "Characteristics of regional new particle formation in urban and regional background environments in the North China Plain," *Atmos. Chem. Phys.*, vol. 13, no. 24, pp. 12495–12506, Dec. 2013, doi: 10.5194/acp-13-12495-2013.

[111] D. Yue *et al.*, "Characteristics of aerosol size distributions and new particle formation in the summer in Beijing," *J. Geophys. Res.*, vol. 114, p. D00G12, Jul. 2009, doi: 10.1029/2008JD010894.

[112] Y. M. Zhang *et al.*, "Characterization of new particle and secondary aerosol formation during summertime in Beijing, China," *Tellus B: Chemical and Physical Meteorology*, vol. 63, no. 3, pp. 382–394, Jan. 2011, doi: 10.1111/j.1600-0889.2011.00533.x.

[113] H. Man *et al.*, "Comparison of Daytime and Nighttime New Particle Growth at the HKUST Supersite in Hong Kong," *Environ. Sci. Technol.*, vol. 49, no. 12, pp. 7170–7178, Jun. 2015, doi: 10.1021/acs.est.5b02143.

[114] J. An *et al.*, "Characteristics of new particle formation events in Nanjing, China: Effect of water-soluble ions," *Atmospheric Environment*, vol. 108, pp. 32–40, May 2015, doi: 10.1016/j.atmosenv.2015.01.038.

[115] E. Herrmann *et al.*, "Aerosols and nucleation in eastern China: first insights from the new SORPES-NJU station," *Atmos. Chem. Phys.*, vol. 14, no. 4, pp. 2169–2183, Feb. 2014, doi: 10.5194/acp-14-2169-2014.

[116] J. F. Peng *et al.*, "Submicron aerosols at thirteen diversified sites in China: size distribution, new particle formation and corresponding contribution to cloud condensation nuclei production," *Atmos. Chem. Phys.*, vol. 14, no. 18, pp. 10249–10265, Sep. 2014, doi: 10.5194/acp-14-10249-2014.

[117] V. P. Kanawade *et al.*, "Infrequent occurrence of new particle formation at a semi-rural location, Gadanki, in tropical Southern India," *Atmospheric Environment*, vol. 94, pp. 264–273, Sep. 2014, doi: 10.1016/j.atmosenv.2014.05.046.

[118] P. Monkkonen, I. K. Koponen, K. E. J. Lehtinen, K. Hameri, R. Uma, and M. Kulmala, "Measurements in a highly polluted Asian mega city: observations of aerosol number size distribution, modal parameters and nucleation events," *Atmos. Chem. Phys.*, p. 10, 2005.

[119] C. Kuang, I. Riipinen, S.-L. Sihto, M. Kulmala, A. V. McCormick, and P. H. McMurry, "An improved criterion for new particle formation in diverse atmospheric environments," *Atmos. Chem. Phys.*, vol. 10, no. 17, pp. 8469–8480, Sep. 2010, doi: 10.5194/acp-10-8469-2010.

[120] K. Iida, "Contribution of ion-induced nucleation to new particle formation: Methodology and its application to atmospheric observations in Boulder, Colorado," *J. Geophys. Res. D Atmospheres*, vol. 111, no. D23201, 2006.

[121] E. M. Dunne *et al.*, "Global atmospheric particle formation from CERN CLOUD measurements," *Science*, vol. 354, no. 6316, pp. 1119–1124, Dec. 2016, doi: 10.1126/science.aaf2649.

[122] J. Merikanto, D. V. Spracklen, G. W. Mann, S. J. Pickering, and K. S. Carslaw, "Impact of nucleation on global CCN," *Atmos. Chem. Phys.*, p. 16, 2009.

[123] U. Lohmann and J. Feichter, "Global indirect aerosol effects: a review," *Atmos. Chem. Phys.*, p. 23, 2005.

[124] D. Bousiotis, M. Dall'Osto, D. C. S. Beddows, F. D. Pope, and R. M. Harrison, "Analysis of new particle formation (NPF) events at nearby rural, urban background and urban roadside sites," *Atmos. Chem. Phys.*, vol. 19, no. 8, pp. 5679–5694, Apr. 2019, doi: 10.5194/acp-19-5679-2019.

[125] Z. Wang *et al.*, "New particle formation in China: Current knowledge and further directions," *Science of The Total Environment*, vol. 577, pp. 258–266, Jan. 2017, doi: 10.1016/j.scitotenv.2016.10.177.

[126] M. Wang *et al.*, "Rapid growth of new atmospheric particles by nitric acid and ammonia condensation," *Nature*, vol. 581, no. 7807, pp. 184–189, 2020, doi: 10.1038/s41586-020-2270-4.

[127] D. Stolzenburg *et al.*, "Enhanced growth rate of atmospheric particles from sulfuric acid," *Atmos. Chem. Phys.*, vol. 20, no. 12, pp. 7359–7372, Jun. 2020, doi: 10.5194/acp-20-7359-2020.

[128] L. Pichelstorfer *et al.*, "Resolving nanoparticle growth mechanisms from size- and time-dependent growth rate analysis," *Atmos. Chem. Phys.*, vol. 18, no. 2, pp. 1307–1323, Jan. 2018, doi: 10.5194/acp-18-1307-2018.

[129] M. Ozon, D. Stolzenburg, L. Dada, A. Seppänen, and K. E. J. Lehtinen, "Aerosol formation and growth rates from chamber experiments using Kalman smoothing," *Atmos. Chem. Phys.*, vol. 21, no. 16, pp. 12595–12611, Aug. 2021, doi: 10.5194/acp-21-12595-2021.

[130] J. Voigtländer, J. Duplissy, L. Rondo, A. Kürten, and F. Stratmann, "Numerical simulations of mixing conditions and aerosol dynamics in the CERN CLOUD chamber," *Atmos. Chem. Phys.*, vol. 12, no. 4, pp. 2205–2214, Feb. 2012, doi: 10.5194/acp-12-2205-2012.

[131] R. Cai *et al.*, "Data inversion methods to determine sub-3 nm aerosol size distributions using the particle size magnifier," *Atmos. Meas. Tech.*, vol. 11, no. 7, pp. 4477–4491, Jul. 2018, doi: 10.5194/amt-11-4477-2018.

[132] K. Lehtipalo *et al.*, "Methods for determining particle size distribution and growth rates between 1 and 3 nm using the Particle Size Magnifier," vol. 19, p. 22.

[133] L. Dada *et al.*, "Formation and growth of sub-3-nm aerosol particles in experimental chambers," *Nat Protoc*, vol. 15, no. 3, pp. 1013–1040, Mar. 2020, doi: 10.1038/s41596-019-0274-z.

[134] C. Bloss *et al.*, "Development of a detailed chemical mechanism (MCMv3.1) for the atmospheric oxidation of aromatic hydrocarbons," *Atmos. Chem. Phys.*, p. 24, 2005.

[135] M. E. Jenkin, S. M. Saunders, V. Wagner, and M. J. Pilling, "Protocol for the development of the Master Chemical Mechanism, MCM v3 (Part B): tropospheric degradation of aromatic volatile organic compounds," *Part B*, p. 13, 2003.

[136] R. Marten *et al.*, "Survival of newly formed particles in haze conditions," *Environ. Sci.: Atmos.*, p. 10.1039.D2EA00007E, 2022, doi: 10.1039/D2EA00007E.

[137] M. Wang *et al.*, "Synergistic HNO3–H2SO4–NH3 upper tropospheric particle formation," *Nature*, vol. 605, no. 7910, pp. 483–489, May 2022, doi: 10.1038/s41586-022-04605-4.

[138] A. W. Stelson and J. H. Seinfeld, "THERMODYNAMIC PREDICTION OF THE WATER ACTIVITY, NH4NO3 DISSOCIATION CONSTANT, DENSITY AND REFRACTIVE INDEX FOR THE NH,,NO3-(NH,,)2SO,,-H20 SYSTEM AT 25°C," p. 8.

[139] L. Hao, E. Kari, A. Leskinen, D. R. Worsnop, and A. Virtanen, "Direct contribution of ammonia to α-pinene secondary organic aerosol formation," *Atmos. Chem. Phys.*, vol. 20, no. 22, pp. 14393–14405, Nov. 2020, doi: 10.5194/acp-20-14393-2020.

[140] K. Na, C. Song, C. Switzer, and D. R. Cocker, "Effect of Ammonia on Secondary Organic Aerosol Formation from α-Pinene Ozonolysis in Dry and Humid Conditions," *Environ. Sci. Technol.*, vol. 41, no. 17, pp. 6096–6102, Sep. 2007, doi: 10.1021/es061956y.

[141] T. Nah *et al.*, "Characterization of aerosol composition, aerosol acidity, and organic acid partitioning at an agriculturally intensive rural southeastern US site," *Atmos. Chem. Phys.*, vol. 18, no. 15, pp. 11471–11491, Aug. 2018, doi: 10.5194/acp-18-11471-2018.

Curriculum vitae

RUBY MARTEN

EDUCATION

2017 − 2022	**Doctorate:** Department of Environmental System Science (D-USYS) at ETH Zurich, and the Laboratory of Atmospheric Chemistry (LAC) at the Paul Scherrer Institut (PSI, Villigen) Doctor Father: Prof. Dr. Urs Baltensperger (ETH)
2011 − 2015	**Master in Science in Chemistry with Industrial Experience with First Class Honours:** School of Chemistry, University of Bristol, UK
	Master thesis: Center for Colloid and Interface Science. Thesis Supervisor: Prof. Dr. Julian Eastoe

WORK EXPERIENCE

2016 – 2017	**R&D Lab Technician:** Flint Group Sweden AB, Trelleborg, Sweden
2013 – 2014	**Intern research scientist:** Royal DSM N.V., Chemelot, Geleen, Netherlands

PUBLICATIONS

R. Marten, "Survival of newly formed particles in haze conditions," Environmental Science: Atmospheres, doi: 10.1039/D2EA00007E.

M. Wang et al., (2022). Synergistic HNO3–H2SO4–NH3 upper tropospheric particle formation. Nature. 605. 483-489. 10.1038/s41586-022-04605-4.

M. Wang et al., "Rapid growth of new atmospheric particles by nitric acid and ammonia condensation," Nature, vol. 581, no. 7807, pp. 184–189, May 2020, doi: 10.1038/s41586-020-2270-4.

M. Xiao et al., "The driving factors of new particle formation and growth in the polluted boundary layer," Atmos. Chem. Phys., vol. 21, no. 18, pp. 14275–14291, Sep. 2021, doi: 10.5194/acp-21-14275-2021.

L. Caudillo et al., "Chemical composition of nanoparticles from α-pinene nucleation and the influence of isoprene and relative humidity at low temperature," Atmos. Chem. Phys., vol. 21, no. 22, pp. 17099–17114, Nov. 2021, doi: 10.5194/acp-21-17099-2021.

X.-C. He et al., "Role of iodine oxoacids in atmospheric aerosol nucleation," Science, vol. 371, no. 6529, pp. 589–595, Feb. 2021, doi: 10.1126/science.abe0298.

X.-C. He et al., "Determination of the collision rate coefficient between charged iodic acid clusters and iodic acid using the appearance time method," Aerosol Science and Technology, vol. 55, no. 2, pp. 231–242, Feb. 2021, doi: 10.1080/02786826.2020.1839013.

D. Stolzenburg et al., "Enhanced growth rate of atmospheric particles from sulfuric acid," Atmos. Chem. Phys., vol. 20, no. 12, pp. 7359–7372, Jun. 2020, doi: 10.5194/acp-20-7359-2020.

M. Simon et al., "Molecular understanding of new-particle formation from α-pinene between −50 and +25 °C," Atmos. Chem. Phys., vol. 20, no. 15, pp. 9183–9207, Aug. 2020, doi: 10.5194/acp-20-9183-2020.

M. Heinritzi et al., "Molecular understanding of the suppression of new-particle formation by isoprene," Atmos. Chem. Phys., vol. 20, no. 20, pp. 11809–11821, Oct. 2020, doi: 10.5194/acp-20-11809-2020.

Q. Ye et al., "Molecular Composition and Volatility of Nucleated Particles from α-Pinene Oxidation between −50 °C and +25 °C," Environ. Sci. Technol., vol. 53, no. 21, pp. 12357–12365, Nov. 2019, doi: 10.1021/acs.est.9b03265.